Master's thesis

NTNU
Norwegian University of Science and Technology
Faculty of Engineering
Department of Energy and Process Engineering

Andreas Herløsund Søgnen

Numerical analysis of finned-tubes and finned-tube bundles

Master's thesis in Mechanical Engineering
Supervisor: Erling Næss
June 2021

NTNU
Norwegian University of
Science and Technology

Andreas Herløsund Søgnen

Numerical analysis of finned-tubes and finned-tube bundles

Master's thesis in Mechanical Engineering
Supervisor: Erling Næss
June 2021

Norwegian University of Science and Technology
Faculty of Engineering
Department of Energy and Process Engineering

NTNU
Kunnskap for en bedre verden

MASTER THESIS

for

Student Andreas Herløsund Søgnen

Spring 2021

Numerical analysis of finned-tubes and finned-tube bundles

Numerisk analyse av finnede rør og finnede rørbunter

Background and objective

The exhaust gas from a gas turbine engine contain large amounts of heat that can be utilized for process purposes or for power generation. The power production potential on a typical offshore oil and gas platform is in the order of 10MWe, which would reduce on-site CO2 emissions drastically if utilized. However, heat recovery units needs to be compact and lightweight in order to fit on the platform deck, while also maintaining reliability. This leads to an intricate compromise, as lightweight designs with less structural stiffness can be more prone to flow-induced vibrations. NTNU, in cooperation with SINTEF Energy Research and major industry players, is engaged in research work which seeks to develop new, compact heat exchanger solutions for gas turbine exhaust gases. In this context, finned tubes have been selected as good candidates due to the high specific heat transfer surface. Specifically, research has indicated that tubes with a smaller diameter than what is commonly used today may lead to significant weight savings. More data on the heat transfer and pressure drop performance, as well as flow induced forces, of small diameter fin tubes are needed to verify this hypothesis. CFD has been selected as a suitable design tool to study how tube geometry variations affect heat transfer performance and susceptibility to vibrations. Modeling existing geometries and comparing with experimental data is a vital step to build confidence in such models and justify modeling assumptions. Currently, transient CFD simulations of a small section of a heat exchanger unit is believed to be the most viable modeling approach, but steady state simulations can be used to study mesh.

Objective:

The main objective of this project work is to further validate a CFD model of one particular fin tube geometry developed in the project thesis, and to extend the model to a full bundle of finned-tubes. The extended model shall be validated against experimental data and used to quantify the influence of important parameters mainly on the heat transfer and the pressure drop behaviour of the bundle.

The following tasks are to be considered:

For a single row of finned-tubes:

1. Study the effect of a resolved versus an unresolved mesh at the boundary between the finned-tubes and the fluid with regards to heat transfer, pressure drop and vortex shedding.
2. Investigate the influence of turbulence models applicable for the problem. The findings shall be presented, discussed and compared with special focus on predicting heat transfer

For a full finned-tube bundle:

3. The model developed for a particular fin tube geometry in the project thesis shall be extended to a full bundle. The model shall be validated against available data in literature for the heat transfer coefficient and the pressure drop.
4. A numerical investigation of the influence of geometrical dimensions on the heat transfer coefficient, pressure drop and heat transfer distribution shall be conducted. The dimensions can be the fin and tube diameter, fin spacing and height, and the tube spacing and layout. The findings shall be compared with, and discussed in context of available literature
5. Suggestions for further work shall be presented.

Abstract

The objective of this thesis is to use CFD to investigate the air-side heat transfer and pressure drop over finned-tubes and finned-tube bundles, using the software OpenFOAM. The finned-tubes investigated have a small tube diameter to save weight. This is necessary due to their intended usage in offshore waste heat recovery units. In such applications, the weight and volume must be kept to a minimum. This requires optimisation of the design. For optimisation, understanding the local heat transfer behaviour is important. To this extent, CFD can be a powerful tool.

The work in this thesis is a continuation of the work done in the project thesis [65], where a simulation model for one row of solid annular finned-tubes was developed. An updated version of this model was used in this thesis to investigate the grid dependency of the simulation results and the influence of using different turbulence models. The findings showed that y_p^+ should be kept below two, which is in accordance with recommendations found in the literature. y_p^+ is here used to describe a dimensionless distance from a wall boundary to the first cell centre in the grid. From the investigation of suitable turbulence models, the Spalart-Allmaras turbulence model was chosen. It was chosen for its simplicity and stability, without any significant sacrifice in the accuracy of the results.

These findings were then used to develop a full bundle model, initially consisting of eight rows. Quite a lot of problems were experienced in the generation of the grids for the full bundle simulations. These problems in achieving a good grid meant the Reynolds number had to be limited to $Re = 5500$ for all the simulations. Three initial simulations were performed using the eight-row full bundle simulation domain. A mistake was, however, made in the geometry where every other row was slightly shifted. The results for the pressure drop and heat transfer coefficient were within the error band of the correlations used to validate the model. The row-by-row heat transfer coefficient did, however, not behave as expected from the literature. These row-by-row results were intended to be used as an aid in deciding how many rows to model in the rest of the thesis. Since the simulation geometries were incorrect, findings in the literature were used instead. From which it was decided to continue with five rows.

An investigation into geometry parameters was conducted at a Reynolds number $Re = 5500$. These all used a modified version of the full bundle model with five rows. To get a better comparison for these simulations, a new five-row simulation with the initial geometry was performed. Compared to the eight-row simulation, this five-row simulation had a 26% lower heat transfer coefficient. Why this is, was not found, but differences in mesh quality seem likely.

The geometry parameters investigated were fin tip clearance, fin pitch and tube bundle layout. The simulation results for the different parameters were compared with the literature. The local heat transfer coefficient over the fins was also compared. This was done to get a better understanding of how the changes in the geometry parameters affects the heat transfer. A literature study of the distribution of the heat transfer coefficient over the fin was conducted. However, how changes in the geometry changes the distribution of the heat transfer coefficient is lacking in the literature. This is something new this thesis provides.

Possible explanations for the behaviours seen in the results for the different geometry changes have been proposed. Further studies are, however, needed to confirm the behaviours found in the simulation results, and what is causing them.

The simulations in this thesis were run on a computer provided by the Department of Energy and Process Engineering (EPT), and on the computer cluster IDUN/EPIC at NTNU.

A reduced domain full bundle model with cyclic boundary conditions in the streamwise direction was also investigated. No successful implementation was, however, achieved.

Sammendrag

Målet for denne masteravhandlingen er å bruke numerisk fluiddynamikk (CFD) til å undersøke varmeovergang og trykktap for luftsiden av finnede rør og finnede rørbunter i programmet OpenFOAM. De finnede rørene som er undersøkt har en liten rørdiameter for å spare vekt. Detter er nødvendig fordi rørene skal brukes i offshore gjenvinning av spillvarme (WHRU). Til denne bruken er lav vekt og lavt volum viktig. Dette krever en optimalisering av designet, og for en slik optimalisering er forståelse for hvordan den lokale varmeoverføringen oppfører seg viktig. Her kan numerisk fluiddynamikk være et godt verktøy.

Arbeidet i denne avhandlingen er en fortsettelse på arbeidet gjort i prosjektavhandlingen [65]. I prosjektavhandlingen ble en numerisk modell for en rad av runde heltrukne finnede rør utviklet. En oppdatert versjon av denne modellen ble brukt i denne avhandlingen. Først til å undersøke mesh/grid avhengighet, så til å undersøke forskjeller mellom noen passende turbulensmodeller.

Disse undersøkelsen viste at y_p^+ bør ha en verdi lavere enn to, noe som samsvarer med anbefalinger funnet i litteraturen. y_p^+ er her en størrelse brukt til å beskrive en dimensjonsløs avstand fra en vegg til det første gridpunktet. Utfra resultatene for de forskjellige turbulensmodeller ble Spalart-Allmaras turbulensmodellen valgt. Denne modellen ble valgt fordi den er stabil og enkel, uten at det påvirker nøyaktigheten i resultatet signifikant.

Disse resultatene ble så brukt til å utvikle en full rørbunt modell, denne hadde i utgangspunktet åtte rørrekker. En del problemer oppstod i genereringen av et grid til full rørbunt simuleringene. Disse problemene med å genere et godt grid resulterte i at Reynolds-tallet måtte ha en øvre begrensning på $Re = 5500$ for alle simuleringene.

Tre simuleringer ble kjørt på dette åtterekkers simulerings domenet. En feil ble gjort da geometriene ble tegnet som gjorde at annenhver rekke var forskjøvet. Trykktap og varmeovergangsresultatene er fremdeles innenfor feilbandet til korrelasjonene som ble brukt for å validere modellen. Varmeovergangen rekke for rekke oppførte seg derimot annerledes enn hva som er forventet utfra resultater i litteraturen. Rekke for rekke resultatene fra simuleringene var tenkt som hjelp til å bestemme hvor mange rørrekker som skulle modelleres i resten av avhandlingen. Siden det vare en feil i geometrien, ble det i stedet tatt en bestemmelse ved hjelp av resultater i litteraturen. Fra disse ble det bestemt å fortsette med fem rørrekker.

En undersøkelse av geometriparametere ble gjennomført med et Reynolds-tall på $Re = 5500$. Disse undersøkelsen ble alle gjort med en modifisert versjon av den fulle rørbunt modellen med fem rørrekker. For å ha et bedre grunnlag for å sammenligne ble en ny fem rekkers simulering med den originale geometrien gjennomfør. Sammenlignet med åtterørs simuleringen hadde denne fem rørs simuleringen et varmeovergangstall som var 26% lavere. Hvorfor dette vare tilfelle er ikke oppklart, men forskjeller i mesh-kvalitet virker sannsynlig. Geometri parameterne som ble undersøkt var finnetuppklaring, finne avstand/pitch og rørbunt konfigurasjon. De numeriske resultatene for de forskjellige parameterne ble sammenlignet med eksisterende litteratur. Fordelingen av varmeovergangstallet over finnene ble også sammenlignet. Dette ble gjort for å bedre forstå hvordan varmeovergangen blir påvirket av geometriforandringene.

Et litteraturstudium om fordelingen av varmeovergangstallet over en finne ble også gjennomført. Resultater for hvordan varmeovergangstallsfordelingen blir påvirket av geometriforandringer er ikke funnet i litteraturen, og er dermed noe nytt denne avhandlingen tilbyr.

Mulige forklaringer på de forskjellige oppførselene sett i resultatene for geometriforandringene er foreslått. Videre arbeid trengs derimot til å bekrefte om oppførselene er rette og hva som faktisk ligger til grunne for dem.

Simuleringene i denne avhandlingen er kjørt på en stasjonær PC utlånt av instituttet for Energi og Prosessteknikk (EPT), og på IDUN/EPIC regne-clusteret på NTNU.

En redusert domene modell for en full rørbunt med sykliske grensebetingelser i strømningsretningen ble også undersøkt. Implementeringen av denne var ikke suksessfull.

Preface

This is a master thesis which was carried out at the Department of Energy and Process Engineering (EPT) at the Norwegian University of Science and Technology (NTNU) in the spring of 2021.

I want to thank my supervisor professor Erling Næss for the continuous support, guidance and help in understanding the results in this thesis.

Andreas Herløsund Søgnen
Trondheim, June 2021

Contents

Nomenclature

Symbols

ΔP	Pressure drop	[Pa]
ΔP_a	Pressure drop due to acceleration	[Pa]
ΔT_{LM}	Logarithmic mean temperature difference	[K]
$\dot{m}$	Mass flow rate	[kg/s]
$\dot{Q}$	Heat duty	[W]
$\dot{V}$	Volumetric flow rate	[m$^3/s$]
$\widetilde{h}$	Enthalpy	[J/kg]
$\widetilde{u}_i$	Velocity in the i-direction	[m/s]
A_b	Tube heat transfer area between the fins	[m^2]
A_f	Fin heat transfer area	[m^2]
A_{in}	Area at the inlet of the domain	[m^2]
A_{min}	Minimum free-flow area	[m^2]
A_{P_d}	Area in diagonal plane	[m^2]
A_{P_t}	Area in transverse plane	[m^2]
$A_{tot} = A_f + A_b$	Total heat transfer area	[m^2]
Ar	Overall extended-surface-area ratio	[-]
C_f	Fin tip clearance	[m]
C_p	Specific heat at constant pressure	[J/(Kg·K)]
C_μ	Constant used in various turbulence models	[-]
d_f	Fin diameter	[m]
d_o	Outside diameter of the tube	[m]
d_{eff}	Effective diameter	[m]
f_{vs}	Vortex shedding frequency	[1/s]
G	Mass velocity in the smallest free-flow area	[Kg/(m$^2 \cdot s$)]

h	Size of cube sides in the background mesh	[m]
h_f	Fin height	[m]
h_o	Outside tube heat transfer coefficient	$[\mathrm{W}/(\mathrm{m}^2 \cdot K)]$
h_{app}	Apparent or overall outside heat transfer coefficient	$[\mathrm{W}/(\mathrm{m}^2 K)]$
h_{loc}	Local heat transfer coefficient	$[\mathrm{W}/(\mathrm{m}^2 \cdot K)]$
I	Turbulent intensity	[-]
K	Specific kinetic energy	[J/kg]
k	Turbulent kinetic energy	[J/Kg]
l	Length scale in turbulence modelling	[m]
NTU	Number of heat transfer units	[-]
P	Pressure	[Pa]
P_d	Diagonal pitch	[m]
P_l	Longitudinal pitch	[m]
P_t	Transverse pitch	[m]
q''	Heat flux	$[\mathrm{W}/\mathrm{m}^2]$
$R_{i,j}$	Reynolds stresses	[J/Kg]
S	Fin pitch	[m]
t	Fin thickness	[m]
T_f	Local fin temperature	[K]
T_{in}	Inlet temperature	[K]
T_m	Arithmetic mean temperature	[K]
T_{out}	Outlet temperature	[K]
T_{ref}	Reference temperature	[K]
T_w	Tube wall temperature	[K]
U_i	Mean velocity in the i-direction	[m/s]
u_i	Velocity fluctuation in the i-direction	[m/s]
u_τ	Shear velocity	[m/s]
U_{Amin}	Average velocity in minimum free flow area	[m/s]
U_{in}	Inlet velocity	[m/s]
y^*	Dimensionless wall distance based on turbulent kinetic energy	[-]
y^+	Dimensionless wall distance based on shear-velocity	[-]
y_p^+	Dimensionless wall distance to the first cell-centre in the mesh	[-]

y_p	Distance to first cell-centre in the mesh	[m]
E	Total energy	[J/Kg]
e	Internal energy	[J/Kg]
L	Reduced domain length	[m]
m	Fin efficiency parameter	[1/m]
N	Number of tube rows	[-]

Dimensionless Groups

C_l	Lift coefficient
$Eu = \frac{2 \cdot \Delta P}{\rho U^2_{(Amin)} N}$	The Euler number
$Nu = \frac{h_o \cdot c_o}{\kappa}$	Nusselt number
Pr_t	Turbulent Prandtl number
Re_{dh}	Reynolds number based on the hydraulic diameter d_h
$Re_{do} = \frac{\dot{m} \cdot d_o}{A_{min} \cdot \mu}$	Reynolds number in the minimum free-flow area
Sr	Strouhal number
j	Colburn j-factor
Pr	Prandtl number
Sc	Schmidt number
Sh	Sherwood number

Greek Letters

α	Thermal diffusivity	[m$^2/s$]
α_t	Turbulent diffusivity	[m$^2/s$]
β	Tube layout angle	[-]
β_L	Pressure gradient over the reduced domain with length L	[Pa/m]
$\delta_{i,j}$	Kronecker delta	[-]
ϵ	Turbulent dissipation rate	[J/(Kg$\cdot s$)]
ϵ_{τ}	Effectiveness parameter in the $\epsilon - NTU$ method	[-]
η_f	Fin efficiency	[-]
γ	Original temperature gradient over the reduced domain	[K/m]
γ_1	Corrected temperature gradient over the reduced domain	[K/m]
κ	Thermal conductivity of air	[W/(m$\cdot K$)]
μ	Dynamic viscosity	[Pa $\cdot s$]

ω	Specific turbulent dissipation rate	[1/s]
ϕ	Modified fin height	[m]
ρ	Density	[Kg/m^3]
σ	Minimum-to-inlet area ratio	[-]
θ	Angle from the inflow	[-]
$\widetilde{\nu}$	Transport variable in Spalart -Allmaras turbulence model	$[m^2/s]$

Subscripts

b	Bare tube between fins
corr	Correlation
f	Fin
in	Inlet of simulation domain
num	Numerical
out	Outlet of simulation domain
ref	Reference
t	Turbulence
tot	Total heat transfer area

Abbreviations

AMI Arbitrary Mesh Interface

BL Boundary Layer

CFD Computational Fluid Dynamics
CHT Conjugate heat transfer

DNS Direct numerical simulation

LRR Launder, Reece and Rodi

RANS Reynolds averaged Navier-Stokes
RSM Reynolds stress model

SA Spalart-Allmaras turbulence model
SST Shear Stress Transport

WHRU Waste Heat Recovery Unit

List of Figures

List of Tables

1 Introduction

The electricity produced offshore is often produced by gas turbines. In the production cycle, the excess heat in the exhaust is usually just emitted to the atmosphere or partially recovered for heating purposes. Waste Heat Recovery Units (WHRUs) can be implemented into the cycle to utilise more of this excess heat. The recovered heat can then be used for power production. Implementing a WHRU into the power production cycle increases overall efficiency, cuts energy use and thus lowers emissions. With high fuel prices and high taxes on CO_2 emissions, this can also be cost-effective.

On offshore platforms space is limited and weight must be kept down. It is therefore important that the WHRU is light and compact. To achieve this, the WHRU must have an optimal design in terms of weight and volume [64]. Finned-tube heat exchangers have been chosen as a good candidate for usage in WHRUs due to their high heat transfer per unit volume. To save weight, using a smaller tube diameter than what is normally used has been proposed. These finned-tubes with a smaller tube diameter have been less studied. Further investigations are, therefore, needed to better understand how these behave and see if the smaller tube diameter works as intended. These investigations can then be used to improve the heat transfer and pressure drop correlations and obtain good design guidelines.

The air (or gas) side performance is the limiting factor in a finned-tube heat exchanger, and the fins are added to the tubes to enhance the air-side heat transfer [21]. Understanding the air-side of the heat exchanger is therefore crucial. For this, an accurate numerical model can give a lot of insight which is difficult to obtain experimentally. Computational Fluid Dynamics (CFD) can to this extent be a great tool to supplement experimental testing. The CFD model can be used both to qualitatively understand the local flow behaviour and to quantitatively investigate how changes in the geometry influences the heat transfer and pressure drop [34]. The limitation of CFD is the need for experimental data to validate the model. This experimental data also comes with an uncertainty due to uncertainties in the measurements. The computational cost of CFD is also a drawback, and it is important to find a balance between model accuracy and computational cost.

The main objective in this thesis is to use the open-source CFD software OpenFOAM to investigate the air-side heat transfer and pressure drop over finned-tubes and finned-tube bundles. The secondary objective is to quantify how the heat transfer and pressure drop depends on some particular geometry parameters of the finned-tubes and finned-tube bundle. This thesis is a continuation of the project work [65], where a one-row model for a particular finned-tube geometry was developed. This finned-tube geometry has solid annular fins and is used as a starting point for the geometries investigated in this thesis. The project work and the work in this thesis builds on numerical work in a Ph.D. by Lindqvist [33] and experimental work in a Ph.D. by Holfeld [17]. Both investigated, among others, the finned-tube geometry modelled in this thesis.

To challenge some results found in the project thesis, investigations of both the dependency of y_p^+ values in the results and of suitable turbulence models for the problem were performed. y_p^+ is defined as the dimensionless distance from a wall boundary to the first cell centre in the mesh. These two investigations were performed with an updated version of the one-row model developed in the project work. The one-row model was then extended to a full bundle model, and this full bundle model was used to investigate changes in some geometry parameters of the finned-tubes and finned-tube bundles. The results are compared to available literature.

There are some assumptions that are used throughout this thesis. The first one is for the simulation domains. It is assumed that a cut-out in the flow direction is representative of a whole tube bundle. In the one-row simulation domain, only one fin and half of the tube lengths between the two adjacent fins are modelled. Cyclic boundary conditions are then used in the tube-axis direction and column direction to represent a row of finned-tubes. The one-row simulation domain is shown in Figure (19) in section 3.1. In the full bundle model, a given number of finned-tubes are modelled this way to represent a finned-tube bundle. Each modelled finned-tube representing a row. The full bundle simulation domain is shown in Figure (28) in section 3.4.

This use of cyclic boundary conditions implies that the finned-tubes modelled are deep inside a tube bundle since any end-effects of the heat exchanger casing are neglected.

The effect of radiation inside the heat exchanger is also neglected. The same for the difference between helically wound and annular solid finned-tubes. These are assumed to behave identically.

Some of the findings from the project thesis are also used. In the project thesis [65], heat conduction through the tube wall was included in the simulations. This was found to increase the simulation time without any significant difference in the results compared to having a constant temperature at the outside tube wall. This is therefore neglected in this thesis, and a constant temperature is used at the outside tube walls. This simplification was also used by Lindqvist [33].

The material used in the finned-tubes is aluminium which has a high conductivity. An investigation into fin efficiency corrections was performed in the project thesis. It was found that because of this high conductivity the corrections made no significant difference to the results. For this reason, a theoretical fin efficiency is used in this thesis.

A computer was provided by the Department of Energy and Process Engineering (EPT) for use in the master's thesis. This was mainly used for grid generation and setting up the different simulations, although some of the one-row simulations were run on this computer. The rest of the simulations were run on the computer cluster IDUN/EPIC at NTNU. The computer cluster is described in this technical report by Själander et al. [63].

1.1 Structure of the thesis

The thesis is structured as follows:

Chapter 2 is a review of the literature used in chapters 3 and 4. Including a description and comparison of the tested turbulence models, and results from the literature used as a comparison for the simulation results.

Chapter 3 is a method part. Here the updated one-row model is presented. Preliminary results for the y_p^+ and mesh investigation, and for the simulations with different turbulence models are also presented. These results are then used to extend the one-row model into a full bundle model.

Chapter 4 contains the results and discussion of the results for the full bundle simulations. First, the results of three initial simulations are presented. These are compared with the literature to validate the model. The results for the row-by-row heat transfer coefficient for these simulations are also presented and compared with the literature. Then the results for changes to three different geometry parameters are presented and compared with the literature.

Conclusions of the work done in this thesis are given in chapter 5, and chapter 6 contains suggestions for further work.

2 Review of previous work

This section is a review of the literature used in sections 3 and 4.

2.1 Turbulence models

Turbulence is a relatively hard phenomenon to model. The motion appears random, and the easiest way to describe it is often by means of statistics. Turbulence is, however, deterministic, and the Navier-Stokes equations can be used to describe it fully. In CFD simulations, solving it this way is called direct numerical simulations (DNS). This is very computationally heavy and requires a grid fine enough to capture the smallest turbulent structures. For practical applications, this is usually not viable, and one instead solves the Reynolds averaged version of the Navier-Stokes equations (RANS) [68, 70]. The RANS equations are shown in equation (24) in section 3.1. The outcome of averaging the Navier-Stokes equations into the RANS equations is the addition of a new term, $-\overline{u_i u_j}$. This term is usually called the Reynolds stresses, and to have closure of the RANS equations, this term needs to be modelled. A similar term also appears in the Reynolds averaged energy equation (see equation (25)). However, this term is usually modelled implicitly through a constant turbulent Prandtl number (Pr_t) relating it to the Reynolds stresses [2].

It should be noted that lowercase letters (e.g. u_i) are used for fluctuating quantities, and uppercase letters (e.g. U_i) are used for the mean.

The Reynolds stresses are in most turbulence models modelled using the turbulent viscosity approach. In this section, the turbulent viscosity approach is defined, and four turbulence models using this approach are presented. The four turbulence models chosen should all be suitable for the problem at hand. To challenge the turbulent viscosity approach, a Reynolds stress model, which solves the Reynolds stresses more directly, is also included. The models are then compared to each other and to how they are expected to perform for the problem at hand, then in section 3.3, the models are tested out.

Turbulent viscosity

Momentum is generally transported in the same direction as the velocity gradient. From this, an assumption is made that the Reynolds stress is proportional to the velocity gradient: $-\overline{uv} = \nu_t \cdot \frac{\partial U}{\partial y}$. With ν_t being the constant of proportionality called the eddy or turbulent viscosity, analogous to the molecular viscosity (ν) due to the assumed form it takes in the equation. Unlike ν, ν_t is purely artificial and needs to be modelled [2, 70].

This assumption and way of modelling was introduced by Boussinesq and is often called the eddy viscosity hypothesis [2]. Extended to 3D, it takes the form:

$$-\overline{u_i v_j} = \nu_t \left(\frac{\partial U_i}{\partial x_j} + \frac{\partial U_j}{\partial x_i} - \delta_{i,j} \frac{1}{3} \frac{\partial U_k}{\partial x_k} \right) - \delta_{i,j} \frac{2}{3} k \tag{1}$$

where $\delta_{i,j}$ is the Kronecker delta and k is the mean turbulent kinetic energy. The added terms are a correction to avoid zero Reynolds stresses along the normal (where i=j) by continuity.

For an incompressible flow using the rate of strain tensor $S_{ij} = \frac{1}{2}\left(\frac{\partial U_i}{\partial x_j} + \frac{\partial U_j}{\partial x_i}\right)$ equation (1) simplifies to:

$$-\overline{u_i v_j} = 2\nu_t S_{ij} - \delta_{i,j} \frac{2}{3} k \tag{2}$$

The different eddy viscosity turbulence models are then used to model ν_t. The definition of ν_t means that turbulence is assumed to be isotropic. This is not always the case and is one of the obvious limitations of this modelling approach [2, 70].

The simplest turbulence models are algebraic models. These either assume ν_t to be constant or a function of local flow parameters depending usually on a velocity and length scale. These models are very simplistic and cannot predict more complex flow structures like separation and backflow. In more advanced turbulence models, extra transport equations are solved. These are classified after how many extra transport equations they use [2].

Several eddy viscosity turbulence models are based upon solving a transport equation for the turbulent kinetic energy ($k = 1/2 \cdot \overline{u_i u_i}$). A transport equation for k can be derived from the Navier-Stokes equations. On a quasi-symbolic form this becomes:

$$\frac{Dk}{Dt} = D_k + P_k - \epsilon \tag{3}$$

where D_k is the diffusion of k which are a function of both the molecular and turbulent viscosity. P_k is the production of k and ϵ is the dissipation of k. Although an exact equation can be obtained, the terms must be modelled in order to solve it numerically [2].

From solving equation (3), ν_t can be calculated using the Prandtl-Kolmogorov relation: $\nu_t = C_\mu \cdot \sqrt{k} \cdot l$, where C_μ is a constant, and l is an unknown turbulent length scale. This length scale is usually modelled indirectly through another transport equation [2]. It should be mentioned that there are exceptions to this way of modelling, especially for one-equation models which usually solves for ν_t more directly [61].

The first modern turbulence model to use this way of modelling was the standard $k - \epsilon$ model. In this model transport equations for k and ϵ are solved, where ϵ is the turbulent dissipation rate found in equation (3). ϵ represents dissipation of k into heat, and is related to the turbulent length scale, viz: $\epsilon = C_\mu^{0.75} \cdot k^{1.5}/l$. Inserting this into the Prantl-Kolmogorov relation, ν_t can be found [2].

Being one of the first modern turbulence models, taking over for the algebraic models, the $k - \epsilon$ model has endured extensive testing and is the most validated turbulence model. This testing has revealed the model to be most accurate at higher Reynolds numbers, with the first grid point situated in the log-layer of the law of the wall (see section (3.2)) and without separation of the flow [70].

Revisions to the original $k - \epsilon$ turbulence model by Launder and Spalding (1974) incorporating wall damping functions have been proposed. The wall damping takes into account the molecular viscosity which is present in the viscous sublayer in the law of the wall. These revisions, usually called low Reynolds $k - \epsilon$ models, are more accurate if the first grid point is situated in the viscous sublayer [70]. The damping functions do, however, rely on relatively crude modelling making them inaccurate [45].

The modern version of the $k - \omega$ turbulence model was developed to better predict the wall behaviour compared to the $k - \epsilon$ model. In the $k - \omega$ turbulence model a transport equation for ω is solved instead of a transport equation for ϵ. Physically ω represents the specific turbulent dissipation rate, meaning it is very closely related to and represents the same phenomena as ϵ [28]. The relation between the two is given in equation (4).

$$\omega = \frac{\epsilon}{C_\mu k} \tag{4}$$

The transport equation for ω differs slightly from the transport equation for ϵ solved in the $k - \epsilon$ turbulence model. As a consequence, the damping functions added in order for the $k - \epsilon$ turbulence model to be used near walls, are not needed. This gives the $k - \omega$ turbulence model superior accuracy near walls where the molecular viscosity is dominant over ν_t. The $k - \omega$ model also gives better results if the flow has an adverse pressure gradient. Testing has, however, shown the model to be dependent on the applied freestream conditions [45, 70].

Spalart-Allmaras

The Spalart-Allmaras turbulence model was the model used in the project thesis, and most of the description below is similar to the one found in the project thesis [65].

The Spalart-Allmaras (SA) turbulence model was originally developed for aerodynamics, with the aim being to develop a model which could handle the wake region and adverse pressure gradient behind an aerofoil better than the $k - \epsilon$ turbulence model [66, 78]. In recent years, it has also found some usage in CFD simulations of turbomachinery [70].

The SA model is a one-equation turbulence model, but do not solve a transport equation for k. Instead, a transport equation is solved for the variable $\widetilde{\nu}$ which is made to fit ν_t in the log-layer in the law of the wall (see section (3.2)) [23, 78]. The behaviour of both ν_t and $\widetilde{\nu}$ is shown in Figure (1). In the Figure, ν_t and $\widetilde{\nu}$ are made dimensionless using the molecular viscosity: $\nu_t^+ = \nu_t/\nu$ and $\widetilde{\nu}^+ = \widetilde{\nu}/\nu$.

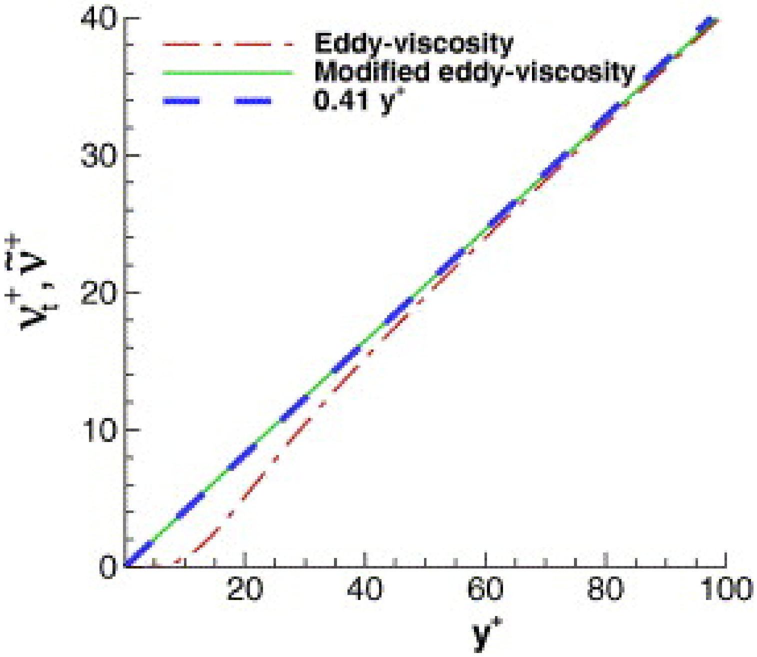

Figure 1: The transport variable in the Spalart-Allmaras turbulence model $\widetilde{\nu}$ (in figure made dimensionless as $\widetilde{\nu}^+ = \widetilde{\nu}/\nu$) and ν_t (in figure made dimensionless as $\nu_t^+ = \nu_t/\nu$) as a function of y^+ plotted along with a linear function of y^+ approximating $\widetilde{\nu}^+$ (Figure taken from Kalitzin et al. [23])

As can be seen from Figure (1), ν_t has a close to linear behaviour for $y^+ \gtrsim 30$, with the transport variable $\widetilde{\nu}$ continuing this line all the way to the wall.

The behaviour of ν_t seen in Figure (1) stems from the law of the wall (see section (3.2)). This means that for a flat plate, $\widetilde{\nu}$ should be a straight line (as seen in blue in Figure (1)). For other geometries, however, this is not necessarily the case, and $\widetilde{\nu}$ is found by solving a transport equation. On quasi-symbolic form this transport equation takes the form:

$$\frac{D\widetilde{\nu}}{Dt} = Prod + Diff + Distr \tag{5}$$

Where *Prod*, *Diff* and *Distr* is the production, diffusion and destruction of $\widetilde{\nu}$, respectively [66].

Even though $\widetilde{\nu}$ is not necessarily a straight line for more general geometries, one expects it to be close, since flow very close to a wall is largely independent of geometry [68]. This means the transport equation for $\widetilde{\nu}$ should be relatively cheap to solve [78].

The behaviour of ν_t and $\widetilde{\nu}$ differs significantly closer to the wall than the log-layer ($y^+ \lesssim 30$), as can be seen in Figure (1). To replicate the behaviour in the ν_t calculated from $\widetilde{\nu}$, a function f_{v1} is used ($\nu_t = f_{v1} \cdot \widetilde{\nu}$). The function f_{v1} takes the form:

$$f_{v1} = \frac{\chi^3}{\chi^3 + C_{v1}^3} \tag{6}$$

where $\chi = \widetilde{\nu}/\nu$ and C_{v1} is a constant [55, 66].

$k-\omega\ SST$

The $k-\omega SST$ (Shear Stress Transport) turbulence model was developed to be an improvement over the standard $k-\epsilon$ and $k-\omega$ models for use in aerodynamics. The $k-\epsilon$ model is known to have an unreliable performance near walls, and the $k-\omega$ model for being sensitive to small changes in the freestream values, with both models being known to predict flow separation poorly [70, 77].

The idea behind the $k-\omega SST$ model is to utilise the two basic models in the area where they are generally good. This means using the $k-\omega$ model near the walls and using the $k-\epsilon$ model far away from the walls [77].

The same transport equation for k as the two basic models (see equation (3)) is solved in the $k-\omega SST$ model, but with a different equation for ω than in the $k-\omega$ model. The ω equation in the $k-\omega SST$ model takes the quasi-symbolic form:

$$\frac{D\omega}{Dt} = Diff + P_\omega - D_\omega + (1-F_1)\cdot Add \tag{7}$$

with $Diff$ being the diffusion, P_ω the production and D_ω the dissipation of ω. This equation is the ϵ equation in the $k-\epsilon$ model rewritten to ω using the relation in equation (4).

The additional term, Add, comes from the rewriting of the ϵ equation and is not present in the ω equation solved in the $k-\omega$ model. F_1 is a blending function [70, 77].

A viscosity limiter is also added in the calculation of ν_t from k and ω. This ensures a better prediction of flow separation, by reducing ν_t in regions of high shear stress [70].

The blending function, F_1, is used to determine whether the transport equation for ω in equation (7) is equal to the ω equation from the $k-\omega$ model, the ϵ equation from the $k-\epsilon$ model or a blend between them. This is done by assigning a value of F_1 between zero and one to each cell in the mesh. A value $F_1 = 0$ is assigned to cells in the freestream, meaning the $k-\epsilon$ model is solved, and a value $F_1 = 1$ is assigned to cells adjacent to the wall boundaries, meaning the $k-\omega$ model is solved. To get a smooth transition between the models F_1 usually takes the form of a hyperbolic tangent function [70, 77].

Transition SST or $\gamma - Re_\theta$

The boundary layers in a flow are not always fully laminar or fully turbulent. The turbulence models described above are for fully turbulent boundary layers. However, there exist models which adjust the turbulence model to the local state, whether this is laminar, in a transition or fully turbulent. One such model is the Transition SST turbulence model which is a four-equation model. The model is based on the $k-\omega SST$ turbulence model, and is generally used for the same applications, but should be more accurate at low to moderate Reynolds numbers [42, 30].

Two of the equations solved in the Transition SST model are the same as in the $k-\omega SST$ model, but with some changes to the terms. In the k equation (see equation (3)), P_k and D_k are slightly altered, and in the ω equation (see equation (7)), F_1 is somewhat changed [46, 79].

The alteration of the blending function, F_1, does not change the functionality but rather ensures that it still works as intended in cells with laminar flow [79]. The change was implemented due to the authors of the model [46] finding the normal $k-\omega SST$ tending to zero and not one in the middle of a laminar region. This means the $k-\epsilon$ model is inadvertently used in a region where it is known to underperform compared with the $k-\omega$ model [30, 46].

The third transport equation solved is for the intermittency, γ. This is a quantity that takes a value $0 \leq \gamma \leq 1$ and the flow in the cells. A value γ=0 describes a fully laminar flow and a value γ=1 a fully turbulent flow in the given cell [79]. The altered production term in the k-equation is the original production term (seen in equation (3)) multiplied with the intermittency (i.e. $P_k \cdot \gamma$). The altered dissipation term has a similar behaviour. In turbulent flow ($\gamma = 1$) the dissipation remains the same as in the $k-\omega SST$ model (i.e. D_k), while for laminar flow ($\gamma = 0$) the dissipation term goes down to 10% of the fully turbulent dissipation (i.e. $0.1 \cdot D_k$), and not to zero [30, 29, 46]. This ensures that the turbulent kinetic energy is transported and dampened even in a laminar boundary layer where the production of turbulent kinetic energy is zero. In the transition region ($0 < \gamma < 1$), a behaviour in between is solved for [79]

The transport equation for γ takes the quasi-symbolic form:

$$\frac{D\gamma}{Dt} = Diff + P_\gamma - D_\gamma \tag{8}$$

where the production term P_γ controls for where the transition region starts, and the dissipation term D_γ allows the flow to re-laminarise. When the transition region starts, the intermittency takes a value different from zero. To find this onset of transition (and if present re-laminarisation), the momentum thickness Reynolds number, Re_θ is used. This gives a Reynolds number with a length scale, θ, which do not depend on user input and can be defined for any geometry [46, 79]. The authors of the model [46] found that transition started at a value ($Re_\theta = Re_{\theta,t}$) only dependent on freestream parameters. To determine all the local values of $Re_{\theta,t}$ (named $\overline{Re}_{\theta,t}$ by the authors of the model [46] to distinguish it from the value $Re_{\theta,t}$) a forth transport equation is solved. This takes the quasi-symbolic form:

$$\frac{D\overline{Re}_{\theta,t}}{Dt} = Diff + Prod \tag{9}$$

where $Diff$ and $Prod$ is the production and diffusion of $\overline{Re}_{\theta,t}$. This transport equation takes a constant value in the whole domain except the boundary layer, where $\overline{Re}_{\theta,t}$ diffuses towards the walls, where a zero gradient boundary condition is applied [79, 29, 46].

It is recommended to have $y_p^+ < 1$ when using this turbulence model, making it, alongside solving four transport equations, quite computationally heavy [29, 46].

Reliazible $k - \epsilon$ model

The realizable $k - \epsilon$ turbulence model is a newer and revised version of the standard $k - \epsilon$ model. The normal $k - \epsilon$ model is not very accurate for high shear flow and flows which have separation. Part of the reason for this is the relatively crude modelling of ϵ. Instead of starting from the exact equation for ϵ, which can be derived from the Navier-Stokes equations, a simplified ϵ equation similar to that of k is used in the $k - \epsilon$ model [62, 68].

In the realizable $k - \epsilon$ model, the transport equation for ϵ is modelled closer to the exact equation for ϵ. The model equation used stems from a model equation for the mean vorticity fluctuations, $\overline{\omega_i \omega_i}$, which also can be derived from the Navier-Stokes equations. At high Reynolds numbers, $\overline{\omega_i \omega_i}$ can be directly related to the turbulent dissipation rate: $\epsilon = \nu \cdot \overline{\omega_i \omega_i}$. The terms in this equation can then be modelled more easily than the terms in the exact ϵ equation [62, 68].

The turbulent viscosity ν_t is also redefined to be realizable (hence the name). This sets some requirements for the Reynolds stresses (and thus ν_t), which should prevent them from being non-physical. Here it is required that the Reynolds stresses are non-negative and that the Schwartz's inequality is satisfied. This is done through C_μ being a function dependent on k, ϵ, the strain rate and the vorticity, and not a constant. This makes the model more accurate for flows with high shear and separation [62].

LRR: A Reynolds stress turbulence model

The turbulent viscosity approach described at the start of this section constitute a major simplification in assuming $\overline{u_i u_j}$ to be isotropic through using the Boussinesq hypothesis. In real flows, this is not usually the case. Turbulence is usually produced in one direction before a redistribution to the other directions happens. In the turbulent viscosity models, both the possibility of anisotropic turbulence and the redistribution of turbulence is neglected [2].

In Reynolds stress models (RSM), the Boussinesq hypothesis is not used. Instead, $\overline{u_i u_j}$, which is the term missing to have closure of the RANS equations (see equation (24)), is solved for directly. Introducing the Reynolds stress tensor $R_{i,j} = \overline{u_i u_j}$, a transport equation for each of the terms can be derived exactly from the Navier-Stokes equations. Using that $R_{i,j}$ is symmetric (i.e. $R_{i,j} = R_{j,i}$) this becomes six different transport equations [2, 70].

These takes the quasi-symbolic form:

$$\frac{DR_{i,j}}{Dt} = P_{i,j} + \Phi_{i,j} + D_{i,j} - \epsilon_{i,j} \tag{10}$$

where $P_{i,j}$ is the production, $D_{i,j}$ is the diffusion and $\epsilon_{i,j}$ is the dissipation of $R_{i,j}$, while $\Phi_{i,j}$ is a new term called the "pressure strain correlation" [2]. This is the term responsible for the redistribution between the directions and is only active off the diagonals (i.e. when $i \neq j$).

In order to solve these equations the terms for Φ_{ij}, D_{ij} and ϵ_{ij} must be modelled, while $P_{i,j}$ is exact. The modelling of $\epsilon_{i,j}$ is usually done through solving a seventh transport equation. It is wort mentioning that for $i = j$, $R_{i,j}$ reduces to $2 \cdot k$. This reduced equation does not capture the redistribution since $\Phi_{i,i} = 0$. [2, 70]

The modern modelling of the terms in the Reynolds stress tensor ($R_{i,j}$) for use in CFD stems from Launder et al. [31], which became the LRR (Launder, Reece and Rodi) turbulence model [31, 70]. In the development of this model, a lot of effort was put into finding reliable models for the pressure-strain, $\Phi_{i,j}$, believing this to be the key to developing an accurate RSM model. However, in testing different models for $\Phi_{i,j}$, Launder et al. [31] did not find much difference. Instead, Launder et al. [31] found that the deviation between the model and some of their experimental results, more likely came from the modelling of $\epsilon_{i,j}$ or from the tuning of the model coefficients [31]. Supporting this is the fact that the modelling of $\epsilon_{i,j}$ in the LRR model is similar to the modelling of ϵ in the $k - \epsilon$ model. This has in turn shown the LRR turbulence model to produce similar inaccurate results as the $k - \epsilon$ model in some situations. One such situation worth mentioning is the modelling of a recirculating flow entering an open area [70].

All RSM models describe $R_{i,j}$ directly to give closure of the RANS equations (see equation (24)) instead of relying on the turbulent viscosity hypothesis. This means they all solve, usually, seven transport equations. This makes them computationally heavy compared to the usual two-equation (or one for the SA) turbulent viscosity models [70].

Comparison of the models above

The four turbulent viscosity models above have all been developed to handle an adverse pressure gradient and flow separation. These are, as mentioned, flow conditions also present in flow over finned-tubes. In their description of turbulence models, Versteeg et al. [70] described the $k - \omega SST$ model as the most accurate turbulent viscosity model for general flows, with the SA model only being good for aerodynamics. Their description does, however, not include the Realizable $k - \epsilon$ model.

Studies comparing turbulence models for simulations of finned-tube bundles seem to be quite scarce in the literature. An indication of suitable models can, however, be drawn from what has previously been used, although it does not show the performance of the models compared to each other. In a comparison of some previous works made by Lindqvist [33], the Realizable $k - \epsilon$ and the RNG $k - \epsilon$ were the recurring models. The RNG $k - \epsilon$ model is another improved $k - \epsilon$ model similar to the Realizable $k - \epsilon$ model described above. Both of these models were developed to be accurate in situations with high shear and/or flow separation, and both show improvements over the standard $k - \epsilon$ model [70, 62].

Lindqvist [33] found good agreement with the literature using the Spalart-Allmaras turbulence model. This inspired the use of the SA model in the project thesis [65] producing less accurate results. Lindqvist [33] did some simulations comparing the SA and the $k - \omega SST$ model. In these simulations, the results using the SA model were in better agreement with the experimental data and the experimental correlations Lindqvist [33] used for comparison than the $k - \omega\ SST$ turbulence model.

One of the studies which do compare turbulence models for flow over a finned-tube bundle is conducted by Nemati et al. [53]. They compared, among others, all of the eddy viscosity models described above. The simulations by Nemati et al. [53] were all performed using a five-row solid annular finned-tube bundle at a Reynolds number $Re_{do} \approx 4000$.

Their results show the pressure drop and heat transfer (in terms of Eu and Nu) between the SA, the Realizable $k-\epsilon$, the $k-\omega SST$ and the Transition SST model to differ by approximately 12.5% and 4% for Eu and Nu respectively. All of the models were also compared to an experimental correlation for Eu and an experimental correlation for Nu. The SA model was the turbulence model with the largest deviation from these correlations of the models mentioned above.

The resulting streamlines for the models were also compared in the study by Nemati et al. [53]. The separation from the finned-tubes and the recirculation zones behind the finned-tubes were almost identical between the models for all but the last row. For the last row, the recirculation zones behind the finned-tubes varied some more. According to Nemati et al. [53], the flow separation from the tubes was at $\theta \approx 90°$, while the flow separated from the fins at $\theta \gtrsim 120°$, using the angle θ from the inflow defined in Figure (2) in section 2.2. The conclusion by Nemati et al. [53] pointed to the Transition SST model for low Reynolds numbers, although all the turbulence models mentioned above performed admirably. They also pointed to the Spalart-Allmaras turbulence model for being reasonably accurate and at the same time requiring less computational power.

The results by Nemati et al. [53] are in good agreement with more general studies found in the literature (like test cases with an adverse pressure gradient and/or flow separation [44, 3, 4] or more complex external flow [47], both of which have many of the same challenges in turbulence modelling as for finned-tubes). These studies usually point to the $k-\omega SST$ model or the Realizable $k-\epsilon$ model as the most general turbulence model with the best agreement with experimental data. The SA model usually comes out below these, but with better performance than the standard $k-\epsilon$ model. Some of the studies (e.g. [3]) also show RSM models, like the LLR turbulence model, to not perform any better than the turbulent viscosity models.

These results are, of course, not directly comparable to the modelling of finned-tubes, since they do not solve the energy equation (see equation (25)). The general agreement between these results and the result by Nemati et al. [53] do, however, point to the $k-\omega SST$ model and the Realizable $k-\epsilon$ model as the most suitable models. The fact that the Realizable $k-\epsilon$ model is one of the recurring models in the comparison by Lindqvist [33] of previous studies also underlines this.

No comparison between the LLR RSM turbulence model and the other turbulent viscosity models for flow over finned-tubes have been found. The more general cases show, as mentioned, that it does not necessarily show higher accuracy. This also fits well with the description of the LRR model by Versteeg et al.[70] mentioned above. How this extends to and influences the calculation of temperature is not clear.

The Transition SST model is expected to behave like the $k-\omega SST$ model, but with higher accuracy at lower Reynolds numbers. This is because the Transition SST model is an extension of the $k-\omega SST$ model more suitable for partially laminar boundary layers. In fully turbulent flow the models are identical. This improved prediction at lower Reynolds numbers was pointed out by Nemati et al. [53]. The difference between the Transition SST and $k-\omega SST$ model was around 6% for Eu and 2.5% for Nu in the results by Nemati et al. [53], with the result for the Transition SST model being closer to the correlations they used for comparison. It is, however, worth mentioning that this difference is less than the difference between the Transition SST model and another transition model tested by Nemati et al. [53].

2.2 Distribution of the heat transfer coefficient over the fin

An uneven distribution of the heat transfer coefficient over the fins is a known phenomenon and is caused by the uneven distribution of the flow over the finned-tubes [69, 48]. In this section, a description of the local heat transfer coefficient over a annular fin is presented, and to understand the distribution of the local heat transfer coefficient, a description of the local flow over the fin is also presented.

A definition of an angle, θ, from the inflow is used to describe the local heat transfer and flow behaviour, θ is shown in Figure (2).

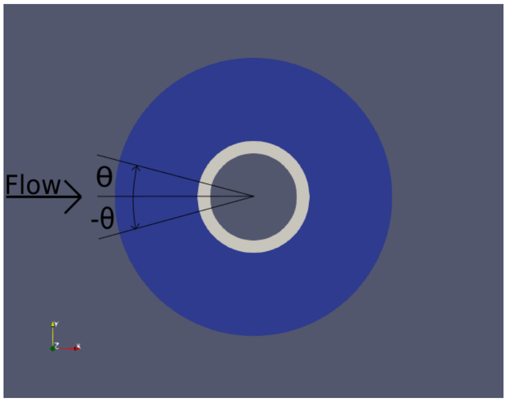

Figure 2: Definition of the angle θ going from $0° < \theta < \pm 180°$ from the inflow

And as can be seen from Figure (2), the angle is defined from $\theta = 0°$ up to $\theta = \pm 180°$.

Measuring the local heat transfer coefficient over a fin can be done with different methods. The first methods used to do this were the point heating and total heating methods. In the point heating method, a section of the fin is heated with a uniform heat flux. The local temperature and local heat flux are then measured using thermocouples when the fin is cooled by the flow. From this, the local heat transfer coefficient can be calculated. Since only a part of the fin is heated, the thermal boundary layer development in the point heating method is wrong. This in turn can lead to an overprediction of the local heat transfer coefficient [27].

The total heating method is to this extent more realistic. In this method, the fin is heated from the base, and the local heat flux and the local temperature distribution is measured when the fin is cooled by the flow. From this, the local heat transfer coefficient can be calculated. The method does, however, rely on apparatus which intrudes into the flow and disturbs it. This can then lead to unrealistic flow behaviour and thus an unrealistic distribution of the heat transfer coefficient [27, 48]. The resolution over the fin in these two methods are also limited by the number of sensors used [18].

A more modern method using the same principle is utilising infrared technology. In a study by Vintrou et al. [71], the fin was heated by an infrared emitter. As the fin is cooled by the flow, an infrared camera is used to find the temperature distribution over the fin. From the temperature distribution, the distribution of the heat transfer coefficient can be calculated. This gives a much higher spatial resolution over the fin and does not disturb the flow.

The local distribution of the heat transfer coefficient can also be studied through similarity to the local mass transfer coefficient. Here the fin is covered in a layer of naphthalene which goes directly from solid to gas into the flow (i.e., sublimation). The local mass transfer coefficient can then be determined by measuring the weight and registering contours before and after the experiment. The method, called naphthalene sublimation, does therefore not interfere with the flow [27, 18]. Since the method involves weighing and registering contours, the uncertainty in the method is highest where the mass transfer is lowest [27]. It is worth pointing out that this method assumes that the fin has a constant temperature. How this interfere with the distribution of the heat transfer coefficient is unclear. However, according to Kearney and Jacobi [27], the effect should be small, meaning the distribution should be realistic.

With the advancement of CFD, experimental studies using the methods described above to study the local heat transfer coefficient seems to get sparser. In CFD, the local distribution of the heat transfer coefficient is much more readily available, and easy to calculate from the results. In experimental studies, it is difficult to have a good enough resolution to be able to describe the local heat transfer coefficient accurately. However, such studies are still very much needed. Both to understand the distribution of the heat transfer coefficient, but also for validation of CFD models. A CFD model validated by experimental results can then be a powerful tool in studying the distribution of the heat transfer coefficient and how it is influenced by changes in the bundle geometry [71].

The local flow development is influenced by the layout of the finned-tube bundle, and the local heat transfer coefficient is governed by the local flow over the fin. In the literature presented below, a distinction is therefore made between the distribution over a fin in one row of finned-tubes, and for a fin in a bundle with a staggered layout and with an in-line layout. As the local distribution of the heat transfer coefficient is governed by the local flow, there is first a description of the flow development over the fin in order for the distribution of the heat transfer coefficient to be understandable. Only studies using non-intrusive methods to describe the distribution of the heat transfer coefficient are presented.

One row of finned-tubes

The flow development over a fin is schematically shown in Figure (3).

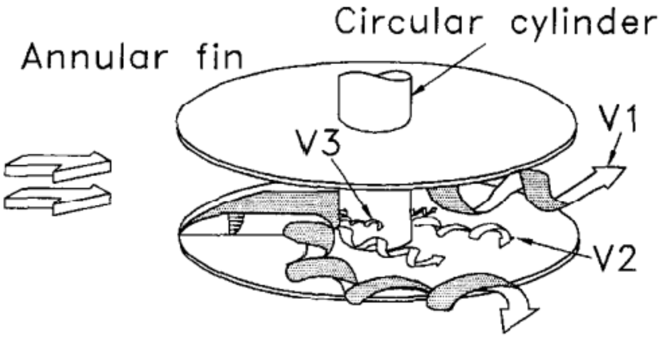

Figure 3: Flow over an annular finned-tube showing schematically the boundary layer development and separation into horseshoe vortices. V1 is the primary vortex, and V2 and V3 secondary vortices. (Figure taken from Sung et al. [67])

Figure (3) is taken from Sung et al. [67] and depicts the boundary layer development from the leading edge of the fin towards the tube. Although not depicted, the development of the boundary layer happens from the leading edge of the fin ($\theta = 0°$) up to around $\theta = \pm 90°$ [27].

As the growing boundary layer gets nearer to the base of the fin, the flow gets pushed away and starts separating due to the adverse pressure gradient caused by the tube. As depicted in Figure (3), this separation forms a system of vortices, called horseshoe vortices. The name horseshoe vortices come from the "horseshoe" shape they form around the tube. The flow moves the vortices downstream creating the symmetrical legs of the horseshoe vortices on each side of the tube. This results in high mixing of the flow [27].

The number of horseshoe vortices that are formed depends on the Reynolds number [71]. V1 in Figure (3) depicts the primary vortex caused by the separation of the main flow around the tube. While V2 is a smaller secondary vortex caused by the secondary flow near the base of the fin. At higher Reynolds numbers, an even smaller vortex, V3, can occur [67].

The separation of the horseshoe vortices from the tube happen around $\theta = \pm 90°$, moving a little further back at higher Reynolds numbers [27]. Due to the separation of the flow, a recirculating wake is formed behind the tube, between the legs of the horseshoe vortices. Figure (5), shows this recirculating wake zone schematically. In the wake, the flow is near stagnant, and recirculation can lead to backflow impinging the trailing edge of the fin.

At high Reynolds numbers, separation can also occur at the leading edge of the fin, with subsequent reattachment a little on to the fin [18]. Hu and Jacobi [18] found this to happen for $Re_{dh} > 9000$.

It is worth pointing out that Figure (3) is representative of flow over finned-tubes with a large fin pitch, where the boundary layers over the fins develop independently of each other. For a smaller fin pitch, Sung et al. [67] found the flow to be more complex with higher levels of secondary flow and more secondary vortices. In such situations, the boundary layer developing over the fin meets with the boundary layer from the underside of the fin above, and the main flow does not reach the tube [67, 48]. The investigation by Sung et al. [67] was performed at relatively high Reynolds numbers, at lower Reynolds number secondary flow is less prevalent [67, 71].

The development of the local heat transfer coefficient is governed by the local flow development described above. Studying the distribution of the mass transfer coefficient over a row of annular finned-tubes, Hu and Jacobi [18] used the naphthalene sublimation technique. As mentioned above, this is an indirect method of studying the local heat transfer coefficient, where the local Sherwood number (Sh), describing the mass transfer, can be related to the local Nusselt number using the relation:

$$Nu = Sh \cdot \left(\frac{Pr}{Sc}\right)^{1/3} \tag{11}$$

where Sc is the Schmidt number. Sc is analogous to the Prandtl number (Pr), but describing the ratio of momentum diffusivity to mass diffusivity instead of momentum diffusivity to thermal diffusivity [21].

Hu and Jacobi [18] studied the distribution of the local mass transfer coefficient at a range of Reynolds numbers $3000 \lesssim Re_{dh} \lesssim 12000$, where Re_{dh} is the Reynolds number evaluated using the hydraulic diameter. Their results for the local mass transfer coefficient over the fin are shown for two different Reynolds numbers in Figure (4), along with the local flow phenomena causing the mass transfer coefficient distribution.

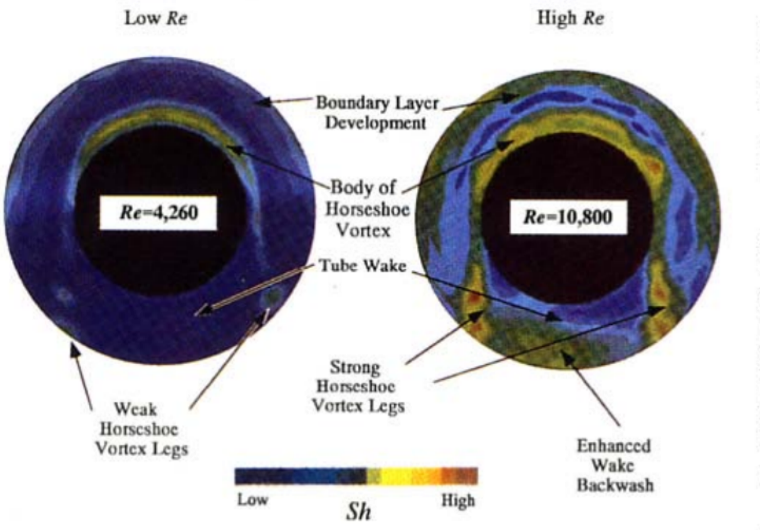

Figure 4: Distribution of the mass transfer coefficient (Sh) over the fin from the results of Hu and Jacobi [18], with the in-flow coming from the top (Figure collected from Kearney and Jacobi [26])

In the lower Reynolds number result shown to the left in Figure (4), a locally higher mass transfer coefficient, due to flow impingement, is visible at the leading edge of the fin up to around $\theta = \pm 90°$. A locally higher mass transfer coefficient, due to horseshoe vortices, is also found near the base of the fin [18]. At the lowest Reynolds number investigated by Hu and Jacobi [18], $Re_{dh} = 3000$, the increase in the mass transfer coefficient near the base of the fin was observed by Hu and Jacobi [18] up to $\theta = \pm 30°$. While for the slightly higher Reynolds number shown to the left in Figure (4), the increase is visible up to $\theta \approx \pm 60°$. Figure (4) also shows the beginning of enhancement in the mass transfer coefficient in the legs of the horseshoe vortices, which was not present for $Re_{dh} = 3000$ in the study by Hu and Jacobi [18]. Hu and Jacobi [18] also found a low mass transfer coefficient behind the tube between $\theta = \pm 140°$, due to the wake.

As the Reynolds number increases, an increase in the mass transfer at the trailing edge of the fin in the area $\theta = \pm 170°$, due to backflow, was also observed by Hu and Jacobi [18]. This is visible in the higher Reynolds number result to the right in Figure (4).

At Reynolds number higher than $Re_{d_h} = 9000$, Hu and Jacobi [18] observed a change in the position of the maximum mass flux from the leading edge to a little further back on the fin. According to Hu and Jacobi [18], this is an indication of leading-edge separation from the fin, with the new maximum being where the flow re-attaches to the fin.

Kearney and Jacobi [26, 27] did one of the more extensive investigations of the distribution of the mass transfer coefficient over an annular fin. They investigated the distribution of the mass transfer coefficient over a fin in a single row of finned-tubes, and in the second row of a finned-tube bundle with both a staggered layout and an in-line layout. The studies by Kearney and Jacobi [26, 27] builds on the work by Hu and Jacobi [18].

In their experiments of a fin in one row of finned-tubes, Kearney and Jacobi [27] found an increase in the local mass transfer coefficient at the leading edge and near the base of the fin. Both visible from $\theta = 0°$ up to around $\theta = \pm 90°$ [27]. Kearney and Jacobi [27] also observed a decrease in the local mass transfer coefficient in the wake behind the tube. This is very similar to the result by Hu and Jacobi [18], shown in Figure (4).

Increasing the Reynolds number, Kearney and Jacobi [27] found the increases in mass transfer at the rear part of the fin to be comparably higher than at the front of the fin. According to Kearney and Jacobi [27], this came from both an increase in backflow and from higher mass transfer in the legs of the horseshoe vortices. This more evenly distributed mass transfer coefficient is, to a degree, also visible in the higher Reynolds number result by Hu and Jacobi [18] on the right in Figure (4).

Tube bundle with a staggered layout

The flow over the finned-tubes in a staggered bundle is very similar to flow over a single row of finned-tubes described above. From where the flow impinges, a boundary layer starts growing, and as the boundary layer nears the bases of the fin, horseshoe vortices form around the tube (as seen in Figure (3)). Behind the tube, a recirculating wake forms due to the separation of the flow, as depicted in Figure (5) [26].

Figure (5) is a schematic representation of the flow distribution over a finned-tube in a bundle with a staggered layout showing the separation of the flow and subsequent wake behind the tube [48].

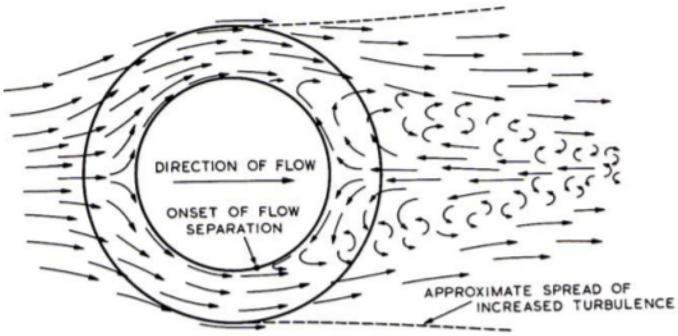

Figure 5: Schematic flow representation over a finned-tube in a staggered bundle from Neal and Hitchcock (1966) (collected from Mon [48])

There are, however, some differences in the flow, both between a single row of finned-tubes and a finned-tube bundle with a staggered layout and between the different rows in the bundle. The flow over the first row is almost identical to the flow over one row of finned-tubes, this is true for an in-line layout as well [27].

Figure (6) shows a schematic representation of the bulk flow in a finned-tube bundle with a staggered layout.

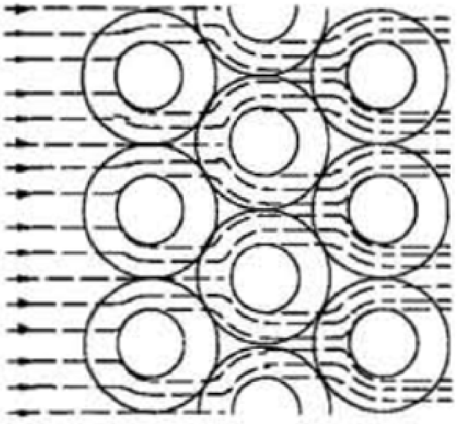

Figure 6: Schematic representation of the bulk flow over the finned-tubes in a bundle with a staggered layout. (Figure taken from Kearney and Jacobi [26])

As depicted with an area with no streamlines behind the finned-tubes in Figure (6), the flow from the second row onwards is influenced by the wake of the preceding row. Due to the blockage effect of the preceding row, the main flow does not hit the entire fin. The edge of the fin around $\theta = \pm 90^\circ$ is in the wake of the row before. How much of the fins are in the wake of the preceding row depends on the geometry. Kearney and Jacobi [26] found flow impingement from the leading edge only up to around $\theta = \pm 20^\circ$.

The separation of the horseshoe vortices from the tube (as depicted in Figure (3)), happens around $\theta = \pm 90^\circ$, but is, as for the one-row case, dependent on the Reynolds number [48, 53, 27]. According to Mon [48], Neal and Hitchcock (1966) also found that the separation point moves further back for rows deeper into the bundle. Investigating different turbulence models for use in numerical simulations of flow over a finned-tube bundle, Nemati et al. [53] found the separation from the fin to be at $\theta \gtrsim \pm 120^\circ$ for all the model, as described in section 2.1.

Although not clearly depicted in Figure (6), the flow develops through the bundle, with the flow from the second row onwards being characterised by good mixing, due to the wakes of the preceding rows and the separation of horseshoe vortices [27, 48].

The local heat transfer coefficient is governed by the local flow, and the heat transfer coefficient is expected to be more uniformly distributed for a bundle compared to a single row of finned-tubes since the flow is better mixed [48].

Vintrou et al. [71] investigated the local heat transfer behaviour of a fin in the middle row of a staggered three-row finned-tube bundle using infrared technology. The fin was first heated with an infrared emitter. The temperature distribution over the fin was then captured with an infrared camera while the flow cooled the fin. From the distribution of the temperature, the local heat transfer coefficient (in terms of the local Nusselt number) over the fin can be calculated. This led to a partially numerical method using numerical integration to get from the temperature to the heat transfer coefficient [71]. The highest uncertainty using this method is, according to Vintrou et al.[71], in the wake region behind the tube, and the uncertainty increases as the Reynolds number gets lower.

The results by Vintrou et al. [71] for the distribution of the local Nu at $Re_{d_o} = 1885$ (left) and $Re_{d_o} = 3638$

(right) are shown in Figure (7). As can be seen from Figure (7), increasing the Reynolds number, increases the heat transfer, changes the wake zone, and makes the flow seemingly more complex.

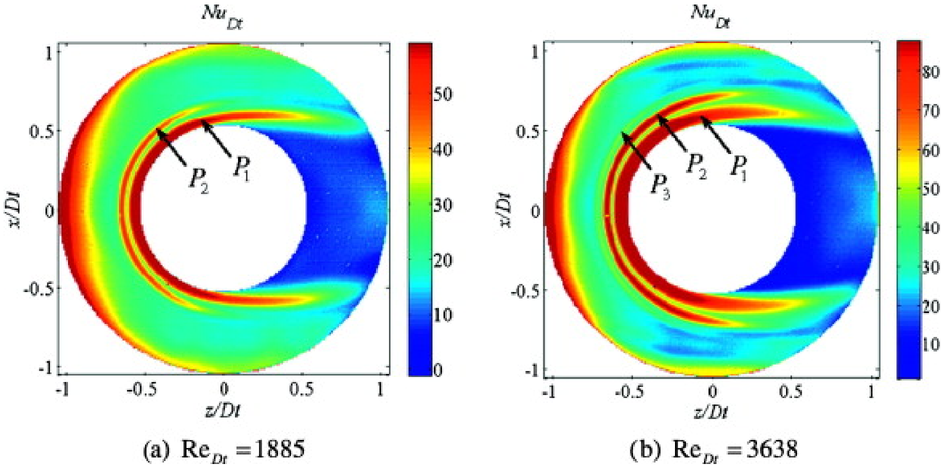

Figure 7: Results by Vintrou et al. [71] showing the distribution of Nu (called Nu_{Dt} in the figure) over the fin in the second row of a staggered finned-tube bundle at two different Re_{d_o} (called Re_{Dt}). P is the position of horseshoe vortices and Dt is the tube diameter. The inflow comes from the left. (Figure taken from Vintrou et al. [71])

As can be seen in the results by Vintrou et al. [71] shown in Figure (7), there is a local maximum of Nu at the leading edge of the fin. This decreases towards the base of the fin as the boundary layer develops. Near the base of the fin, Nu increases again, due to the development of horseshoe vortices. Figure (7) shows that more than one primary horseshoe vortex (P) is responsible for the increases. According to Vintrou et al. [71], these are not the same as secondary vortices (shown in Figure (3) by Sung et al. [67] as V2), but the next primary vortex (V1 in Figure (3) by Sung et al. [67]) starting to develop before the first vortex has separated from the tube. Increasing the Reynolds number increases the number of horseshoe vortices, but also results in stronger horseshoe vortices. Figure (7) shows the increase in Nu due to the horseshoe vortices up to the separation point around $\theta = \pm 90°$. Above this angle, an increase in Nu is visible in the legs of the horseshoe vortices but this decreases towards the trailing edge of the fin.

Boundary layer development from the edge of the fin is visible in Figure (7) up to around $\theta = \pm 90°$. The increase in the heat transfer a little to each side of the leading edge is, however, much smaller due to the wake of the preceding row, as can be seen in Figure (7). As seen in Figure (7), the lowest Nu is found in the wake behind the tube. At $\theta \approx \pm 180°$ an increase in Nu, near the trailing edge of the fin, is again visible in Figure (7) due to backflow.

Kearney and Jacobi [26] found similar results to Vintrou et al. [71] in their experimental study of a fin in a two-row staggered annular finned-tube bundle. They used naphthalene sublimation to find the local heat transfer coefficient through analogy to the mass transfer coefficient.

The results by Kearney and Jacobi [26] for the distribution of the local mass transfer coefficient over a fin in the second row at two different Reynolds numbers are shown in Figure (8).

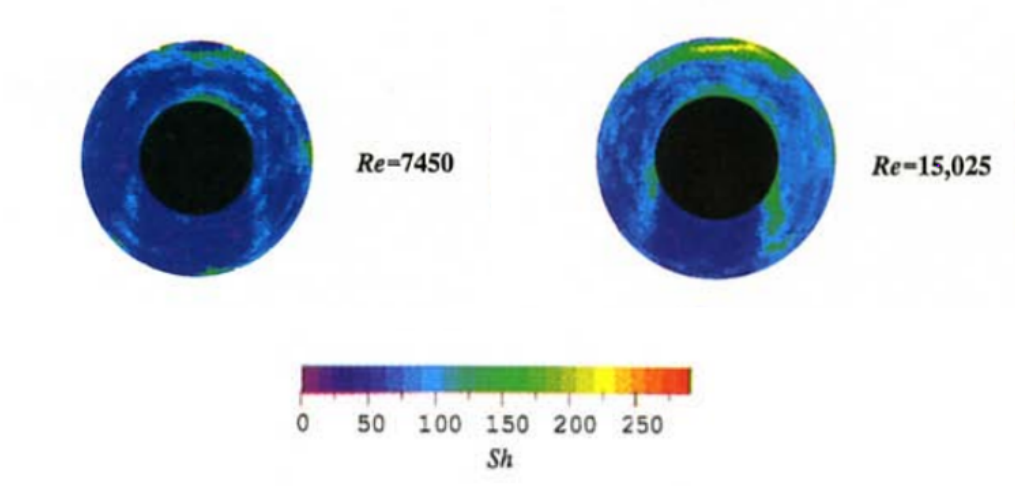

Figure 8: Distribution of the mass transfer coefficient (Sh) in a staggered tube bundle from the results of Kearney and Jacobi [26]. The inflow comes in from the top. (Figure adapted from a figure by Kearney and Jacobi [26])

A local maximum of the mass transfer coefficient was observed by Kearney and Jacobi [26] from the leading edge of the fin up to around $\theta = \pm 20°$ due to the flow impingement, as seen most clearly in the higher Reynolds number result by Kearney and Jacobi [26], to the right, in Figure (8). A subsequent decrease in the mass transfer coefficient is also visible in Figure (8) going towards the base of the fin, due to the growth of the boundary layer.

Due to the wake region behind the first row, the local mass transfer coefficient at the edge of the fin from $\theta = \pm 20°$ up to $\theta = \pm 90°$ is comparably less than for a single row of finned-tubes. This can be seen if the results by Kearney and Jacobi [26] shown in Figure (8) is compared with the one-row results by Hu and Jacobi [18] shown in Figure (4).

Near the frontal base of the fin, a higher local mass transfer coefficient is visible in Figure (8). This is, again, caused by the formation and subsequent separation of the horseshoe vortices from the tube. As the horseshoe vortices are moved with the flow downstream, a higher mass transfer coefficient is also visible in the legs of the vortices due to the enhanced mixing of the flow [26]. As seen in Figure (8), this mixing and subsequent enhancement of the local mass transfer coefficient increases with increasing Reynolds numbers.

A region of lower mass transfer behind the tube, due to the wake, is also visible in the results by Kearney and Jacobi [26] shown in Figure (8).

At higher Reynolds numbers, Kearney and Jacobi [26] also observed a slight increase in the mass transfer coefficient at the trailing edge of the fin due to backflow. This is easier to see in results by Kearney and Jacobi [26] at higher Reynolds numbers than what is shown in Figure (8).

It is worth pointing out that for the second row in a finned-tube bundle with a staggered layout, some of the flow impinging the leading edge of the fin is the undisturbed inflow. This in turn increases the local heat transfer coefficient at the leading edge. This effect is only present for the second row, and the flow further into the tube bundle is expected to be better mixed and a little more uniformly distributed [48].

Tube bundle with an in-line layout

The flow in a finned-tube bundle with an in-line layout is characterised by the same flow phenomena as with a staggered layout. There are, however, some differences in where these phenomena occur [26]. In Figure

(9), a schematic representation of the bulk flow in a finned-tube bundle with an in-line layout is depicted. The figure is taken from Kearney and Jacobi [26].

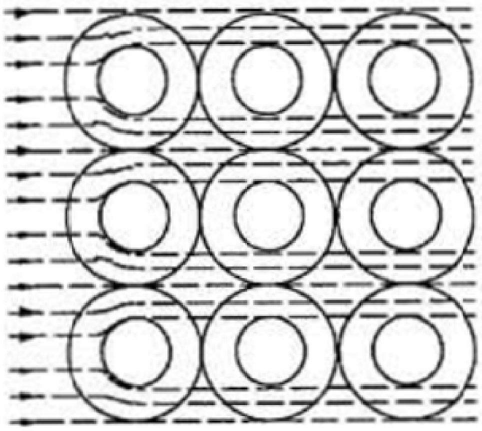

Figure 9: Schematic representation of flow over the finned-tubes in a tube bundle with an in-line layout. (Figure taken from Kearney and Jacobi [26])

As can be seen in Figure (9), the flow from the second row onwards do not impinge directly at the leading edge of the fin ($\theta = 0°$), but a little to each side, due to the finned-tubes being situated right behind each other. From where the flow impinges a boundary layer develops in the same way as for a staggered layout [26].

Horseshoe vortices develop, as for a staggered layout, when the developing boundary layer gets pushed away from the base of the fin due to the adverse pressure gradient caused by the tube (as shown in Figure (3)). These horseshoe vortices are, however, weaker compared to a finned-tube bundle with a staggered layout since the flow do not impinge at the leading edge of the fins. Instead, the leading edge of the fins is in the recirculating wake of the preceding row. This wake is similar to the wake for a staggered layout shown in Figure (5). As a consequence, both the leading and trailing edge of the fin is engulfed in the recirculating, slow-moving wake [26, 27, 48].

A finned-tube bundle with an in-line layout also has more bypass flow compared to a staggered layout, where the flow flows in the open area between the finned-tubes. This results in a less mixed, jet-like flow [17]. It is worth pointing out that in most finned-tube bundles, as oppose to what is shown in Figures (9) and (6), the fins do not touch, meaning there is an open area between the finned-tubes.

Using naphthalene sublimation, Kearney and Jacobi [26, 27] also described the distribution of the local mass transfer coefficient over the fin in a finned tube bundle with an in-line layout. This is the only experimental study found investigating the local heat/mass transfer coefficient in a finned-tube bundle with an in-line layout.

In calculating the overall heat transfer coefficient from the local distribution of the mass transfer coefficient, Kearney and Jacobi [27] found their results for an in-line layout to overpredicted the correlations they used for comparison. Kearney and Jacobi [27] argued that this partly comes from an error in using ΔT_{LM} (see equation (35) in section 3.6) for an in-line bundle resulting in the actual ΔT being overpredicted. This, according to Kearney and Jacobi [27], makes the correlations underpredict the real heat transfer coefficient for an in-line layout.

For the results by Kearney and Jacobi [27, 26] for the finned-tube bundle with a staggered layout and for the one-row of finned-tubes, Kearney and Jacobi [27] found the calculated overall heat transfer coefficient to match with the correlations much better. This in turn was used by Kearney and Jacobi [27] as validation for the whole experiment, including the results for the in-line layout.

The results by Kearney and Jacobi [26] for the local mass transfer coefficient are shown in Figure (10). The results are for a fin in the second row of a two-row finned-tube bundle with an in-line layout.

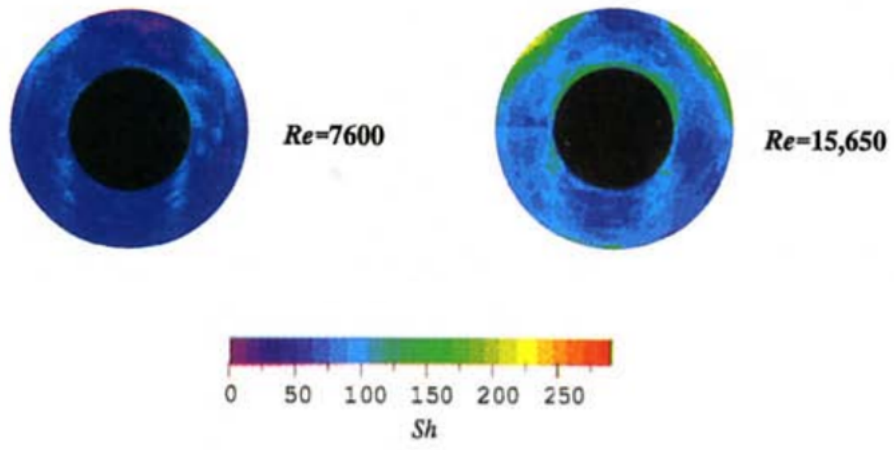

Figure 10: Distribution of the mass transfer coefficient (Sh) in an in-line tube bundle from the results of Kearney and Jacobi [26]. The inflow comes in from the top (Figure adapted from a figure by Kearney and Jacobi [26])

As seen in Figure (10), a low mass transfer coefficient is found at the leading edge of the fin. This is caused by the wake of the preceding row. Where the flow, not blocked by the preceding row, impinges the edge of the fin, Kearney and Jacobi [26] observed a higher local mass transfer coefficient. This is most clearly visible for the higher Reynolds number result in Figure (10) and can be seen at the edge of the fin from $\theta \approx \pm 20°$ all the way up to $\theta \approx \pm 90°$ [26].

This is a clear difference from the results by Kearney and Jacobi [26] for a staggered finned-tube bundle. For a staggered layout, the increased local mass transfer coefficient due to flow impingement is visible at the leading edge fin up to around $\theta = \pm 20°$ [26], as seen in Figure (8).

From where the flow impinges the edge of the fin, the local mass transfer coefficient decreases as the boundary layer grows, as seen in Figure (10). Near the base of the fin, from $\theta = 0°$ up to $\theta = \pm 90°$, the local mass transfer coefficient increases again due to the formation of horseshoe vortices around the tube [26]. This is most clear to see in the higher Reynolds number result in Figure (10). As mentioned above, the horseshoe vortices forming in an in-line layout are weaker than the ones found in a comparable finned-tube bundle with a staggered layout [26].

Kearney and Jacobi [26] also found an increase in the local heat transfer coefficient in the legs of the horseshoe vortices. As seen in Figure (10), this effect is more prominent for the lower Reynolds number result.

An area of lower mass transfer is evident behind the tube due to the wake, as seen in Figure (10). For a bundle with more than two rows, this wake then influences the leading edge of the fin in the next row as well. Kearney and Jacobi [26, 27] did, however, find the wake found in the in-line layout to have higher mass transfer compared to a staggered layout. This can be seen if the results by Kearney and Jacobi [26] at $Re \approx 15000$, shown if Figure (10) for an in-line layout and in Figure (8) for a staggered layout, are compared.

The difference in the distribution of the heat transfer coefficient between an in-line and staggered layout means the in-line layout usually has a lower overall heat transfer coefficient [69, 26]. Kearney and Jacobi [26] did however point out that for a shallow finned-tube bundle with high fins, an in-line layout can achieve a comparable overall heat transfer coefficient to a staggered layout, and with a smaller pressure drop. According to Kearney and Jacobi [26], this is because a large part of the overall heat transfer in a staggered finned-tube bundle comes from the horseshoe vortices, which are confined to a specific area. In an in-line layout, most of the heat transfer comes from the boundary layer development from where the flow impinges. Higher fins protrude further into the jet-like flow between the finned-tubes. This gives a larger area where boundary layers can develop. For a finned-tube bundle with a staggered layout, these areas of the fins are in the wake of the preceding row [26].

2.3 Row-by-row development of the heat transfer coefficient

In this section, an investigation of literature regarding the number of rows until the row-by-row heat transfer coefficient becomes constant is performed. The focus will be on a generic staggered tube bundle, but with the difference to an in-line layout being described.

The row-by-row heat transfer coefficient in a finned-tube bundle is expected to become constant when the number of rows in the bundle increases. This is because the flow develops due to mixing over the first rows. In subsequent rows, the flow reaches a more stabilised state where the temperature in the flow is relatively uniformly distributed [69, 36].

In CFD, increasing the number of rows increases the computational cost of the simulation, so modelling more rows than necessary is wasteful. When the flow in the tube bundle does not develop anymore, no more information is gained by modelling more rows.

In section 2.2 differences in the distribution of the flow and of the heat transfer coefficient over the fins between an in-line and a staggered layout are described. These differences are also evident in the development of the row-by-row heat transfer coefficient, and are well represented in the simulation results by Mon [48] shown in Figure (11).

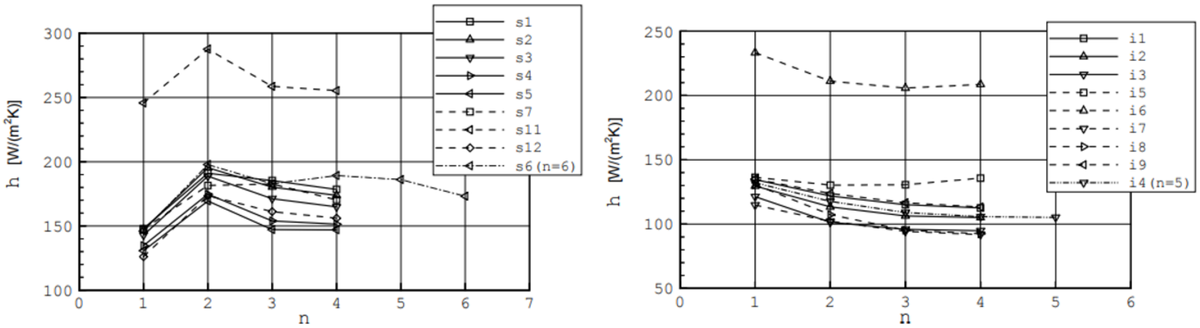

Figure 11: Row-by-row results by Mon [48] for the heat transfer coefficient for a staggered layout (left) and for an in-line layout (right) at $Re_{do} = 43000$ (Figure adapted from a figure by Mon [48])

Figure (11) shows the results by Mon [48] for the row-by-row heat transfer coefficient for both a staggered layout (on the left in Figure (11)) and an in-line layout (on the right in Figure (11)).

For a staggered layout, the heat transfer coefficient increases from the first to the second row where a maximum is usually found. The heat transfer coefficient then decreases towards a constant value as the number of rows increases, as shown in Figure (11). The maximum found at the second row comes from the accelerated jet of undisturbed inflow impinging the leading edge of the fin, while the decrease in the row-by-row heat transfer coefficient for subsequent rows comes from the mixing of the flow. The first row usually has the lowest heat transfer coefficient due to being impinged by the non-accelerated inflow [36, 69]. How much lower the heat transfer coefficient for the first row is, varies in the literature. E.g. in the simulation results by Mon [48] shown in Figure (11) and in the simulation results by Lindqvist et al. [36] shown in Figure (13), the first row has a heat transfer coefficient between 80% and 90% of the last row. In the row correction factor by Weierman [73], this value is, however, around 70%.

For an in-line layout the row-by-row heat transfer coefficient is expected to have the highest value for the first row, then gradually decrease as the number of rows increases. This behaviour is seen in the simulation results by Mon [48] with an in-line layout shown (to the right) in Figure (11). The overall heat transfer coefficient is also generally lower for an in-line layout compared to a staggered layout [69].

The development of the flow through the tube bundle not only influences the row-by-row heat transfer coefficient but also the row-by-row pressure drop. This is a topic that seems to have been studied less than the row-by-row development of the heat transfer coefficient.

In a comparison made by Klynderud [69], the row-by-row development of the pressure drop from different studies were compared. The comparison by Klynderud [69] showed the row variation for the pressure drop to be less than 6% in all but one of the studies. The exception in the comparison by Klynderud [69], was a study by Weierman [73] proposing correction factors for different geometry parameters. The row-by-row correction for the pressure drop proposed by Weierman [74] is dependent on tube bundle geometry, and depending on the geometry, the pressure drop can both increase and decrease row-by-row [73, 20].

Gianolio et al. [6] studied experimentally a staggered six-row solid finned-tube bundle with both a forced and an induced draft setup. Forced draft describes a situation where the flow is being pushed through the bundle, while induced draft is the opposite. The results by Gianolio et al. [6] for both forced and induced draft are shown in Figure (12).

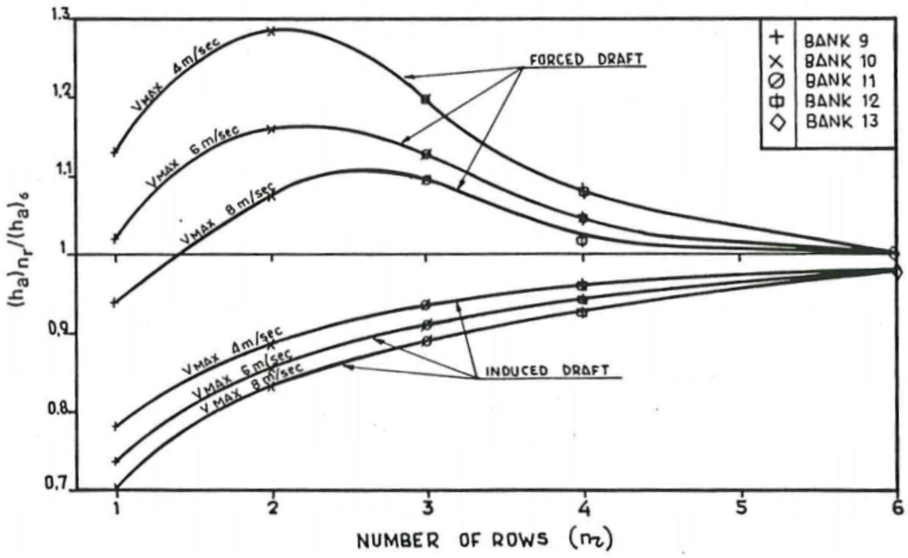

Figure 12: Row-by-row results by Gianolio and Cuti [6] for the heat transfer coefficient for a forced and an induced draft setup. The results are normalised with the result for the last row forced draft result (Figure collected from Gianolio and Cuti [6])

For the induced draft setup, the results by Gianolio et al. [6] show the row-by-row heat transfer coefficient to grow asymptotically towards a maximum value, with the first row having the lowest heat transfer coefficient, as can be seen in Figure (12). This difference in the behaviour compared to the forced draft setup is caused by the calming effect of the induced draft setup, resulting in less flow mixing [6]. The results by Gianolio et al. [6] still shows some change in the row-by-row heat transfer coefficient between the fifth and sixth row. However, as can be seen in Figure (12), these changes are relatively minor compared to the first rows.

Eckels and Rabas [7] found the same trend as in the results by Gianolio et al. [6] shown in Figure (12) investigating a similar bundle with an induced draft setup. The results by Eckels and Rabas [7] showed the same growth of the row-by-row heat transfer coefficient towards an asymptotic value. This value was, however, shown by Eckels and Rabas [7] to be reached after around four rows, depending somewhat on the Reynolds number.

Most finned-tube heat exchangers use a forced draft setup, and all the studies presented below are for a forced draft setup. The results of Gianolio et al. [6] for a forced draft setup shown in Figure (12) follow the development for a staggered tube bundle described at the start of this section. As can be seen in Figure (12), the results of Gianolio et al. [6] show the row-by-row heat transfer coefficient to reach a maximum at the second row, then decrease towards an asymptotic value. This value is, however, below the heat transfer coefficient for the first row, as can be seen in Figure (12). The results by Gianolio et al. [6] still shows some change in the row-by-row heat transfer coefficient between the fifth and sixth row. However, as can be seen in Figure (12), these changes are relatively minor compared to the first rows.

Hofmann et al. [15] proposed a correction factor based on their own experimental results from an eight-row finned-tube bundle. This row correction factor was developed from the average row-by-row heat transfer coefficient from their results. The row-by-row development of this row correction factor is shown in Figure (13) alongside the numerical results by Lindqvist et al. [36]. As can be seen in Figure (13), the correction factor does not reach unity until the eighth row. This means the row-by-row heat transfer coefficient does not reach a constant value, and that the number of rows before a constant value is reached is eight or more. It should be mentioned that the heat transfer coefficient was only calculated for every other row in the study by Hofmann et al. [15]. This means the row-by-row heat transfer coefficient could have reached a constant value after seven rows without this being visible in the row correction factor by Hofmann et al. [15]. The experimental results by Hofmann et al. [15] also varies significantly from the average value they used for the row correction factor, and at lower Reynolds numbers ($Re_{d_o} \lesssim 7000$) their results were more or less constant from the fourth row onwards [15].

Hofmann et al. [15] compared their row correction factor with other published row correction factors. The comparison by Hofmann et al. [15] show their row correction factor to be among the slowest to develop towards unity, and the row correction factor by Mon [48] to be the fastest. The row correction factor by Mon [48] is described later in this section and also shown in Figure (13). Hofmann et al. [15] also developed a correlation from their experiments. In a subsequent paper, Hofmann et al. [16], did CFD simulations of one row of finned-tubes. The numerical results by Hofmann et al. [16] were shown to agree with this correlation if corrected to be valid for one row using the correction factor they developed.

Mon [48] investigated both a staggered and an in-line tube bundle numerically and the results are shown in Figure (11). For a staggered layout, shown to the left in Figure (11), the row-by-row heat transfer coefficient reaches a constant value between the third and the fourth row. This value was relatively consistent between all the different staggered geometries simulated, as can be seen in Figure (11), and, according to Mon [48], for all the simulated Reynolds numbers. Most of the simulations by Mon [48] used a tube bundle with four rows, although some simulations using five or six rows were also conducted by Mon [48], as can be seen in Figure (11).

The simulation results by Mon [48] using an in-line tube layout are shown to the right in Figure (11). As can be seen in Figure (11), the heat transfer coefficient for an in-line layout has the highest value for the first row and then decreases towards an asymptotic value as the number of rows increases. Most of the variation in the in-line row-by-row results for the heat transfer coefficient by Mon [48] happens between the first and second row, as can be seen in Figure (11). Although, according to Mon [48], the heat transfer coefficient was not constant until the fourth row.

Both the results for a staggered and for in-line layout were compared with the literature by Mon [48]. According to Mon [48], the results shown in Figure (11) are in good agreement with the experimental results by Ward and Young [72] for a staggered layout and by Brauer (1961) for an in-line layout. It is, however, worth pointing out that a literature review by Mon [48] show other studies to have different results. As shown by Mon [48], the variation for a tube bundle with a staggered layout ranged from two to three rows (Kuntysh et al. (1980 and 1993) and Antuf'ev et al (1968)) up to five to six rows (Mirkovic (1974) and Neal and Hitchcock (1966)) before the heat transfer coefficient becomes constant. For an in-line layout, studies by both Antuf'ev et al (1968) and Kuntysh et al. (1993) show, according to Mon [48], the row-by-row heat transfer coefficient to be constant from the second row onwards.

Mon [48] developed a correlation for Nu for both a finned-tube bundle with an in-line and with a staggered layout, based on her own numerical results. These correlations were based on an already existing correlation from the VDI Heat atlas [48]. The correlations are valid for four or more rows, which are, according to Mon's [48] results, a bundle where the row-by-row heat transfer coefficient has reached a constant value. To extend the validity of the correlations, a row correction factor for fewer rows was introduced by Mon [48].

Lindqvist et al. [36] compared the row-by-row development of the row correction factor by Mon [48] with results from their own numerical simulations. These numerical simulations by Lindqvist et al. [36] were performed with an eight-row finned-tube bundle at a wide range of Reynolds numbers. Lindqvist et al. [36] also compared their numerical results with the row correction by Hofmann et al. [15] described above and with a row correction factor from ESCOA [36].

Figure (13), taken from Lindqvist et al. [36], shows the cumulative row-by-row heat transfer coefficient from the simulation results by Lindqvist et al. [36] alongside the row correction factors.

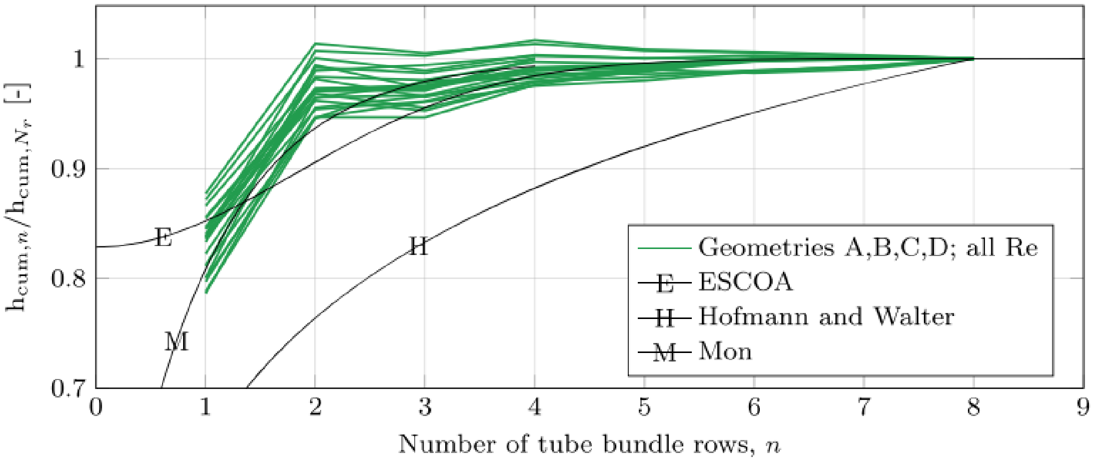

Figure 13: Cumulative row-by-row results by Lindqvist et al. [36] for the heat transfer coefficient. The results are normalised by the results for the last row. The results are compared with the row correction factor by Mon [48], ESCOA [36] and Hofmann et al. [15] (Figure taken from Lindqvist et al. [36])

As can be seen in Figure (13), the simulation results by Lindqvist et al. [36] matches well with the row correction factor by Mon [48], showing a more or less constant heat transfer coefficient after four to five rows depending on the Reynolds number.

The row correction factor proposed by Hofmann et al. [15] shows, as mentioned, development all the way to the last row with a constant value not being reached for the heat transfer coefficient, as can be seen in Figure (13). This then leads to a significant underprediction for the first seven rows compared to the numerical results by Lindqvist et al. [36], as seen in Figure (13).

According to Holfeld [17], the studies by Jameson (1945) and Brauer (1961) shows the heat transfer coefficient for a staggered tube bundle to be constant from the fourth row onwards. The numerical results by Lindqvist et al. [36] shown in figure (13) are in good agreement with this.

The studies by Jameson (1945) and Brauer (1961) were used by Holfeld [17] for comparison with her own experimental results. The experimental results by Holfeld [17] did, however, not manage to reproduce these results. Investigating an eight-row staggered finned-tube bundle, the results by Holfeld [17] for the row-by-row heat transfer coefficient showed an oscillatory behaviour through the whole bundle. The first row had the lowest heat transfer coefficient in all the results by Holfeld [17], while the highest heat transfer coefficient varied from the second row, which is as expected, to the third, fourth and sixth row.

Trying to explain the unexpected oscillations in the results, Holfeld [17] pointed to errors in measurement equipment and uncertainty in measurements.

A comparison by Klynderud [69] of different results for the row-by-row heat transfer coefficient in the literature shows that for solid finned-tube bundles with eight rows, most of the change happens between the first and the fourth row.

In experiments done by Klynderud [69], this stabilisation around the fourth row was not present. Instead, the results by Klynderud [69] showed a similar oscillatory behaviour as in the results by Holfeld [17] described above. Many of the results by Klynderud [69] showed a peak in the heat transfer coefficient at the sixth row, although the maximum heat transfer coefficient was mostly found in the second row. It is worth pointing out that Klynderud [69] used the same experimental setup as Holfeld [17], meaning the same errors can be present in the measurements.

Investigating the row-by-row Colburn j-factor experimentally, Monheit [49] found around 95% of the change to happen up till the third row.

Lee et al. [32] also studied the development of the Colburn j-factor but did not find the same results as Monheit [49]. Lee et al. [32] studied experimentally a five-row finned-tube bundle with both a staggered layout and an in-line layout. For a staggered layout, the results by Lee et al. [32] did not show a constant heat transfer coefficient from the fourth to the fifth row. For this reason, no conclusion on how many rows before the heat transfer coefficient becomes constant was drawn by Lee et al. [32]. For an in-line layout, on the other hand, Lee et al. [32] found the row-by-row heat transfer coefficient to be constant after four rows.

As seen from the literature presented above, the number of rows before the row-by-row heat transfer coefficient becomes constant varies highly in the literature. In experimental studies, the influence of measuring techniques and measuring errors might play a role. There is also a possibility that geometry effects play an important role, meaning there is no universal number for how many rows before the heat transfer coefficient becomes constant [49]. For a finned-tube bundle with a staggered layout, most of the literature presented above shows the heat transfer coefficient to become constant between the fourth and sixth row, although the results vary from the third to the eighth row. In-line finned-tube bundles have been less studied, but both studies found investigating an in-line layout show the heat transfer coefficient to become constant at the fourth row.

Row-by-row results for the heat transfer coefficient collected from the experimental studies by Klynderud [69] and Holfeld [17], and from the numerical study by Lindqvist et al. [36] are used for comparison with the simulation results in this thesis. These are shown in Figure (31) in section 4.1. These results were chosen mostly due to the data from the studies being available, either through values given for the results or through clear graphs. These results are also for an eight-row finned-tube bundle which is the same as investigated in section 4.1.

2.4 Finned-tube and bundle layout effects

In this section, literature investigating the influences of fin tip clearance, fin pitch and tube bundle layout on the heat transfer and pressure drop, is presented.

In Figure (14) the geometrical dimensions of the finned-tubes and finned-tube bundles are defined.

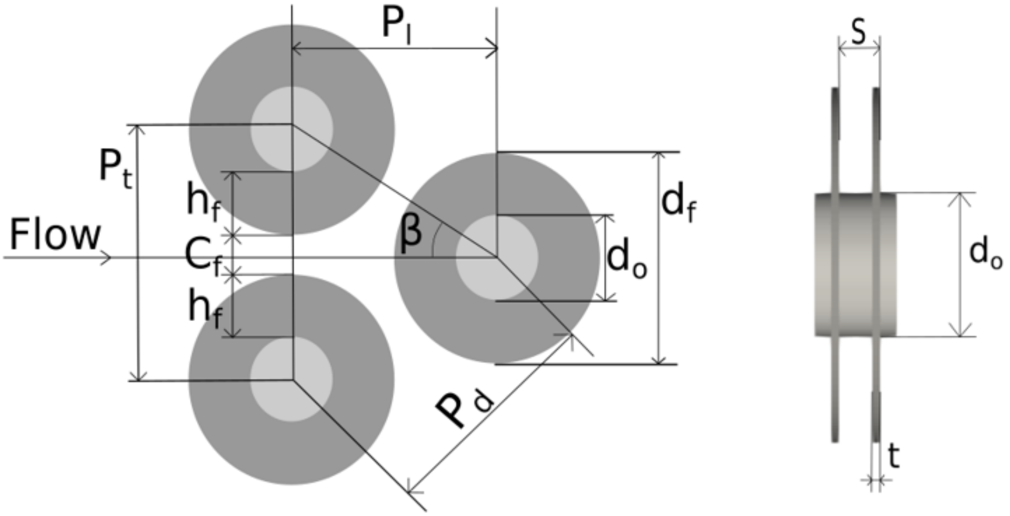

Figure 14: Definition of finned-tube and finned-tube bundle dimensions

P_l, P_t and P_d are the longitudinal, transverse and diagonal pitches, respectively. C_f is the fin tip clearance, S the fin pitch and t is the fin thickness. β is then defined as the tube bundle layout angle.

Fin tip clearance

In this section, literature regarding changing the fin tip clearance C_f (see Figure (14)), and how this influence the heat transfer coefficient and pressure drop, is presented. C_f is closely related to the longitudinal pitch (P_l) and transverse pitch (P_t) of the tube bundle. Some studies investigate the effects of changing either P_l or P_t on the heat transfer and pressure drop. This is the same as studying the tube bundle layout and is presented later. Changing the fin tip clearance here means changing C_f while keeping the ratio of P_l and P_t, and thus β, constant. All of the studies presented in this section studied finned-tube bundles with a staggered layout.

Holfeld [17] studied the effects of the fin tip clearance on the heat transfer coefficient and pressure drop experimentally. This study is the only one found studying the effect all the way to $C_f = 0$, that is to say, where the fins are touching. The study by Holfeld [17] compares three different fin tip clearances, $C_f = 0$, $C_f = 5$ mm and $C_f = 10$ mm, and is carried out using serrated finned-tube bundles with a $\beta = 30°$ layout. This corresponds to geometry 4, 5 and 6 in the study by Holfeld [17], all having a fin height $h_f = 18$ mm.

The results with different fin tip clearances by Holfeld [17] are shown in Figure (15).

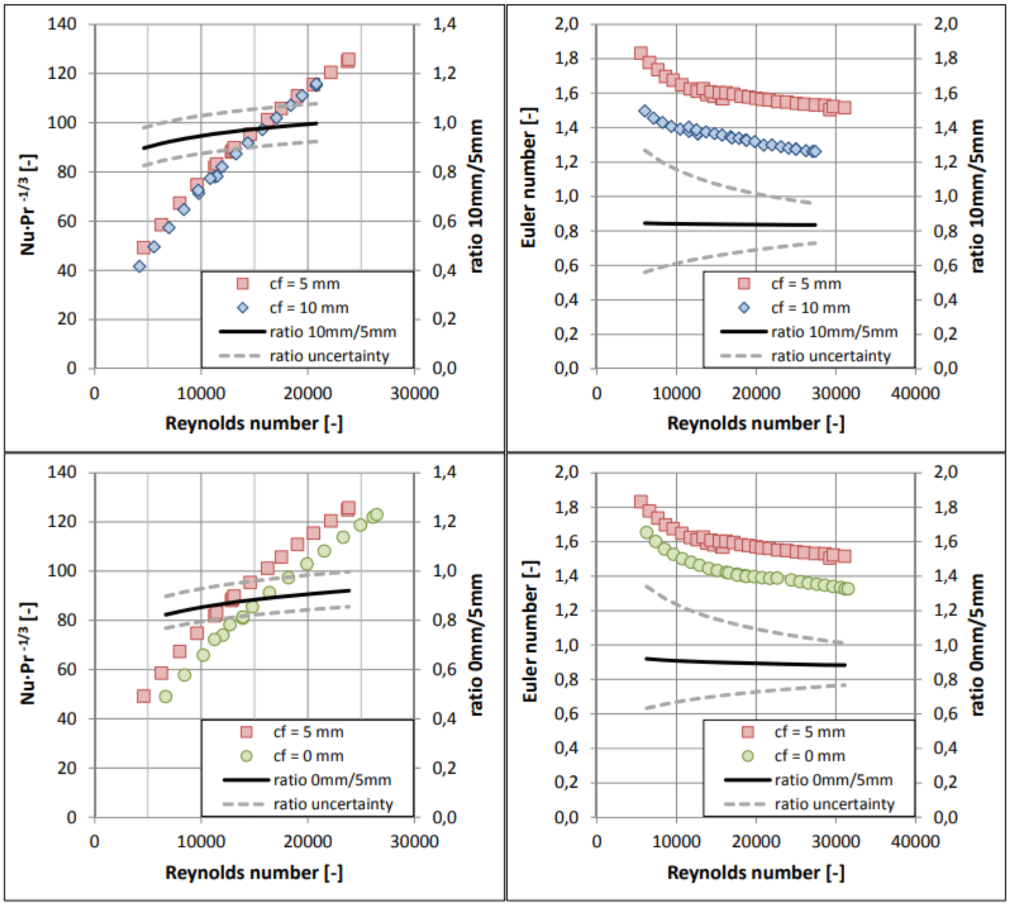

Figure 15: Results by Holfeld [17] showing the dependency of the fin tip clearances C_f on the heat transfer ($Nu \cdot Pr^{-1/3}$) and pressure drop (Eu) (Figure taken from Holfeld [17])

In figure (15), the heat transfer coefficient is given as $Nu \cdot Pr^{-1/3}$ and the pressure drop given as Eu. The middle fin tip clearance, $C_f = 5$ mm, is compared with both $C_f = 0$ (see bottom of Figure (15)) and $C_f = 10$ mm (see top of Figure (15)) by Holfeld [17]. A ratio of the two compared fin tip clearances is also given by Holfeld [17] to show the dependency on the Reynolds number, as seen in Figure (15).

As can be seen from Figure (15), changing the fin tip clearance from $C_f = 5$ mm down to $C_f = 0$ or up to $C_f = 10$ mm, both give a decrease in the heat transfer coefficient and the pressure drop.

Increasing the fin tip clearance from $C_f = 5$ mm to $C_f = 10$ mm gives a maximum decrease in Nu of 10% according to Holfeld [17]. As the Reynolds number increases the results approaches each other, as shown in the ratio to the top left in Figure (15) going towards unity. This decrease is explained by Holfeld [17], to be caused by more bypass flow as C_f increases.

Decreasing the fin tip clearance from $C_f = 5$ mm down to $C_f = 0$ also gives a decrease in Nu. The difference gets smaller as the Reynolds number increases, as seen in the ratio at the bottom left in Figure (15), going from around 18% down to 8% , according to Holfeld [17]. The decrease is, according to Holfeld [17], caused by the flow being less mixed when $C_f = 0$, acting more like a plate finned-tube and not an annular finned-tube heat exchanger.

A similar trend is seen in Figure (15) for the pressure drop. Decreasing the fin tip clearance from $C_f = 5$ mm down to $C_f = 0$ gives a decrease in Eu. This decrease becomes larger as the Reynolds number increases, going from 8% up to around 12%, according to Holfeld [17]. Increasing the fin tip clearance from $C_f = 5$ mm up to $C_f = 10$ mm also gives a decrease in Eu, now of around 15% [17].

The results by Holfeld [17] with different fin tip clearances given in Figure (15) are compared at the same Reynolds number. Changing C_f do, however, change the minimum flow area, A_{min}, between the finned-tubes. This means the mass flow rate at a given Reynolds number is different between the cases. Using the Reynolds number to evaluate the performance of the different fin tip clearances can therefore be misleading. For this reason, Holfeld [17] also compared the overall performance. As a performance parameter, Holfeld [17] used the heat transfer per unit of pressure drop. Using this performance parameter and comparing the fin tip clearances at the same mass flow rate, the results by Holfeld [17] showed the overall performance to reduce as C_f reduces.

The behaviour shown in the results by Holfeld [17], is, however, not universal. Ma et al. [40] studied experimentally the heat transfer and pressure drop for two different serrated finned-tube bundles, where the only difference was C_f. For the heat transfer, Ma et al. [40] found the opposite trend to Holfeld [17], that is to say, an increase in the heat transfer coefficient as C_f increases. It is, however, worth pointing out that the increase was relatively minor, and not something Ma et al. [40] commented on or described in any detail. The increase is not reflected in the Nu correlation (not shown) developed by Ma et al. [40] for serrated finned-tube bundles either. The correlation by Ma et al. [40] has a term $(P_t/P_l)^{0.06}$ indicating that Nu is independent of C_f. It is also worth pointing out that the two bundles used in the experiments by Ma et al. [40] had a fin tip clearance of $C_f = 33.9$ mm and $C_f = 49.9$ mm, which is much larger than the largest C_f tested by Holfeld [17].

For the pressure drop, Ma et al. [40] found Eu to reduce as C_f increases. That is to say, the same trend found by Holfeld [17]. The reduction in Eu as C_f increases also becomes larger as the Reynolds number increases, going from around 8% up to around 20%, according to Ma et al. [40].

Both Ackerman and Brunsvold [1] and Ward and Young [72] found negligible difference in the heat transfer coefficient when changing C_f [17]. Ackerman and Brunsvold [1] studied finned-tube bundles with elliptical pin-fins, while Ward and Young [72] studied solid annular finned-tubes. Both studied two different fin tip clearances, where the largest fin tip clearance was around 10 and 20 times bigger than the smallest, respectively [17]. For the pressure drop, Ackerman and Brunsvold [1] found a slight decrease as C_f increases. The decrease was, however, relatively small compared to Ma et al. [40] and Holfeld [17], as pointed out by Holfeld [17].

Mon [48] studied the effect of the fin tip clearance numerically, modelling three different geometries where the only difference was C_f. The fin tip clearances were $C_f = 6.8$ mm $C_f = 14.4$ mm and $C_f = 30.8$ mm. This corresponds to geometry s2, s13 and s14 in the study by Mon [48], all being solid annular finned-tubes in a bundle with a $\beta = 30°$ layout.

The results by Mon [48] showed a decrease in Nu as C_f increases. This decrease was larger going from $C_f = 14.4$ mm to $C_f = 30.8$ mm, than from $C_f = 6.8$ mm to $C_f = 14.4$ mm, being around 11% and 5% respectively [48]. The reason for the decrease, according to Mon [48], is that the finned-tubes in a bundle behaves more like individual finned-tubes as C_f increases. This is the same as having more bypass flow between the finned-tubes, which is the reason given by Holfeld [17] for a decrease in Nu going from $C_f = 5$ mm to $C_f = 10$ mm.

For the pressure drop, Mon [48] found the same results as all of the other studies above, where an increase in C_f gives a decrease in Eu.

Fin pitch

In this section literature regarding change in the fin pitch is presented. The fin pitch (S), is the distance from the centre of one fin to the next, as seen in Figure (14). The fin density is then defined as one over the fin pitch ($1/S$). All of the studies presented in this section studied finned-tube bundles with a staggered layout.

Holfeld [17] studied experimentally two finned-tube bundles where the only difference was the fin pitch. The fin pitches studied were $S = 1/270 = 3.70$ mm and $S = 1/170 = 5.88$ mm. This corresponds to geometry 2 and 3 in the study by Holfeld [17]. These geometries are both annular finned-tubes with a fin height of $h_f = 18$ mm.

The results by Holfeld [17] for the two different fin pitches are shown in Figure (16).

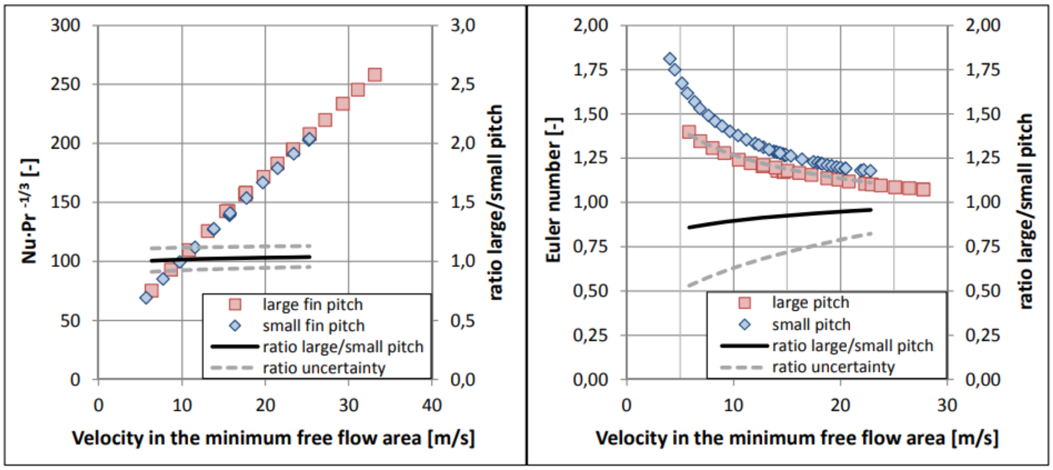

Figure 16: Results by Holfeld [17] showing the dependency of the fin pitch S on the heat transfer ($Nu{\cdot}Pr^{-1/3}$) and pressure drop (Eu) at different U_{Amin}. (Figure taken from Holfeld [17])

As seen in Figure (16), the results by Holfeld [17] show a close to negligible difference in the heat transfer coefficient at the same U_{Amin}. The larger fin pitch has a slightly higher Nu going from around 1% up to around 4% as the velocity increases, according to Holfeld [17]. This is well within the uncertainty of around ±12% in measurements of Nu calculated by Holfeld [17]. Even though the increase in Nu as the fin pitch increases is close to negligible, the correlation for Nu developed by Holfeld [17] (see equation (20) in section 2.5) shows an increase in Nu as S increases. The correlation by Holfeld [17] and its dependency on S is shown in Figure (17) alongside the numerical results by Lindqvist et al. [36].

As pointed out by Holfeld [17], comparing Nu at the same mass flow rate gives a totally different answer. Here Nu for the smaller fin pitch is much higher. As the minimum free-flow area is smaller for the smaller fin pitch, the Reynolds number is higher than for the larger fin pitch at the same mass flow rate.

For the pressure drop at the same U_{Amin}, Holfeld [17] found Eu to increase as the fin pitch decreases, as seen in Figure (16). As the velocity increases, the difference gets smaller, where the smallest fin pitch, according to Holfeld [17], goes from having around 18% higher Eu down to 8% higher Eu, as seen in Figure (16).

The reason for a smaller pressure drop for the larger fin pitch is, according to Holfeld [17], the decrease in surface area. This results in less friction and thus lower pressure drop.

Comparing the overall performance of the different fin pitches at the same mass flow rate, Holfeld [17] found that heat transfer per unit pressure drop and per unit weight has no dependency on the fin pitch. If compared per unit volume, Holfeld [17] found the performance to increase as the fin pitch decreases.

Næss [52] also studied the effect of the fin pitch on Eu and Nu in staggered finned-tube bundles with serrated fins and found a similar result to Holfeld [17]. Changing the fin pitch from $S = 5.08$ mm to $S = 3.63$ mm gave a decrease in the heat transfer coefficient of around 6% in the results by Næss [52]. The finned-tubes in both the bundles investigated by Næss [52] had a fin height $h_f = 9.52$ mm. This corresponds to geometry 6 and 10 in the study by Næss [52].

For the pressure drop, Næss [52] found that decreasing the fin pitch from $S = 5.08$ mm to $S = 3.63$ mm, increased Eu by around 30%.

Testing four different staggered finned-tube bundles where the only difference was the fin pitch, Ma et al. [40] found the same trend as Næss [52] and Holfeld [17]. The fin pitch in the study by Ma et al. [40] ranged from $S = 4.15$ mm down to $S = 3.89$ mm and yielded around a 5% decrease in the heat transfer coefficient, according to Ma et al. [40]. This decrease was only present at lower Reynolds numbers, with results at higher Reynolds numbers showing very little difference. The finned-tube bundles studied by Ma et al. [40] all had serrated fins and a fin height of $h_f = 16$ mm. These results were, according to Ma et al. [40], consistent with previous results they had for solid finned-tube bundles.

For the pressure drop, Ma et al. [40] found an increase as the fin pitch decreased. The increase in Eu was larger at higher Reynolds numbers, yielding around an 8% increase in Eu going from $S = 4.15$ mm to $S = 3.89$ mm, according to Ma et al. [40].

FaJiang et al. [8] studied annular finned-tube bundles with different fin pitches experimentally and found the same trend as in the studies above. That is to say, an increase in the heat transfer coefficient as the fin pitch increases. The finned-tubes they studied had a fin height $h_f = 13$ mm and the fin pitch was varied from $S = 7$ mm up to $S = 16$ mm. The increase in Nu as the fin pitch increases, was, however, only true up to a point. The two largest fin pitches, $S = 13$ mm and $S = 16$ mm, tested by FaJiang et al. [8] gave very similar results.

For the pressure drop, FaJiang et al.[8] found that a decrease in the fin pitch increases Eu, that is to say, the same trend as in all of the other studies above.

Pongsoi et al. [59] studied three annular finned-tube bundles, with fin pitches $S = 2.4$ mm, $S = 3.2$ mm and $S = 4.2$ mm. The bundles they studied were, however, quite shallow, having only two rows. From their results, Pongsoi et al. [59] concluded that the heat transfer coefficient is more or less independent of the fin pitch.

It is worth pointing out that all the experimental studies described above show very small changes in the heat transfer coefficient when changing the fin pitch. If the ±12% uncertainty in measurement of Nu calculated by Holfeld [17] is assumed to hold for all the studies, these changes are negligible.

Lindqvist et al. [36] investigated fin pitch numerically at $Re_{d_o} = 5000$. The finned-tube bundle geometries Lindqvist et al. [36] modelled used the same starting point as the geometry modelled in this thesis and shown in Figure (28).

The results for the heat transfer (as $Nu \cdot Pr^{-1/3}$) and pressure drop (as Eu) by Lindqvist et al. [36] are shown in Figure (17). The results are compared with the Nu and Eu correlations by Holfeld [17] (see equations (20) and (23) in section 2.5) and from ESCOA [36].

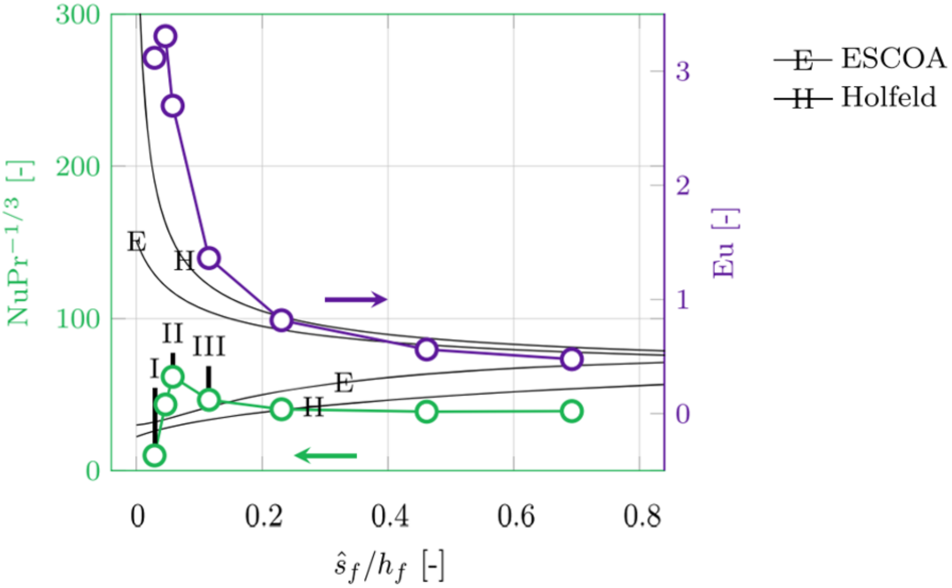

Figure 17: Results by Lindqvist et al. [36] for the heat transfer coefficient ($Nu \cdot Pr^{-1/3}$) and the pressure drop (Eu) at different fin pitches along with the correlations by Holfeld and from ESCOA. The variable $\hat{s_f}/h_f$ corresponds to the ratio of the fin pitch minus the fin thickness ($S-t$) to the fin height h_f (The figure is adapted from a figure by Lindqvist et al. [36])

As shown in Figure (17), the pressure drop increases as the fin density increases showing a nearly exponential growth as the fin pitch goes to zero. This is also visible in the correlation by Holfeld, and, to a degree, in the correlation from ESCOA.

The heat transfer also increases as the fin pitch decreases, but only up to a point, before it drops off, as seen in Figure (17). The roman numerals (I, II and III) in Figure (17) corresponds to a figure in the study by Lindqvist et al. [36] showing the streamlines for these three fin pitches. As explained by Lindqvist et al. [36], as the fin pitch goes to zero, the bypass flow increases. The flow then goes from a relatively uniform flow over the fins to mostly flow around the fins.

Both the correlations show a decrease as the fin pitch increases and fail to predict the increase and sudden decrease shown in the numerical results by Lindqvist et al. [36], shown in Figure (17).

It is worth pointing out that Lindqvist et al. [36] found the heat transfer per unit volume of heat exchanger to increase faster than the pressure drop, up to a point. That is to say, if heat exchanger volume is of high priority, a small fin pitch can be used. This is similar to the result found by Holfeld [17].

Mon [48] also studied the effect of fin pitch numerically modelling four-row annular finned-tube bundles with a staggered layout. Mon [48] studied the effect of fin pitch at two different fin heights, $h_f = 5$ mm with $S = 2.5$ mm, 2.1 mm and 4.5 mm and $h_f = 10$ mm with $S = 1.2$ mm and 2.6mm. This corresponds to geometries s2, s6 and s7 for $h_f = 5$ mm, and s4 and s8 for $h_f = 10$ mm in the study by Mon [48].

The results by Mon [48] for the shorter fins ($h_f = 5$ mm), show a slight increase in the heat transfer coefficient as the fin pitch gets smaller.

For the taller fins ($h_f = 10$ mm), the results by Mon [48] show the opposite trend. Here the heat transfer coefficient increases as the fin pitch increases. The increase was, according to Mon [48], more pronounced at lower Reynolds numbers.

Mon [48] explained this to be down to boundary layer development over the fins, as described in section

2.2 and shown in Figure (3). According to Mon [48], as long as the fin pitch is large enough for the boundary layers between two adjacent fins to grow separately there is little influence on the heat transfer coefficient. If the fin pitch is below this point and the boundary layers touch, the heat transfer coefficient increases as the fin pitch increases [48].

For the pressure drop, Mon [48] found the same trend as all the other studies presented above, where the pressure drop decreases as the fin pitch increases.

Tube bundle layout

In this section literature regarding the layout of the finned-tube bundle is presented.

The angle β was by Holfeld [17] called the "tube layout angle", and is defined as $\beta = \arctan(\frac{P_t/2}{P_l})$. The angle and the transverse and longitudinal pitch are shown in Figure (14). The angle β is used to describe the different layouts.

Several sources only differentiate between an in-line and a staggered layout, where an inline corresponds to $\beta = 90°$. Increasing the angle β towards $90°$, one expects the staggered layout to behave more and more like a finned-tube bundle with an in-line layout [17]. A schematic representation of the flow in both an in-line and a staggered finned-tube bundle is shown in section 2.2 in Figures (9) and (6) respectively.

There seems to be a consensus in the literature that a finned-tube bundle with a staggered layout has a higher heat transfer coefficient than a comparable bundle with an in-line layout [48]. This is caused by the difference in the distribution of the heat transfer coefficient between the two layouts, as described in section 2.2. For the in-line layout more of the flow bypasses the fins, flowing in the open area between the finned-tubes. This causes a less mixed flow [17]. Due to the way the finned-tubes in an in-line layout are situated straight behind each other, the wake region behind the tubes influences both the leading and trailing edge of the fins, as described in section 2.2.

How much higher the heat transfer coefficient is for a staggered layout compared with an in-line layout depends on different geometry parameters. For a deep finned-tube bundle with high fins, Brauer (1964) found, according to Mon [48], a 100% increase. For a shallow, two-row, finned-tube bundle with high fins, Kearney and Jacobi [26], found the heat transfer coefficients to be of the same order of magnitude, as described in section 2.2.

Both of these findings were observed by Rabas et al. [60]. For a shallow finned-tube bundle at higher Reynolds numbers, Rabas et al. [60] found that the heat transfer coefficient of an in-line layout approaches that of a staggered layout. Rabas et al. [60] also found that this was dependent on the fin tip clearance, where the in-line layout performed better for a smaller C_f. For deeper bundles Rabas et al. [60] found the staggered layout to have a significantly higher heat transfer coefficient compared to a finned-tube bundle with an in-line layout.

Due to the bypass flow associated with an in-line layout, the pressure drop is also lower than for a finned-tube bundle with a staggered layout [17].

Næss [52] studied experimentally serrated finned-tube bundles with a staggered layout. The tube layout angle ranged from $\beta = 30°$ all the way up to $\beta = 60°$. It should be mentioned that the Reynolds number is calculated in the smallest free-flow area, A_{min}, and that this changes from the transverse to the diagonal plane as β increases. Næss [52] studied the effect of the layout at two different tube diameters but using the same fin height for both.

The relative results by Næss [52] for the heat transfer coefficient is shown in Figure (18). The results at different β are shown relative to the results for a $\beta = 30°$ layout. The results are also compared with some correlations and the experimental results by Ackerman and Brunsvold [1], as seen in Figure (18) . Instead of using β as a parameter, the ratio of the area in the transverse and diagonal plane is used by Næss [52] (S_t/S_d in Figure (18) corresponding to A_{P_t}/A_{P_l} in this thesis). This parameter is not directly proportional to β, being dependent on the geometry of the finned-tubes, but an increase for the same finned-tubes corresponds to an increase in β.

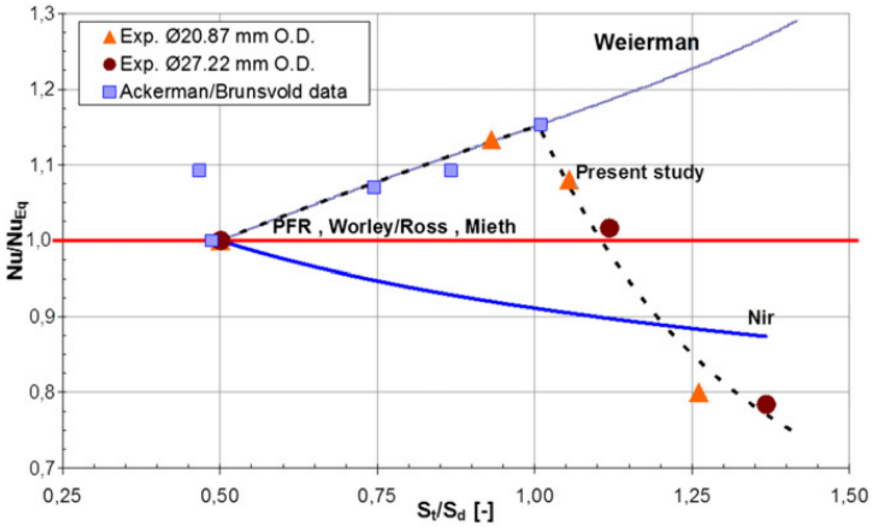

Figure 18: Results by Næss [52] for the relative Nu at different β compared to a $\beta = 30°$ layout (called Nu_{eq} in the figure) at two different outside tube diameter (O.D.). The results are compared with some correlations and experimental results by Ackerman and Brunsvold [1]. S_t/S_d is the ratio of the area in the transverse and diagonal plane, and an increase in the ratio corresponds to an increase in β. (Figure taken from Næss [52])

As can be seen in Figure (18), the heat transfer coefficient increases around 15% as the area ratio goes from 0.5 towards 1.0. This corresponds to an increase in the tube layout angle from $\beta = 30°$ up to around $\beta = 45°$.

As the area ratio increases above 1.0, or around $\beta = 45°$, the heat transfer coefficient decreases quite rapidly, as can be seen in Figure (18). At $\beta = 60°$, corresponding to the area ratios being around 1.27 and 1.42 in the results by Næss [52], shows the heat transfer coefficient to be around 80% of the heat transfer coefficient at $\beta = 30°$, as can be seen in Figure (18).

Næss [52] also tested bundles with a tube layout angle of $\beta = 50°$ (corresponding to the area ratios being 1.05 and 1.15). At this angle, the heat transfer coefficient is a little higher than the heat transfer coefficient at $\beta = 30°$, as seen in Figure (18).

From this data, Næss [52] proposed a correction for the tube bundle layout based on the Nusselt number for an equilateral ($\beta = 30°$) layout. The correction is valid for $\frac{A_{P_t}}{A_{P_d}} > 1$.

$$\frac{Nu}{Nu_{\beta=30^\circ}} = 0.6 + 14.3 \cdot e^{-3.23\cdot\frac{A_{P_t}}{A_{P_d}}} \tag{12}$$

where A_{P_t} and A_{P_d} is the area in the traverse and diagonal plane.

The asymptotic Nusselt number ratio of 0.6 in the correction by Næss [52] in equation (12) is taken from the in-line results by PFR (1976) [52]. This should therefore be a representative value for an in-line layout, although this was not tested by Næss [52].

For $\frac{A_{P_t}}{A_{P_d}} < 1$, Næss [52] found the results to match well with the correlation by Weierman [73], as seen in Figure (18). According to Næss [52], this corresponds to a growth of $Nu \sim (\frac{P_t}{d_o+2\cdot t})^{0.35}$.

This growth is not found in the other correlations Næss [52] used for comparison. As seen in Figure (18), the correlation by Nir [54] shows a decrease in the heat transfer coefficient as β increases, while the others show no dependency on β.

For the pressure drop, Næss [52] found no change in Eu increasing β from 30° up to 50°, but quite a substantial drop down to around 55% of the $\beta = 30°$ layout for the $\beta = 60°$ layout.

A correction for the pressure drop behaviour was also proposed by Næss [52]:

$$\frac{Eu}{Eu_{\beta=30^\circ}} = min\left(1.0\ ;\ 0.52 + 964.5 \cdot e^{-3.24 \cdot \frac{P_t}{P_l}}\right) \tag{13}$$

Here P_t and P_l are the transverse and longitudinal pitch, used instead of the area ratio to represent the layout.

The results by Ackerman and Brunsvold [1] are also shown in Figure (18) alongside the results by Næss [52]. These results also follow a similar trend as β increases, matching fairly well with the correlation by Weierman [73], as seen in Figure (18). Ackerman and Brunsvold [1] studied finned-tube bundles with elliptical pin-fins where the staggered tube layout angle ranged from $\beta = 29°$ up to $\beta = 42.7°$. This corresponds to an area ratio of around 0.5 up to 1.0 in Figure (18). Ackerman and Brunsvold [1] also tested a finned-tube bundle with an in-line, $\beta = 90°$, layout (not shown in Figure (18)) having the same transverse and longitudinal pitch as the finned-tube bundle they tested with a $\beta = 29°$ layout.

Ackerman and Brunsvold [1] correlated their results for the individual bundles, all having a correlation: $Nu = a \cdot Re^{0.547} \cdot Pr^{1/3}$, where a is a constant changing between the different bundles. Comparing the constant for the in-line layout and the comparable finned-tube bundle with a staggered layout shows a 21% higher heat transfer coefficient for the staggered layout. This corresponds to a ratio of 0.82 for the heat transfer coefficient of the in-line layout to the $\beta \approx 30°$ layout. This is substantially higher than the asymptotic value of 0.6 indicated by Næss [52] in the tube bundle layout correction in equation (12). For the pressure drop, Ackerman and Brunsvold [1] found the in-line layout to have around 55% of the pressure drop of the comparable finned-tube bundle with a staggered layout at low Reynolds number, with the difference decreasing to around 70% with increasing Reynolds numbers.

The studies by Næss [52] and Ackerman and Brunsvold [1] are the only ones found studying the tube bundle layout at such a wide range of the angle β. Some other studies have been found investigating how the heat transfer and pressure drop changes when P_l and P_t are changed separately. Both of these changes will change β, but usually not to the extent done in the studies by Næss [52] and Ackerman and Brunsvold [1].

Two such studies were conducted by Ma et al. [40] and by FaJiang et al. [8]. Both studies used pitches corresponding to a tube bundle layout ranging from $\beta \approx 21°$ up to $\beta \approx 33°$.

Another such study was, according to Holfeld [17], conducted by Worley and Ross (1960). These studies are, however, not that relevant for the investigation of layouts due to their small variation in β.

Several studies only differentiate between a finned-tube bundle with an in-line layout and a staggered layout. An in-line layout is expected to have a lower heat transfer coefficient than a comparable finned-tube bundle with a staggered layout [48]. How much lower varies between different studies. This is, as pointed out by Rabas et al. [60], also dependent on the finned-tube and bundle geometry. As described above, the results by Ackerman and Brunsvold [1] shows the ratio of the in-line layout to the $\beta = 30°$ layout to be around 0.82 for Nu, while, according to Næss [52], this value should be around 0.60.

According to Næss [52], Weierman et al. [75] found an in-line layout to have a heat transfer coefficient 75% lower than a $\beta = 30°$ layout. This is believed to be a misprint. The results by Weierman et al. [75] showed a staggered finned-tube bundle with seven rows to have the same pressure drop and heat transfer as an in-line bundle with four rows. This gives a ratio of the in-line layout to the staggered layout of $4/7 \approx 57\%$ or a decrease of 43%.

Lee et al. [32] studied experimentally the difference in the heat transfer coefficient between a staggered and an inline layout using five-row annular finned-tube bundles. These experiments were done at a Reynolds number much lower than the studies mentioned above. According to Lee et al. [32] their results showed the heat transfer coefficient for a staggered layout to be on average 16.2% higher than for an in-line layout. This difference was larger for a shallow bundle with only two rows [32]. This is the opposite of what Kearney and Jacobi [26] and Rabas et al. [60] found for higher Reynolds numbers.

Mon [48] studied the difference between a staggered $\beta = 30°$ layout and an in-line layout numerically.

The results by Mon [48] shows that a staggered layout has higher heat transfer, but also higher pressure drop. At Re_{do}=8600 and $h_f = 5$ mm Nu is, according to Mon [48], 41.7% higher for the staggered layout compared to a comparable finned-tube bundle with an in-line layout, while the pressure drop is 66.5% higher.

Mon [48] also used a performance parameter that takes both the heat transfer and pressure drop into account. The parameter used is the ratio of the heat transfer rate to the pumping losses, where the pumping losses are the pressure drop multiplied by the volumetric flow rate [48].

Using this performance parameter, the in-line layout has, according to Mon [48], an advantage at lower Reynolds numbers. This is because the pressure drop disadvantage of the staggered layout is larger than the advantage in the heat transfer coefficient. This makes the overall performance better for an in-line layout at lower Reynolds numbers, according to Mon [48].

The results by Mon [48], show that as the Reynolds number increases, the pressure drop for an in-line layout increases faster than the heat transfer coefficient. This then lowers its performance advantage.

2.5 Heat transfer and pressure drop correlations

In this section, heat transfer and pressure drop correlations for a row of finned-tubes and for finned-tube bundles are presented. All the correlations are for solid annular finned-tubes and only correlations that are used are presented.

Holfeld [17] compared some of the correlations with her own results and a database of experimental results. The error band for where 95% of the data are predicted by the correlations was also given by Holfeld [17]. This is the error band that will be used for the correlations.

Heat transfer correlations

The heat transfer coefficient is usually given on dimensionless form as the Nusselt number (Nu), however, some (mostly American) studies used the Colburn j-factor (j). The relationship between them is:

$$j = \frac{Nu}{Re_{d_o} \cdot Pr^{1/3}} \tag{14}$$

Many correlations for the heat transfer coefficient has been proposed. Correlations have a tendency to be based on a limited amount of data usually from experiments conducted by the same author proposing the correlation. However, correlations stemming from meta-studies with data from various studies do exist [17].

One-row heat transfer correlations

Most correlations are for a bundle of finned-tubes. These correlations would overpredict the heat transfer coefficient of a single row of finned-tubes. A few correlations for one row of finned-tubes have been proposed. However, using row correction factors, as described in section 2.3, and extending the validity of full bundle correlations are also common practice.

Huisseune et al. [19] proposed a correlation for one row of solid finned-tubes. The correlation is developed from experimental results by Huisseune et al. [19], and takes the form:

$$Nu = 0.495 \cdot Re_{d_o}^{0.509} \left(\frac{P_t}{d_o}\right)^{-0.209} \tag{15}$$

The correlation is valid for $1000 < Re_{d_o} < 14100$, and, according to Huisseune et al. [19], predicts 95% of the experimental data within ±11%.

Nir [54] proposed a correlation for a finned-tube bundle based on experimental data from various studies. To extend the validity of the correlation, Nir [54] used the row correction factor by Weierman [73].

Many versions of this correlation were given by Nir [54] using different definitions of the Reynolds number. The version given in equation (16) is taken from Holfeld [17]. Holfeld [17] compared this version of the correlation by Nir [54] with the database and specified the error band for the 95% confidence interval of the data. This version of the correlation by Nir [54] takes the form:

$$Nu = 1.0 \cdot Re_{d_o}^{0.6} \cdot Pr^{1/3} \left(\frac{A_{tot}}{A_{min}}\right)^{-0.266} \left(\frac{d_f}{d_o}\right)^{-0.4} \cdot K_h \tag{16}$$

where A_{tot} is the total heat transfer area and A_{min} is the minimum free-flow area. The diameters d_f and d_o are for the fin and the outside of the tube, respectively. K_h is the correction factor by Weierman [73] used to extend the validity of the correlation. For one row $K_h \approx 0.70$ [73]. The validity range , $300 < Re_{dh} < 10000$, for the correlation by Nir [54] is given using the Reynolds number with a hydraulic diameter as the length scale. Nir [54] defined the hydraulic diameter for solid fins as:

$$d_h = \frac{4 \cdot d_f}{\frac{A_{tot}}{A_{min}}} \tag{17}$$

For a full finned-tube bundle, Holfeld [17] found the correlation by Nir [54] to predict 95% of the experimental data within a ±39% error band. It is worth pointing out that Nir [54] specified ±10% error band for the correlation for the 95% confidence interval.

Moore et al. [50] compared the two correlations in equations (15) and (16) with their own experimental data. The findings by Moore et al. [50] showed the correlation by Huisseune et al. [19] to match the experimental data best. Even so, the correlation by Huisseune et al. [19] underpredicted the experimental data by Moore et al. [50] up to a Reynolds number $Re_{do} \approx 12000$. The correlation by Huisseune et al. [19] was, however, inside the interval of measurement error given by Moore et al. [50] for their experimental data.

The correlation by Nir [54] was below the correlation by Huisseune et al. [19], and thus showed a greater underprediction of the experimental data by Moore et al. [50] than the correlation by Huisseune et al. [19].

Full bundle heat transfer correlations

PFR (1976) proposed a relatively simple correlation for a finned-tube bundle with solid fins, based on experimental data from various studies. The correlation is collected from Holfeld [17] and takes the form:

$$Nu = 0.29 \cdot Re_{d_o}^{0.633} \cdot Pr^{1/3} \cdot Ar^{-0.17} \tag{18}$$

The correlation is, according to Holfeld [17], valid for $1\ 000 < Re_{d_o} < 40\ 000$. The parameter Ar is the overall extended-surface-area ratio, which is the ratio of the total heat transfer area to the heat transfer area of the tubes without fins [17]. Defined per fin pitch, this becomes $Ar = \frac{A_t}{\pi \cdot d_o \cdot S}$.

Holfeld [17] also compared this correlation with the database. In the comparison by Holfeld [17], the correlation by PFR (1976) predicted 95% of the data within ±31%.

A similar correlation exists in the VDI heat atlas (2010). This correlation is also developed from experimental data from various studies. The correlation from VDI (2010) is, again, collected from Holfeld [17] and takes the form:

$$Nu = 0.38 \cdot Re_{d_o}^{0.6} \cdot Pr^{1/3} \cdot Ar^{-0.15} \tag{19}$$

The correlation from VDI (2010) is valid for $1\ 000 < Re_{d_o} < 100\ 000$ [17].

Mon [48] did a comparison of the VDI (2010) correlation with results from various experimental studies. Mon [48] found the correlation from VDI (2010) to predict 90% of the data within ±38%. Mon [48] did not specify the 95% confidence interval.

It is worth pointing out that this is higher than the maximum deviation specified from VDI (2010), which, according to Mon [48], is ±25%.

A correlation for solid finned-tube bundles was proposed by Holfeld [17]. This correlation was based on both the experimental results by Holfeld [17] and the databases of experimental results from various studies. The correlation by Holfeld [17] takes the form:

$$Nu = 0.346 \cdot Re_{do}^{0.751} \cdot Ar^{-0.350} \cdot \left(\frac{P_t}{d_o}\right)^{-0.575} \cdot \left(\frac{h_f}{d_o}\right)^{0.464} \cdot Pr^{1/3} \tag{20}$$

The correlation predicts 95% of the data from the database and experiments by Holfeld [17] within ±26%. No Re_{do} validity range was given by Holfeld [17] for this correlation.

The VDI (2010) and PFR (1976) correlations in equations (19) and (18), both taken from Holfeld [17], were chosen since both are based on data from various studies, and not just from one. Both of them are also valid at $Re_{do} = 1100$, which is the lowest Reynolds number full bundle simulation performed in this thesis. The correlation by Holfeld [17], shown in equation (20), is used in the comparison of different fin pitches in section 4.2.

The comparison by Holfeld [17] of some correlations against the database of experimental data shows the correlation by PFR (1976) to be the second most accurate after the correlation by Holfeld [17].

Pressure drop correlations

The pressure drop is usually given on a dimensionless form as the Euler number (Eu).

One-row pressure drop correlations

Very few one-row correlations for Eu have been found.

Nir [54] proposed a pressure drop correlation based on experimental data from various studies. This correlation was developed for a full bundle of finned-tubes, but is, according to Nir [54], valid also for one row of finned-tubes.

In the same way as with the Nu correlation by Nir [54] (shown in equation (16)), many versions of the Eu correlation were given by Nir [54] using different definitions of the Reynolds number. The version given here is taken from Holfeld [17], along with the specified error band for predicting 95% of the database given by Holfeld [17]. The correlation by Nir [54] then takes the form:

$$Eu = 2.12 \cdot Re^{-0.25} \cdot \left(\frac{A_{tot}}{A_{min}}\right)^{0.45} \left(\frac{d_f}{d_o}\right)^{-0.25} \tag{21}$$

The correlation is valid for $300 < Re_{dh} < 10^4$. In the comparison with experimental data by Holfeld [17], the correlation by Nir [54] predicted 95% of the data within ±32%. This comparison was done using experimental results for a full bundle.

Full bundle pressure drop

Ward and Young [72] proposed a correlation for the pressure drop based on their own experimental data. The version of the correlation presented here is taken from Mon [48], and takes the form:

$$Eu = 0.256 \cdot Re_{do}^{-0.264} \cdot \left(\frac{t}{d_f}\right)^{-0.377} \cdot \left(\frac{S}{d_o}\right)^{-0.396} \cdot \left(\frac{P_l}{d_o}\right) \tag{22}$$

This correlation is valid from $1000 < Re_{do} < 28\,000$.

Ward and Young [72] stated an average deviation from the experimental data of ±15% and a maximum deviation of $+26\%/-31\%$ for the correlation shown in equation (22).

This fits relatively well with a comparison by Mon [48] where the correlation by Ward and Young [72] shown in equation (22) was compared with numerical results by Mon [48]. In this comparison, most of the numerical results by Mon [48] were within a $+30\%/-20\%$ deviation from the correlation by Ward and Young [72]. The maximum deviation given by Ward and Young, [72] therefore, seems reasonable.

Holfeld [17] also proposed a correlation for Eu based on both experimental results by Holfeld [17] and the database of experimental result. This takes the form:

$$Eu = 0.340 \cdot Re_{d_o}^{-0.132} \cdot \left(\frac{P_t}{P_l}\right)^{0.502} \left(\frac{A_{tot}}{A_{min}}\right)^{0.738} \left(\frac{h_f}{d_o}\right)^{-0.293} \left(\frac{S}{d_o}\right)^{0.333} \tag{23}$$

The correlation predicts 95% of the data in the database within ±34% according to Holfeld [17].

PFR (1976) also proposed a correlation for the pressure drop [17]. In the comparison with the database, Holfeld [17] did, however, find the correlation by PFR (1976) to predict 95% of the data within a ±121% deviation. Due to the large error band, this correlation is not used.

3 Method - extending the one-row model

In this section, the updated one-row model is first presented. This is an updated version of the model developed in the project thesis [65]. The updated one-row model was used to investigate the grid dependency and the usage of wall functions. An investigation of suitable turbulence models was also performed using this model.

The results of these investigations are presented and discussed in this section. These results are then used in the extension of the one-row model into a multi-row, full bundle model. The differences between the one-row model and the full bundle model are also presented in this section, along with an attempt to develop a reduced domain model. The methodology for calculating or postprocessing the simulation results is presented at the end of this section.

3.1 The updated one-row model

In this section the one-row model is described.

Governing equations

Doing simulations and modelling flow over finned-tubes involves conjugate heat transfer (CHT) between the fluid gas region and the solid finned-tube regions. CHT problems requires solving the full Navier-Stokes equations for the fluid region and the energy equation for both the fluid and solid regions [51].

As described in section 2.1, the Reynolds averaged version of the Navier-Stokes equations (RANS) are solved to account for turbulence.

The variables are decomposed using the Reynolds decomposition. Here the parameters are set to a mean and a fluctuation around this mean. For the x-component of the velocity, this looks like $\widetilde{u} = U + u$, where U is the mean of $\widetilde{u}$ and u is the fluctuation of $\widetilde{u}$ around U. These decomposed variables are then inserted into the Navier-Stokes equations, before the equations are averaged. This makes the RANS equations. The RANS equations constitutes equations for the average of the flow [68].

The flow is assumed to be incompressible, and the governing equations for the momentum then takes the form as the incompressible RANS equations. The RANS equation for the i^{th} directions is collected from Mon [48] and Tannehill et al. [58] and takes the form:

$$\frac{D\rho U_i}{Dt} = -\frac{\partial p}{\partial x_j} + \frac{\partial}{\partial x_j}\left(\mu\left(\frac{\partial U_i}{\partial x_i} + \frac{\partial U_j}{\partial x_j}\right) - \rho\overline{u_i u_j}\right) + S_U \tag{24}$$

where S_U is a source term and μ is the dynamic viscosity. The Einstein summation notation (e.g. see White [76]) is used to represent vectors and $\frac{D}{Dt}$ is the material derivative, which is defined as: $\frac{D}{Dt} = \frac{\partial}{\partial t} + U_j \frac{\partial}{\partial x_j}$ [51].

The term: $-\overline{u_i u_j}$ is the additional term in the RANS equations coming from the mathematical process of averaging. This then needs to be modelled using a turbulence model to have closure of the equations, as described in section 2.1.

The Reynolds averaged energy equation is obtained analogous to the RANS equations. The Reynolds decomposed variables are inserted into the equations and then the equation is averaged [68].

The Reynolds average energy equation on the total energy (E) form, then takes the form:

$$\frac{D\rho E}{Dt} + \frac{\partial U_i p}{\partial x_i} = \frac{\partial}{\partial x_i}\left(\kappa\frac{\partial T}{\partial x_i} - \rho \cdot C_p \cdot \overline{tu_i}\right) + S_E \tag{25}$$

Where S_E is a source term, which includes the effect of gravity on the flow. It can also include the effect of radiation, this is neglected. κ is the thermal conductivity and comes from utilising Fourier's law to describe the heat flux. The energy equation is taken from Mon [48] and Tannehill et al. [58].

For the fluid region, OpenFOAM solves the total energy equation decomposed into $E = \widetilde{h} + K - p/\rho$. Where $\widetilde{h}$ is the enthalpy, $K = \sum_i |U_i|^2/2$ is the specific kinetic energy and p/ρ is the pressure divided by the density [56].

The term $\overline{tu_i}$ is also an additional term coming from the averaging. This also needs to be modelled to have closure of the equation. As described in section 2.1, the assumption of a turbulent viscosity and a turbulent diffusivity is used. These are then coupled by the Reynolds analogy using a turbulent Prandtl number (Pr_t) [68]. $Pr_t = 0.85$ is used in this thesis.

The same energy equation is solved for the solid regions, but with all terms involving the velocity set to zero. The equation is solved on internal energy (e) form. Where $E = e + K = e$ for the solid regions [56].

The continuity equation is also used in the solution procedure and takes the form $\frac{\partial U_i}{\partial x_i} = 0$.

It is worth pointing out that the governing equations are, technically, solved on integrated form since OpenFOAM uses the finite volume method (FVM), not the derivative form given here.

Pressure-velocity algorithm

An algorithm or pressure-velocity coupling is needed in order to solve the RANS equations numerically since no explicit equation is given for the pressure [10]. A pressure-velocity coupling uses the restriction the continuity equation sets for the velocity field. In the algorithm, the RANS equations (see equation (24)) are solved with the pressure term from the previous time-step. This is called the momentum prediction step. The discretise RANS equations can then be inserted into the continuity equation to make an equation for the pressure. Using the preliminary results from the momentum prediction step, the equation for the pressure, called the pressure correction equation, can be solved. This gives an updated pressure field, which can then be used to update the velocities [10, 22].

The pressure velocity coupling used in the simulations are called PIMPLE, and is a combination of two other pressure-velocity couplings [12]. The first is the SIMPLE (Semi-Implicit Method for Pressure Linked equations) algorithm. This solves the algorithm describe above directly. The SIMPLE algorithm was originally developed for steady-state simulations, and requires a lot of iterations to reach a converged solution for the velocity field. The other is the PISO (Pressure-Implicit with Splitting of Operators) algorithm. This was created for transient simulations, and solves the pressure correction equation more than once, updating the velocities in between. In the PIMPLE algorithm one can than specify how many times both the overall algorithm and the pressure correction equation should be solved for each time-step [10, 22, 70].

For the fluid region, the PIMPLE algorithm was used with residual control, monitoring the drop in the residual values for the pressure and the enthalpy. The equations are then solved until a specified drop in the residuals is achieved. 10^{-4} was used for the pressure and 10^{-6} for the enthalpy. The overall solution for all the regions was only solved once before going to the next time step.

Under-relaxation was used in the PIMPLE algorithm for stability. For the pressure 0.3 was used, while 0.7 was used for the other variables.

The discretisation schemes used to discretise the equations were all first or second order, with second order upwind being used for most of the parameters.

Simulation domain and boundary conditions

The one-row simulation domain is shown in Figure (19). This domain is used in the y^+- investigation (see section 3.2) and in the investigation of turbulence models (see section 3.3). An assumption is made that the gas side of the heat exchanger can be modelled as dry air. The simulation domain then consists of an air region, and a solid fin and solid tube region. Only the air region and the fin region are solved for.

The one-row simulation domain consists of a section of a finned-tube, shown in Figure (19b), and the surrounding air. An inlet and outlet length are added to the air region, as seen in Figure (19). The section of the finned-tube that is modelled consist of a fin and half of the tube length between the two adjacent fins, as seen in Figure (19b). Cyclic boundary conditions are then used to represent the full width and height of the row of finned-tubes.

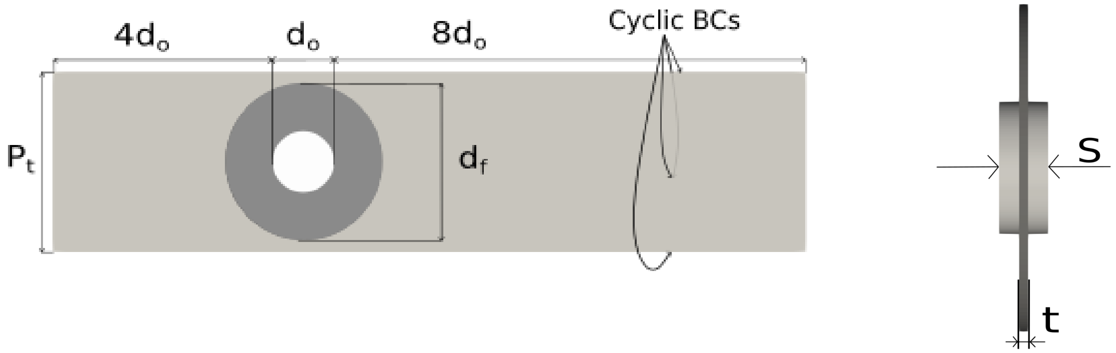

(a) (b)

Figure 19: The one-row domain including the dimensional parameters and the cyclic boundary conditions

The values for the dimensional parameters shown in Figure (19) are given in Table (1).

Table 1: Dimensions relating to the one-row computational domain

Name :	Tube diameter (d_o)	Fin diameter (d_f)	Fin pitch (S)	Fin thickness (t)	Transverse pitch (P_t)
Dimensions [mm] :	13.5	33.5	2.81	0.5	38.7

As seen in Figure (19), four of the sides has cyclic boundary conditions. The four sides are the top and bottom, and the left and right side. The other boundaries are the inlet and outlet, and the air interface with the fins and the tube walls. The flow goes from left to right, which means the inlet is at the left and the outlet is at the right in Figure (19a) The boundary conditions applied at these boundaries are shown in Table (2).

Table 2: Boundary conditions for the boundaries in the one-row simulation domain not having cyclic boundary conditions

Name	**Inlet**	**Outlet**	**Tube walls**	**Fins**
Temperature	Fixed T_{in}	Inlet/Outlet	Fixed T_w	Coupled
Velocity	Fixed U_{in}	Inlet/Outlet	No slip	No slip
Pressure	Zero Gradient	Fixed p_{atm}	Fixed flux pressure	Fixed flux pressure
Turbulence variables	Fixed value	Zero gradient	Fixed value/ wall function	Fixed value/ wall function

As can be seen from Table (2), all but the pressure has a fixed, constant value at the inlet. The temperature has a constant inlet value of $T_{in} = 398$ K in all the simulations. The velocity U_{in} is calculated from the wanted Reynolds number Re_{do} using equation (31), while the turbulence variables depend on the turbulence model. The inlet values for the variables are calculated from the estimation equations given in the OpenFOAM user guide [39]. For the reference length used in these estimation the tube diameter d_o is used and for the reference velocity U_{in} is used. The turbulent intensity was set to $I = 1\%$. For the SA turbulence model no equation is given, however, the calculation of the inlet value for this parameter and ν_t is described in section 3.4. For calculation of $R_{i,j}$ for the LRR turbulence model the postprocessing function "R" was used. Finally, the value for α_t was calculated from ν_t using the turbulent Prandtl number ($Pr_t = 0.85$).

At the outlet, the temperature and velocity use an "Inlet/Outlet" boundary condition. This is a more stable version of the zero gradient boundary condition, which handles backflow better if present. The zero gradient boundary condition sets the normal gradient of the parameter at the boundary to zero [13].

For the pressure, the outlet was set to a fixed value $p = p_{atm}$, where p_{atm} is the atmospheric pressure. For this one bar was used.

For the tube walls, the temperature was set to a constant value $T_w = 298$ K in all the simulations. The velocity was set to zero, and the pressure was set to a boundary condition called "Fixed flux pressure". This boundary condition behaves like a zero gradient boundary condition, but should handle forces due to the pressure better [13]. For the turbulence variables wall functions were generally used. Wall functions are described in section 3.2. There are, however, two exceptions to this. The first is for the Transition SST turbulence model (see section 2.1) where a zero gradient boundary condition is specified for two of the variables. The second is for the y_p^+ investigation where the simulations without wall functions used a constant value of zero.

For the fins, all but temperature had the same boundary conditions as for the tube walls. For the temperature, a coupled boundary condition was used. This to allow for conjugate heat transfer between the fins and the air. For the fin-to-tube boundary the temperature was set to T_w.

Thermophysical properties: For the air side, all the thermophysical properties but the density is sat to a constant value. The air is modelled as dry air, and the values are evaluated at the inlet temperature (T_{in}). For density, the ideal gas law is used. According to Eide [37], the usage of the ideal gas law can be justified if the pressure drop is not too large and according to Lindqvist et al. [34] the usage of constant values can be justified if the simulations concerns gas cooling, as it does here. The thermophysical properties needed to be specified were, the dynamic viscosity where $\mu = 2.25 \cdot 10^{-5}\ Pa \cdot S$ was used. The specific heat at constant pressure where $C_p = 1000\ J/(Kg \cdot K)$ was used, and the Prandtl number where $Pr = 0.7$ was used.

For the fins, aluminium is used as material, and the thermal conductivity is set to $K_{alu} = 193\ W/(mK)$. This value is collected from Lindqvist et al. [34], and corresponds to the conductivity for the aluminium finned-tubes tested by Holfeld [17]

OpenFOAM - Case set up and meshing

The software used for the simulations were OpenFOAM v8 [11]. The OpenFOAM solver used for the simulations is "chtMultiRegionFoam". This is a pre-existing solver which solves conjugate heat transfer problems where heat is transferred between different regions. The regions can be both solid regions and fluid regions.

The simulations were transient and were run until the flow was fully developed and the velocity and pressure drop did not change significantly anymore. Then the flow was "frozen" and only the energy equation (see equation (25)) was solved. The iterations were stopped when the heat duty stabilised.

The time-step used in the simulations were given indirectly through a maximum Courant number. The time-step is then updated by OpenFOAM according to local mesh size and local changes in field values. A Courant number of 0.75-0.95 was used.

The modelled finned-tube geometries were drawn in the open-source CAD software Blender v2.90. The geometries were then saved as stl-files which were used as input in the grid generation. The grid generation was performed in OpenFOAM using the inbuilt tool "snappyHexMesh". "snappyHexMesh" requires a background grid consisting of cubes, this was created using the tool blockMesh. The size of the sides in these cubes (h) was decided in the grid convergence test described in the next section. This background grid had the same overall size as the simulation domain shown in Figure (19) with dimensions shown in Table (1). The cyclic boundary conditions were also set at this stage.

A more in-depth description of how "snappyHexMesh" works can be found in the OpenFOAM user guide [14]. However, in short terms, the grid generation in "snappyHexMesh" consists of three stages.

Firstly, a refinement by dividing the cubic cells in the background grid into smaller cubes near the geometries provided in the stl-files. Secondly a "snapping" process where the cells in the refined mesh are split to fit the shape of the geometries. In this "snapping" process the cells in the mesh goes from being purely cubic to having an arbitrary shape near the geometries dictated by the shape of the geometries. The last stage is to insert layers in the mesh near the geometries. This is done to get a finer mesh near the geometries.

After the grid generation, the mesh was split into an air, a fin and a tube region, before the appropriate boundary conditions described above were set. The boundary conditions were set using the tool "changeDictionary", which allows for all the boundary conditions in a region to be set simultaneously.

Grid convergence

To find a suitable size for the cells in the background mesh, a grid convergence test was performed using the one-row model. A grid convergence test for this geometry was also done in the project thesis [65]. The size differences of the cells in the test were, however, quite large, with $h = 0.3$ mm, $h = 0.5$ mm and $h = 1.0$ mm. The difference in the results between the mesh with $h = 0.3$ mm and with $h = 0.5$ mm was around 6% for Nu and around 3% for Eu. h here describes, as mentioned, the side length of the cubes in the background mesh.

The new grid convergence test used background meshes with cube sides $h = 3$ mm, $h = 3.65$ mm and $h = 0.5$ mm. The simulations were run at a Reynolds number Re_{do}=1000.

The results for relative differences in Eu and Nu between the different meshes are shown in Figure (20). The relative difference is the results divided by the results of the finest mesh. This means the results for the finest mesh is by default unity.

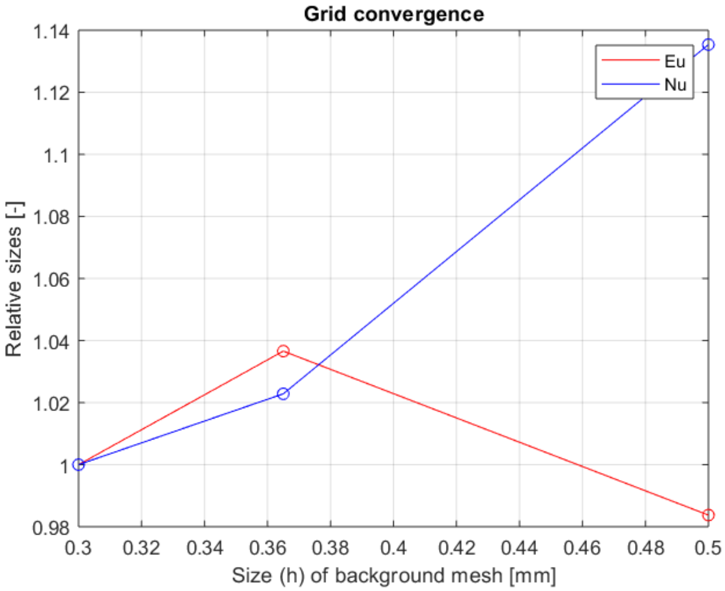

Figure 20: Grid convergence at $Re_{do} = 1000$ for one-row model, showing the relative values compared to the finest grid for Eu and Nu

As can be seen from Figure (20), the difference in the result using a mesh with $h = 0.3$ mm and $h = 0.36$

mm is around 4% for Eu and 2% Nu.

The 6% difference between using a mesh with $h = 0.3$ mm and $h = 0.5$ found in the result for Nu in the project thesis is not replicated here. Instead, the difference is almost 14%. Why this is, is not clear, but a possibility is that the new simulation with $h = 0.3$ mm has a better mesh than the simulation used in the project thesis.

Based on these results, $h \approx 0.35$ mm is chosen as a good enough value for the size of the cube sides in the background mesh.

It is worth pointing out that this grid convergence test was performed at a low Reynolds number. The validity of the results at higher Reynolds numbers and for the full bundle domain were not tested. This was, however, tested by Lindqvist et al. [34]. Lindqvist et al. [34] performed a grid convergence test for the same full bundle geometry modelled in this thesis, and at a higher Reynolds number. From the results of this grid convergence test, Lindqvist et al. [34] suggested that the background grid should not be much larger than $h = 0.3$ mm for this geometry. Interpolating to $h = 0.35$ mm in the results by Lindqvist et al. [34] suggests around a 2.5% overprediction in the result for Nu compared to the result for $h = 0.3$ mm. For Eu, the value was higher. This matches fairly well with the results at $h = 0.365$ mm in Figure (20).

3.2 y_p^+ investigation

The main shortcoming of the model developed in the project thesis [65] was its inability to predict values of Nu, Eu and Sr accurately. Almost all the predicted values of the three parameters lay outside the error band of the correlations used for comparison. This was a trend that seemed to get worse with increasing values of y_p^+.

To investigate if this shortcoming was caused by y_p^+ being too large, an investigation of y_p^+ was conducted. Lindqvist [33] recommended to fully resolve the physical behaviour of the flow, and not use wall functions. To test this, an investigation into the usage of wall functions was also performed. For situations where both the RANS equations (see equation (24)) and the energy equation (see equation 25) are solved, Tannehill et al. [58] recommended y_p^+ around one to two.

y_p^+ is here defined as the dimensionless distance to the first cell centre y_p. A velocity scale is used to make the distance dimensionless. For y^+ the shear-velocity $u_\tau = \sqrt{\frac{\tau_w}{\rho}}$ is used, where τ_w is the wall shear-stress. The definition of y_p^+ then becomes [70, 25]:

$$y_p^+ = \frac{\rho \cdot u_\tau \cdot y_p}{\mu} \tag{26}$$

The investigation is carried out to firstly find the dependency on y_p^+ in the results and then find how large y_p^+ can get before there is significant change in the results. Having a fine enough mesh to resolve the details of the flow in the boundary layer usually means having a y_p^+ value of around one. Resolving the flow behaviour in the boundary layer is computationally heavy. Wall functions are, for this reason, usually applied to wall boundaries in simulations. Wall functions represent models for how the flow behaves very close to a wall. These are then applied to ensure that the velocity gradients near the walls (and thus the shear stress) are computed correctly in the simulation. The idea of using wall functions is that one can get away with a coarser mesh. This mesh do not resolve the flow in the boundary layer, but instead models it using empirical models [9, 70]

Wall functions

Gradients are usually largest near the walls, which means a very fine grid is needed to accurately capture and resolve these gradients. Using wall functions, the first cells near a wall is assigned a non-linear general profile. This profile models the near-wall flow as described by the law of the wall. For the momentum, the law of the wall gives a relationship for the shear stress variation in the boundary layer. Going from the viscous sublayer ($y^+ \lesssim 5$), where molecular viscosity dominates, to the log-law region ($30 \lesssim y^+ \lesssim 300$), where turbulent viscosity dominates. Empirical relations stemming from experiments and DNS simulations of a flat plate describes this variation. This variation is, more or less, universal very close to the wall [5].

These relations can be related to the transport variables in the utilised turbulence model, and from this be used to describe the near wall behaviour of these variables.

The law of the wall can also be applied to the temperature gradient near the wall. This is done through a dimensionless temperature which goes to zero at the wall. Through DNS simulations this profile is shown to have a similar shape as the near-wall velocity. These temperature profiles are, however, a function of the Prandtl number; the molecular Prandtl number (Pr) in the viscous sublayer and a turbulent Prandtl number (Pr_t) in the log-law region. Pr_t is usually set to a constant value a little smaller than unity (in this thesis sat to $Pr_t = 0.85$), while the molecular Pr is fluid dependent. This dependency means the near-wall temperature profile depends on the fluid, and the regions in the law of the wall are no longer close to universal. This is included to get the gradients, and thus the heat transfer, correct. [5].

Most wall functions only have models for the viscous sublayer ($y^+ \lesssim 5$) and the log-layer ($y^+ \gtrsim 30$). [70]. However, some wall functions include modelling of the whole range, including the buffer-region ($5 \lesssim y^+ \lesssim 30$) between the viscous sublayer and the log-layer. One such model in OpenFOAM is the "nutUSpaldingWallFunction". This is based on Spaldings law for continues description of near-wall flow. The higher y^+ gets, however, the further away from the universal behaviour near the wall the flow gets. Here the effect of the geometry gets more pronounced [25, 5]. The "nutUSpaldingWallFunction" is the wall function used in the investigation below [9].

A wall function is also applied for α_t which is the turbulent diffusivity. This utilises the connection to ν_t through the turbulent Prandtl number.

It is worth pointing out that another definition of a dimensionless distance from the wall is also in use. This is called y^* and uses the square root the turbulent kinetic energy (k) as a velocity scale. The advantage to this is that k is defined in separation points where the velocity gradient and thus the shear-velocity is zero [5].

Results of the y_p^+ investigation

The investigation of y_p^+ is performed using the one-row model, with the Spalart-Allmaras turbulence model at a Reynolds number $Re_{do} = 1000$. Seven simulations were conducted, with the maximum y_p^+ value from each simulation being used for comparison. This value ranged from $y_p^+ = 0.816$ to $y_p^+ = 3.24$. Simulations with and without wall functions were performed for the two coarsest meshes. A simulation using an adiabatic boundary condition at the fin tip was also conducted. Below are the results for the Nusselt number (Nu), the Euler number (Eu) and Strouhal number (Sr).

The Nusselt number: The heat transfer coefficient, Nu, is calculated as described in section 3.6. The results for Nu are shown in Figure (21) along with the correlation by Huisseune et al. [19] shown in equation (15). The error band in the correlation by Huisseune et al. [19] is according Huisseune et al. [19] only ±11%.

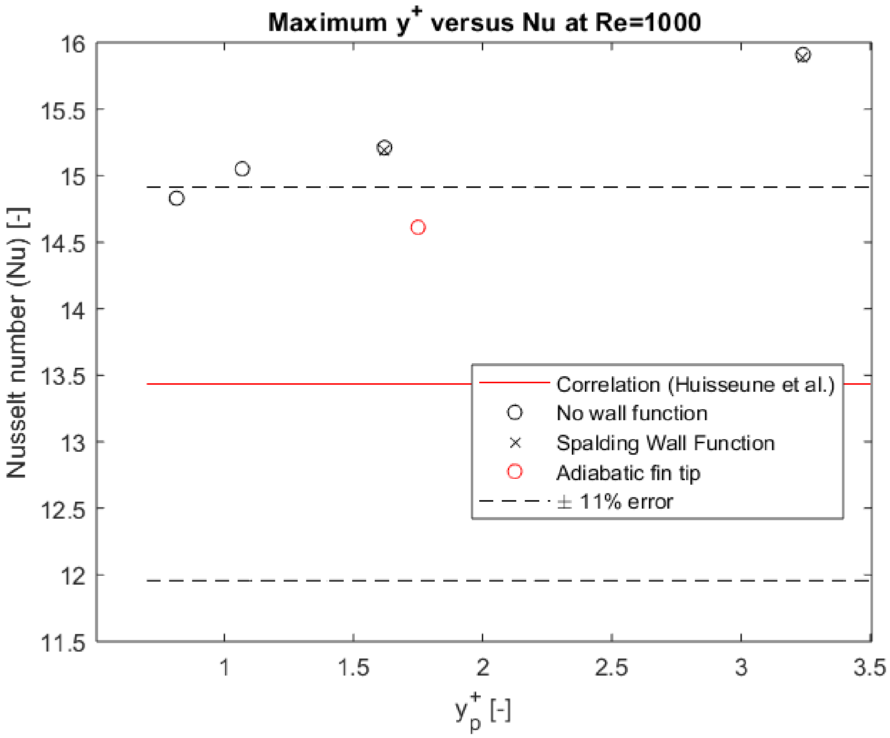

Figure 21: The results for the Nusselt number at different y_p^+ values, along with the correlation by Huisseune et al. [19]

As can be seen in Figure (21), all of the simulations overpredicted the correlation. The overprediction ranged from 10% to 18% for the simulations where heat transfer at the fin tip is included. This indicates that y_p^+ being too large might explain some of the deviation from the experimental correlations found in result for Nu in the project thesis. There are, however, no apparent difference in the simulation results with wall functions and without wall functions.

As can be seen if Figure (21), the difference between a y_p^+ value of between 1.5 and 2 only differs by around 3% from a y_p^+ value smaller than one. This is also in good agreement with the recommendation by Tannehill et al. [58].

A lot is happening at the fin tip where the flow impinges. To investigate how much influence the heat transferred to this edge has on the overall Nu a simulation using an adiabatic fin tip was performed. This is, of course, unrealistic, but one expects the fin tip to have a local heat flux approximately equal to the local heat flux on top of the fin, near the edge. By removing both the area and the heat flux from the fin tip in the calculation of Nu, the overall Nu should not change significantly.

The leading edge of the fin has a high y_p^+ value due to the stagnation and subsequent deflection of the flow away from the edge. All these changes in the flow field makes this edge hard to model accurately. The highest values of y_p^+ in all the simulations are found near the leading edge of the fin and near the stagnation point at the base of the fin. All the simulations had an average y_p^+ value less than one. This means extra computational resources are used trying to resolve the flow near the leading edge of the fin without knowing if it is captured accurately.

Figure (21) shows that having an adiabatic fin tip versus including this area in the calculation makes a difference. The heat transfer to the fin tip seem to increase Nu by around 4% compared to the simulation with an adiabatic fin tip. Although not insignificant, this difference is not very large. However, since the simulation with an adiabatic fin tip deviates less from the correlation, it is assumed that using an adiabatic fin tip provides a more accurate result for Nu. An adiabatic boundary condition at the fin tips will therefore generally be applied to the simulations unless else is stated.

The Euler number: The result for the pressure drop, Eu, is calculated as described in section (3.6). Eu is shown in Figure (22) along with the correlation by Nir [54] shown in equation (21).

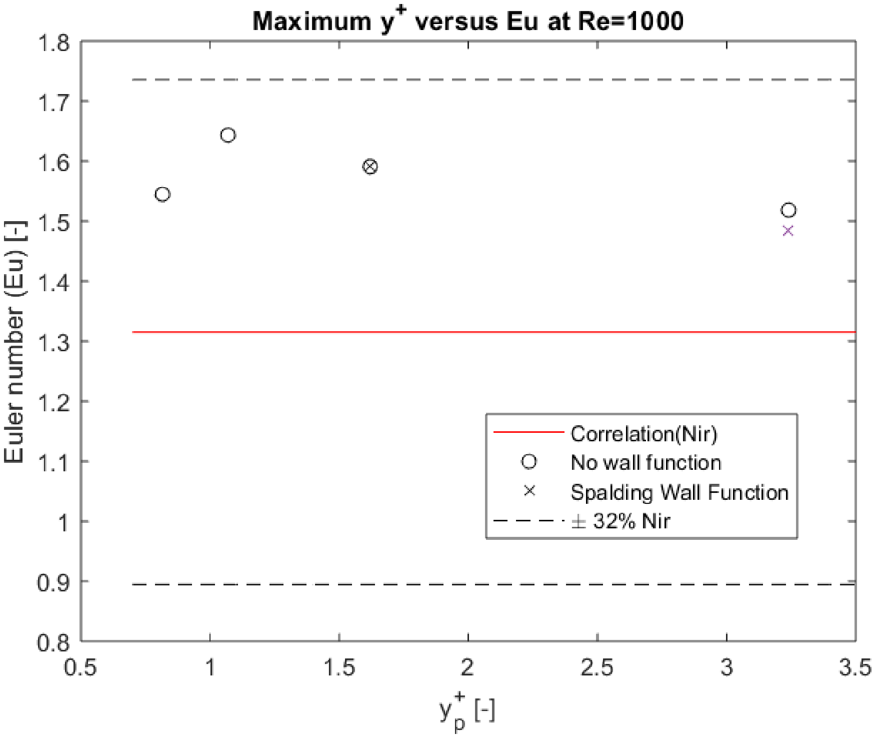

Figure 22: The results for the Euler number at different y_p^+ values, along with the correlation by Nir [54]

As can be seen from Figure (22), the resulting values lie quite close together, with the difference between $y_p^+ < 1$ and $y_p^+ = 3.24$ being around 4%. There are, however, larger differences in the results in between these values. The error band for the correlation of ±32% is taken from Holfeld [17]. As can be seen in figure (22), all the simulation results are within this error band. For $y_p^+ = 3.24$ there is a marginal difference between the simulation with and without wall functions. The simulation without wall functions is, however, closer to the simulation with $y_p^+ < 1$. In the investigated y_p^+ range, Eu do not seem to be very sensitive to the y_p^+ value. There do not seem to be a significant difference between applying wall functions or not either. So, unlike for Nu, the deviation from the experimental correlations in the result for Eu found in the project thesis do not seem to have been caused by y_p^+ being too large.

The Strouhal number: The results for the vortex shedding behaviour are shown in Figure (23). The vortex shedding behaviour is presented on dimensionless form in terms of the Strouhal number (Sr). The results are compared with a reference value of $Sr \approx 0.19$ taken from Mair et al. [41]. Sr is evaluated by first finding the vortex shedding frequency (f_{vs}). f_{vs} is found from plotting the lift coefficient C_l and reading of the oscillation period. The Strouhal number is then calculated using: $Sr = \frac{f_{vs} \cdot d_{eff}}{u_{(A_{min})}}$, where d_{eff} is an effective diameter proposed by Mair et al. [41]. The method is taken from Lindqvist et al. [35]. It should be noted that other authors have proposed different values for Sr, but they all seem to lie around 0.2.

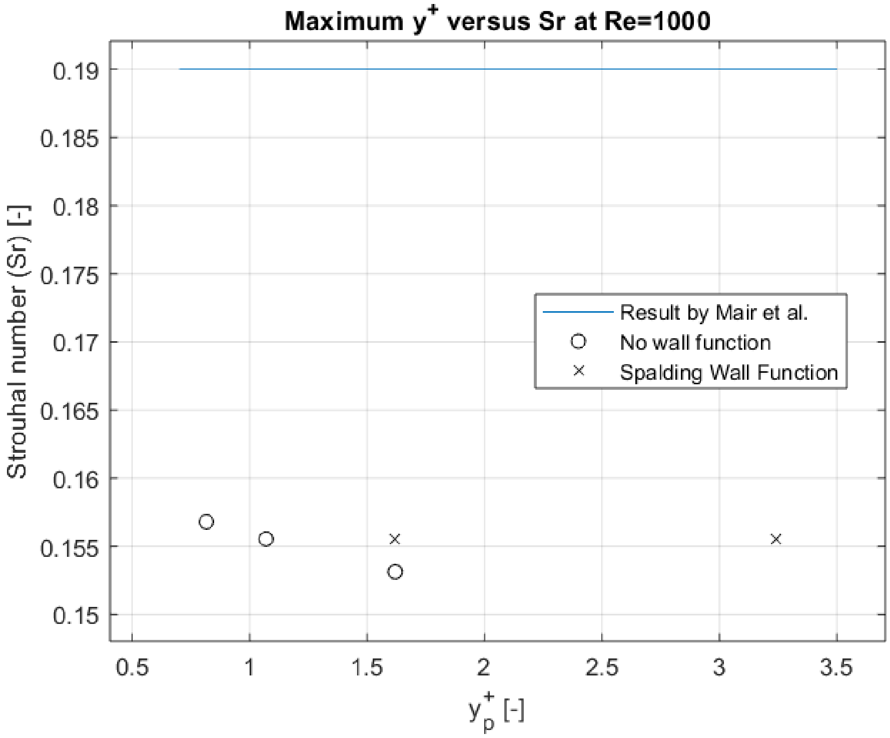

Figure 23: The results for the Strouhal number at different y_p^+ values, along with three correlations for predicting Nu

The results are, as seen in Figure (23), consistently off, with all of the simulations being around $Sr \approx 0.155 \pm 2.5\%$. This might be an indication that the velocity gradient in the boundary layer is not reproduced correctly, causing the value of Sr to be off the reference value by more than 20%. The deviation from the reference value do not seem to be caused by either y_p^+ being too large or by using or not using wall functions. What causes this deviation is not investigated. The calculation of C_l was unsuccessful for the simulation with $y_p^+ = 3.24$ and no wall functions. For this reason, no result for Sr could be calculated for the simulation.

General findings in the y_p^+ investigation

For Eu and Sr, the results do not seem to be very sensitive to the y_p^+ value. For Nu, there is little difference in the answer for $y_p^+ \lesssim 2$. For Nu, this is in accordance with Tannehill et al. [58].

The results still deviates some from the experimental correlations. The largest difference is for Sr, as seen in Figure (23). Why this is, is as mentioned, not clear. However, in the next section regarding different turbulence models the results indicated it might be down to the turbulence model.

As can be seen in Figure (21), some differences were found in the results between including the heat transfer to the fin tip and using an adiabatic boundary condition at the fin tip. This indicates that the complex flow at the fin tip is not properly represented even if the grid is resolved down to $y_p^+ < 1$. Not including the heat transfer to the fin tip and instead use an adiabatic boundary condition at the fin tip is therefore assumed to provide a more accurate answer for Nu. An adiabatic boundary condition at the fin tip will therefore be used in the rest of this thesis, if nothing else is stated.

From the results for Nu shown in Figure (21), y_p^+ should ideally be kept under two. For the difference between using and not using wall functions, there seems to be no significant difference, as seen in Figures (21), (22) and (23). It should be noted that the behaviour of y_p^+ observed here does not necessarily scale with the Reynolds number, so the error of doing simulations with $y_p^+ > 2$ might be higher for higher Reynolds numbers. Since the simulation is done at a low Reynolds number, the full benefit of using wall functions might not show up. Wall functions will therefore be used in the rest of this thesis.

It is worth pointing out that this investigation was not performed in the most ideal way. Some of the changes in y_p^+ were achieved changing the background grid, not the refinement near the wall. The background grids used are in the range 0.25 mm $< h <$ 0.365 mm. In a proper investigation of y_p^+ the background grid should be kept at the converged size found in a grid convergence test while y_p^+ is changed by altering the refinement near the walls. In this investigation two parameters that can influenced the result was changed simultaneously.

3.3 Turbulence models

Using the Spalart-Allmaras turbulence model and having $y_p^+ > 1$ were thought to be the reasons for deviation from the experimental correlations found all the results in the in the project thesis [65]. The y_p^+ value was challenged in the section above. The results indicated that a large y_p^+ value will influence the answer. To further challenge the one-row simulation model, some other suitable turbulence models were tested. These turbulence models are all described in section 2.1.

In this section, the results of simulations with different turbulence models are presented and discussed. The simulations were performed using the one-row model, and all the simulations had a turbulent intensity $I \approx 1\%$ at the inlet. All the simulations used wall functions. However, the simplification of using an adiabatic fin tip was not used. This was because some of the simulations were run prior to deciding on this simplification. Therefore, to keep the simulations as similar as possible, it was neglected in all of them.

For the simulations at $Re_{d_o} = 1000$ either the mesh with $y_p^+ \approx 1$ from the y^+ investigation (see section 3.2) was used or a mesh made with the same input parameters in OpenFOAM. For the simulations with the Spalart-Allmaras and $k-\omega SST$ turbulence model at $Re_{d_o} = 600$ and at $Re_{d_o} = 5000$, the same meshes were used to keep the comparison as similar as possible.

Heat transfer

The heat transfer coefficient, Nu, is calculated as described in section 3.6. The results for Nu are shown in Figure (25). The correlation by Nir [54] shown in equation (16) and the correlation by Huisseune et al. [19] shown in equation (15) are used for comparison.

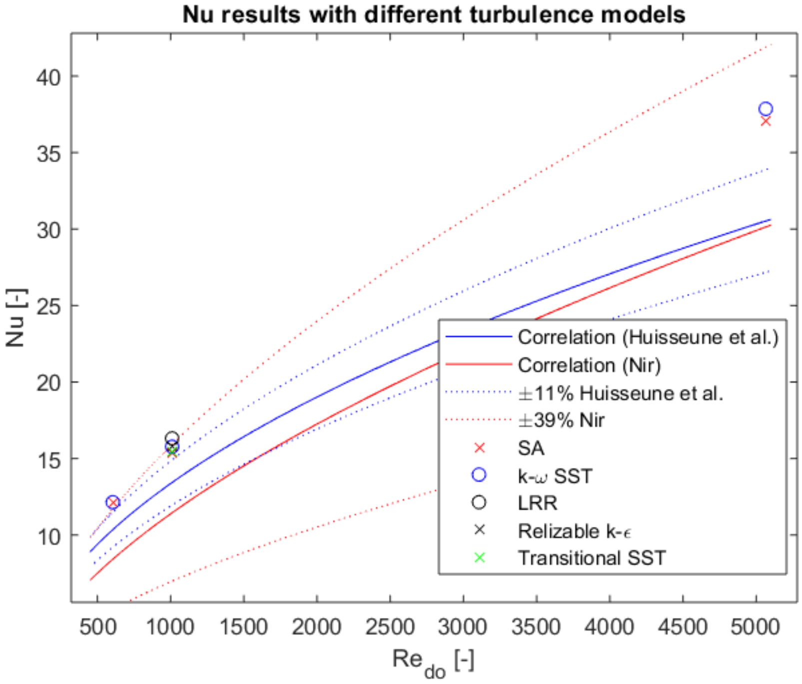

Figure 24: The resulting Nusselt numbers from simulations with different turbulence models. The results are compared with the correlations by Nir [54] and Huisseune et al. [19]

As can be seen from Figure (24), all the simulations over-predicted the correlations. The results at $Re_{do} = 600$ are outside the error band of the correlation by Nir [54], while at $Re_{do} = 1000$ the results are mostly inside the error band. The highest Reynolds number results are within the error band of ±39% for the correlation by Nir [54]. None of the simulations are within the error band of the correlation by Huisseune et al. [19]. This might indicate that the error band for the correlation by Huisseune et al. [19] is too strict. The error band in the correlation by Huisseune et al. [19] is taken from Huisseune et al. [19], while the error band for the correlation by Nir [54] is taken from Holfeld [17]. There is, however, very little difference between the results for the different models. It should be mentioned that at $Re_{d_o} = 1000$ the results are grouped so closely together that all the different points are not clearly visible due to overlapping. It is also worth pointing out that the much more computationally heavy LRR model is the furthest away from the correlations, and the only simulation at $Re_{do} = 1000$ outside the error band of the correlation by Nir [54].

Pressure drop

The pressure drop in terms of the Euler number is calculated as described in section 3.6. The results for Eu are shown in Figure (25). The correlation by Nir [54] shown in equation (21) is used for comparison.

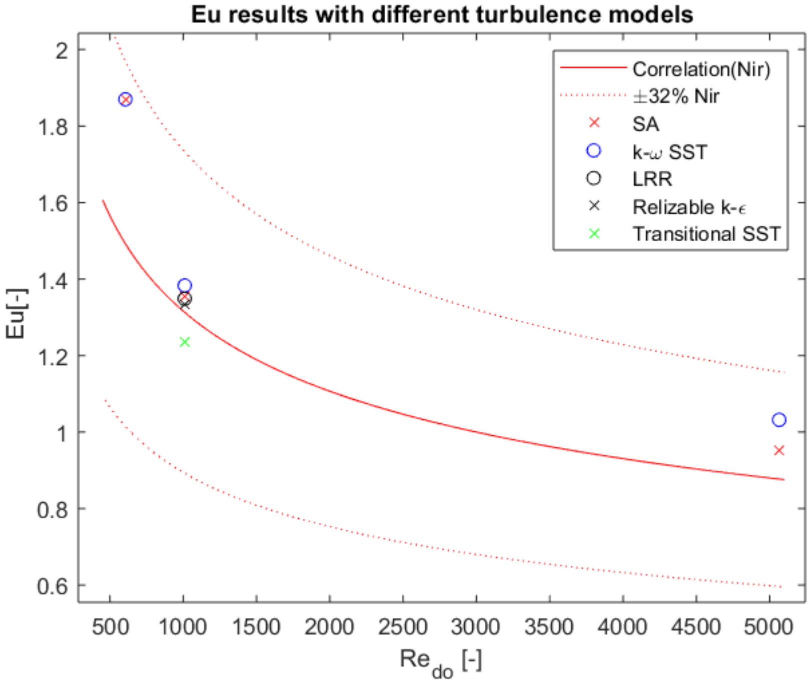

Figure 25: The resulting Euler numbers for the simulations with different turbulence models. The results are compared with the correlation by Nir [54]

Figure (25) shows the results for Eu has a little more difference between the models than was present for Nu. At $Re_{d_o} = 5000$, the SA model is closer to the correlation than the $k-\omega SST$ model. At $Re_{d_o} = 1000$, all but the Transition SST model are grouped together close to the correlation. The Transition SST turbulence model is supposed to be more accurate at such low Reynolds numbers. Whether this is an indication that the Transition SST model is more accurate, with the other models under-performing, is not clear. As for heat transfer, the LLR model does not out-perform the turbulent viscosity models.

It should be mentioned that a lot of uncertainty can be expected of the correlation. Holfeld [17] reporting that for a 95% confidence interval, the error band is ±32%. The comparison by Holfeld [17] was for a bundle and not one row of finned-tubes. According to Nir [54] the correlation is also valid for one row of finned-tubes, as described in section 2.5. However, how accurate the correlation is for one-row of finned-tubes is not clear.

A visual comparison

Nu and Eu represents integrated averaged values. They can therefore not be used to tell if the local flow and heat transfer over the finned-tube is well represented. To investigate this, a visual comparison of both the streamlines and the local heat transfer coefficient over the fin was done. This was done for all models at $Re_{d_o} = 1000$. The resulting streamlines for the Spalart-Allmaras, $k-\omega SST$ and Transition SST model are shown in Figure (26). The streamlines for all the models are shown in appendix A.

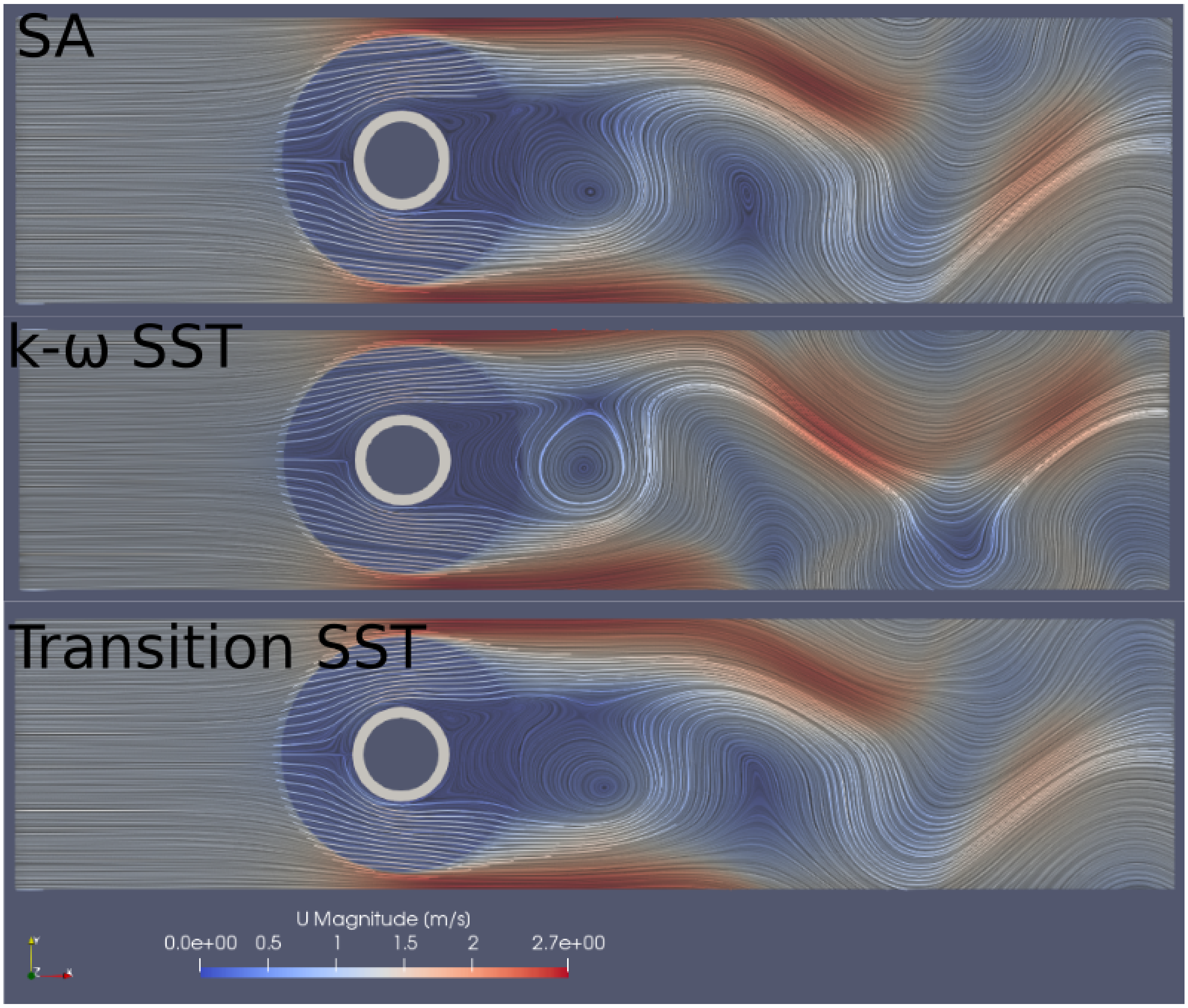

Figure 26: Streamlines of the flow over the finned-tube simulated with the Spalart-Allmaras (SA), $k-\omega SST$ and Transition SST turbulence model at $Re_{d_o} = 1000$

As can be seen in Figure (26), there are some differences in the recirculation zones, although the general flow patterns are similar. This is true for all the models (see appendix A). The flow separation from the tubes seems to be somewhere between $90° < \theta < 110°$ (using the angle from the inflow defined in Figure (2) in section 2.2). For the separation from the fins the angle seem to be slightly higher, although it is hard to tell exactly. This is fairly similar to the result by Nemati et al. [53] described in section 2.1.

It is worth pointing out that the flow a little further behind the finned-tubes do not seem very turbulent, with the recirculation zones taking a different form compared to Figure (5) in section 2.2. This might be a reflection of the low Reynolds number $Re_{d_o} = 1000$ used in this comparison. The low Reynolds number can, of course, have interfered with the validity of the results. However, there do not seem to be a significant difference in flow patterns between the fully turbulent models and the Transition SST model which should work for partially laminar flows.

The distribution of the heat transfer coefficient over the fin for the Spalart-Allmaras, $k - \omega SST$ and Transition SST model is shown in Figure (27). The distributions of the heat transfer coefficient for all the turbulence models are shown in appendix B. The distribution of Nu is calculated for the heat flux using the method described in section 3.6. The same reference temperature $T_{ref} = 376$ K is used for all the models.

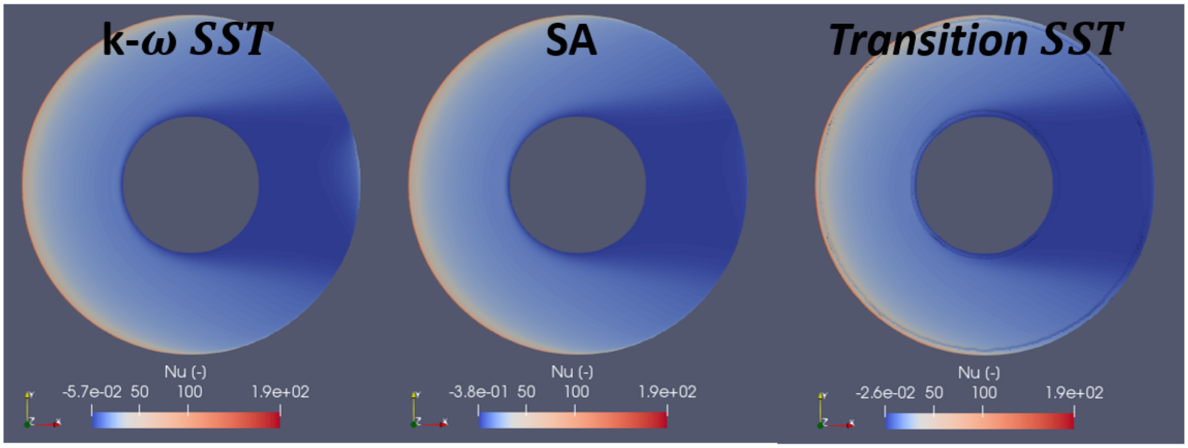

Figure 27: The distribution of Nu over the fin for the simulations using the Spalart-Allmaras (SA), $k-\omega SST$ and Transition SST turbulence model at $Re_{d_o} = 1000$

As can be seen from Figure (27), there is little visual difference between the models. The exception is the LRR turbulence model shown in appendix B which has a 10 % lower maximum Nu compared to the rest of the models. All the models have the highest local heat transfer coefficient at the leading edge of the fin, going up to around $\theta = \pm 90°$. This is caused by flow impingement. The models also have the zone of low heat transfer behind the tube due to the wake. At the trailing edge of the fin there is slight increase in Nu due to backflow. This increase is less visible in the SA and Transition SST model compared to the rest, but still present.

None of the models do, however, show a higher heat transfer coefficient near the frontal base of the fin. As described in section 2.2, a higher local heat transfer coefficient is expected here due to the formation of horseshoe vortices. The reason horseshoe vortices are not visible is most likely due to the low Reynolds number.

It is also worth pointing out that results for all the models have a zone behind the tube where Nu has the opposite sign. This is believed to be a numerical error. What causes this error is not clear. The largest magnitude in this zone is found for the SA model, and the smallest is found for the Transition SST model, as shown in Figure (27). The magnitudes of this zone in all the results are, however, close to zero.

Apart from a difference in the maximum value for Nu between the LRR model and the rest, there is very little difference between the models. Both qualitatively and quantitatively.

Choice of a suitable turbulence model

The overall results for the simulations with different turbulence models were relatively similar, and the same for the physical flow and heat transfer representation seen in the visual comparison. In selecting the most suitable turbulence model for the problem the stability of the model during simulation is also considered.

The $k-\omega$ SST model and the SA model were chosen for further investigation, and simulations at $Re_{do} = 5000$ and $Re_{do} = 600$ were conducted. At $Re_{do} = 5000$ the SA mode is closer to the correlations for both Eu and Nu as seen in Figures (24) and (25), although the difference in the results for Nu is minimal. At $Re_{do} = 600$ both the result Eu and Nu are almost identical for the two models, as see Figures (25) and (24). It should, however, be mentioned that $Re_{d_o} = 600$ represents a laminar case, with the results being of very little utility.

From these results, the SA model is shown to produce results being closer to the correlations than the $k-\omega SST$ model, indicating that it is a little more accurate. As the SA model is also the simplest and the most stable model it was chosen over the $k-\omega SST$ turbulence model.

This is an interesting result, since the investigation was conducted because it looked like the SA turbulence model was under-performing in the project thesis [65]. Here, it was, however, shown to be the best performing model. This result is, however, similar to the result by Lindqvist et al. [34] where the SA model was found to produce results closer to experimental data and correlations compared to the $k-\omega SST$ model.

It is interesting to mention that there is a lot of difference in the y_p^+ values between the models, even though the same mesh or a mesh made with the same input parameters were used. Since distance to the first cell centre in the mesh is the same, this means the shear velocity (and thus the wall shear stress) must be different. The implications of this with regards to calculating lift and drag were not investigated. This might, in part, explain the deviation found in the y_p^+ investigation with regards to Sr. Further investigations into this should be conducted.

3.4 Full bundle model

Implementing a full bundle model is, to a degree, a straight extension of the one-row model described in section 3.1. Although a few changes were made. Apart from the change of adding more rows to model a full bundle, most of the changes were made in the grid generation process.

The full bundle is here represented by a full bundle simulation domain. This consists, initially, of a finned-tube bundle with eight rows. To model the full height and full width of the bundle, cyclic boundary conditions are used. This is analogous to the one-row model described in section 3.1. As described in section 1, this way of modelling is assumed to be representable for a full bundle.

An assumption is made that the findings in the investigations using the one-row model holds true for the full bundle model. This means a grid of $h = 0.35$ mm, as found in the grid convergence test in section 3.1, is used alongside the Spalart-Allmaras turbulence model, as found in section 3.3. The simplification of using an adiabatic boundary condition at the fin tip is also used.

Simulation domain and boundary conditions

The simulation domain for the full bundle is shown in Figure (28). The finned-tubes modelled are the same as the finned-tube modelled in the one-row model shown in Figure (19b).

Figure 28: Full bundle simulation domain

For every other row, half of the finned-tube is on each side of a cyclic boundary, as seen in Figure (28). The initial full-bundle model has dimensions given in Table (3). For the investigation of geometry parameters of the finned-tubes and finned-tube bundles, the changed values for the geometry parameters are given when the results are presented in section 4.2.

Table 3: Dimensions relating to the computational domain

Name:	Dimensions [mm]	Name:	Dimensions [mm]
Tube diameter (d_o)	13.5	Transverse pitch (P_t)	38.7
Fin diameter (d_f)	33.5	Longitudinal pitch (P_l)	33.5
Fin pitch (S)	2.81	Fin tip clearance (C_f)	5.2
Fin thickness (t)	0.5		

The boundary conditions are more or less the same as for the one-row simulation domain described in section 3.1. The biggest difference is using cyclic AMI (Arbitrary Mesh Interface) boundary conditions instead of cyclic boundary conditions. These behave as cyclic boundary conditions, but do not require the mesh on the coupled boundaries to be one-to-one. This means the simulation will run with small imperfections in the mesh such as a different number of cells on the two sides of the cyclic boundary.

The domain has now grown to 12 solid fin or half-fin regions, 12 solid tube or half-tube regions and an air region. The fin regions use the same boundary conditions as the fin in the one-row domain and the tube regions as the tube in the one-row domain. These are shown in Table (2) in section 3.1. The exception is the fin-tip where an adiabatic zero gradient boundary condition is used.

Only the Spalart-Allmaras turbulence model is used in the full bundle simulations. The boundary conditions for the turbulence variables $\widetilde{\nu}$ in the model were a zero gradient at the outlet, and an estimated value at the inlet.

The estimation was calculated using the relation $\nu_t = \sqrt{3/2} \cdot (C_\mu \cdot U_{ref} \cdot I \cdot l)$. This relation is found using the Prandtl-Kolmogorov relation $\nu_t = C_\mu \cdot \sqrt{k} \cdot l$ described in section 2.1 and inserting the estimation for k ($k = 3/2 \cdot (U_{ref} \cdot I)^2$) given in the OpenFOAM user guide [39]. $C_\mu = 0.09$ is a constant used in various turbulence models.

This estimated value was used both for the turbulent viscosity ν_t and for the transport variable $\tilde{\nu}$ described in section 2.1. For the reference velocity U_{ref}, the inlet velocity was used and for the length scale l, d_o was used. I describes the turbulent intensity and was inadvertently varied between the simulations. All the simulation did, however, have $I \lesssim 1$, which means the inlet is more or less laminar.

For all the wall boundary conditions, a wall function was used for ν_t and a fixed value of zero was used for $\tilde{\nu}$. The wall function used is based on Spaldings law and described in section 3.2.

Thermophysical properties: The thermophysical properties used for the full bundle domain are similar to the ones used in the one-row domain described in section 3.1. For the air side, all the thermophysical properties but the density is sat to a constant. The air is modelled as dry air. The constant values are, however, evaluated at the arithmetic mean of the inlet and tube wall temperature: $T = 1/2 \cdot (T_{in} + T_w)$. For density, the ideal gas law is used. The thermophysical properties needed to be specified were, the dynamic viscosity where $\mu = 2.07 \cdot 10^{-5}\ Pa \cdot S$ was used. The specific heat at constant pressure where $C_p = 1010\ J/(Kg \cdot K)$ was used, and the Prandtl number where $Pr = 0.7$ was used.

All of the simulations used the same thermophysical properties. However, the thermophysical properties for one of the simulations shown in section 4.1 should have been different, however, a mistake was made and this was run with the same thermophysical properties as the rest.

For the fins the same thermal conductivity of $K_{alu} = 193\ W/(mK)$ as in the one-row model is used.

Changes in the grid generation compared to the one-row model

Most of the changes in the full bundle model compared to the one-row model were in the grid generation. The grid generation for the full bundle simulations was performed on the computer provided by EPT, while most of the simulations were performed on the computer cluster IDUN/EPIC at NTNU.

OpenFOAM is distributed by two distributors. OpenFOAM v8, used for the one-row model, is distributed by *The OpenFOAM Foundation* [11]. In the grid generation for the full bundle simulations OpenFOAM v2012 was, however, found to be better. OpenFOAM v2012 is distributed by *OpenCFD Ltd* [38]. The reason for this was that the grid generation tool "snappyHexMesh" in OpenFOAM v2012 was found to be better suited for grids with a lot of regions. The actual simulations were, however, found to be easier to run in OpenFOAM v8. Some basic explanations of how snappyHexMesh works is given in the description of the one-row model in section 3.1, and a more in-depth description can be found in the OpenFOAM user guide [14].

Since two versions of OpenFOAM were used, the process from generating the grid to running the simulations became somewhat more complex than for the one-row simulations described in section 3.1. The process started by generating a cubic background grid using the tool "blockMesh". This had the same overall size as the simulation domain shown in Figure (28) with dimensions shown in Table (3). No boundary conditions were applied at this stage. The tool "snappyHexMesh" was then used to refine the mesh close to the finned-tube geometries by splitting the cubic cells into smaller cubic cells. The finned-tube geometries were all drawn in Blender v2.90 and saved as stl-files. These stl-files were then used as input to snappyHexMesh.

To be able to apply an adiabatic boundary condition at all the fin tips, these had to be separate boundaries. It was found that the easiest way to separate the fin-tip as an own boundary from the rest of the fin was to use the tool "createBaffels" at this stage of the grid generation. After separating the fin-tips, the grid generation was continued in "snappyHexMesh" by "snapping" the mesh to fit the finned-tube geometries and finally inserting layers near the finned-tube geometries.

Up till this point, OpenFOAM v2012 was used, but for the rest of the process, OpenFOAM v8 was utilised. To set the cyclic boundary conditions the tool "createPatch" was used. After this, the mesh was split into the air region and all of the fin and tube regions. Finally, the appropriate boundary conditions were applied to all the boundaries in all the regions using the tool "changeDictionary".

As can be seen in Figure (28), the simulation domain has half of the finned-tube on each side of a cyclic boundary for every other row. When splitting the mesh into the respective regions there were some initial problems with the half-fins and half-tubes on the cyclic boundaries. This is the reason the cyclic boundary conditions were applied after the grid generation, and not in the background grid like in the one-row model, as described in section 3.1.

The insertion of layers was also found to be problematic. If too many layers were inserted, problems arose both in computer memory in the grid generation, and in creating a mesh which would run. The reason for the mesh not running is believed to be the small cells in the mesh creating unknown behaviour when the initial values are set in the domain. That is to say cells where e.g. the thermophysical properties are non-positive and/or tending towards infinity.

Problems in the mesh also arose in the feature snapping process in snappyHexMesh. In the "feature snapping" the refined cubic cells are split to fit the geometries. A tolerance is given for how far the mid-point in a cell in the mesh can be from the geometry and still be attach to it. The smaller this tolerance, the less smooth the geometry representation is. This tolerance had to be kept fairly low in order for the mesh to not get distorted. A balance therefor had to be made between modelling the exact geometry and not doing this at the expense of a distorted mesh. It is worth mentioning that the refined cubic cells at the edge of the finned-tube geometries have side lengths of less than 0.1 mm. This means the representation without any feature snapping is relatively smooth in the first place.

A representative mesh is shown in Figure (29), this is taken from one of the full bundle simulations. What is shown, is a cut down the middle of the domain shown in Figure (28). This then shows the middle of the full finned-tube in the second row.

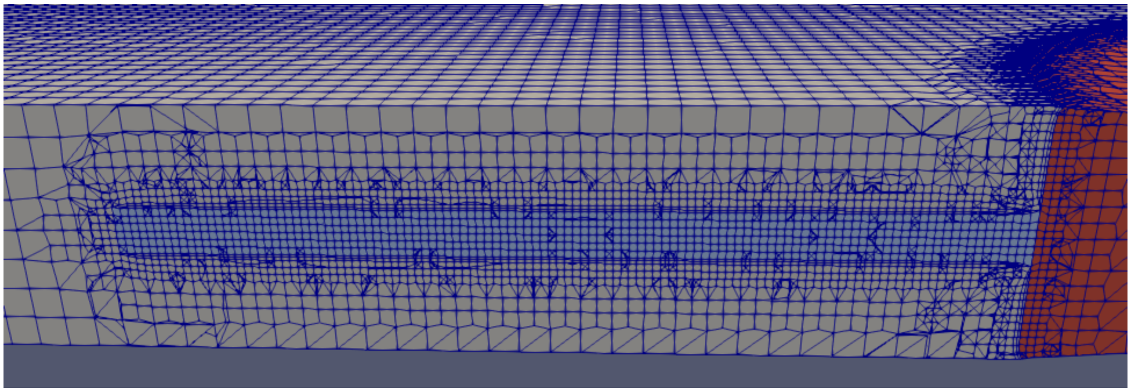

Figure 29: Representative mesh for the full bundle domain, the figure shows the domain in a plane cut down the middle of one of the full finned-tubes

As can be seen in Figure (29), the mesh has lots of small imperfections. These imperfections come from the "snapping" step of the grid generation and do seem inevitable when using the tool "snappyHexMesh". These are cells that have split for no apparent reason and do not sit flush with the plane. Instead, they have a pyramid shape going out of or inn to the plane. All the lines shown in Figure (29) then comes from seeing this in a plane. These imperfections also appear in the middle of the air region far away from the geometries, and again, for no apparent reason.

Figure (29) also shows the inserted layers close to the finned-tube and the refined cubic cells close to the finned-tube geometry. Layers are not inserted at the fin tips.

The problems described above with regards to generating a good grid has been a limiting factor in this thesis. This is something that should be kept in mind when reviewing the simulation results. Using a bad mesh as input to a simulation can in some cases dictate the quality of the simulation results. The problems with inserting layers have also been the limiting factor for how high the Reynolds number could be.

It is worth pointing out that the difficulties with running simulations with many layers only happened for the full bundle domain. Testing a one-row domain with half of the finned-tube on each side of the cyclic boundaries, this was not a problem. This indicate that this problem was not caused by having half of the finned-tube on each side of the cyclic boundaries. What caused the problems with adding layers for the full bundle domain is not clear.

3.5 Reduced domain full bundle

Simulating a full finned-tube bundle, as described in the section above, is computationally heavy. In an attempt to save computational time, a reduced domain was investigated. The reduced domain represents a cut-out of the full domain and is shown in Figure (30). The reduced domain has the same cyclic boundary conditions as the full domain shown in Figure (28), in addition to corrected cyclic boundary conditions in the streamwise direction.

The implementation methods tried out builds on the work of both Martinez et al. [43] and Lindqvist et al. [34]. The methodology used by Martinez et al. [43] originally stem from Patankar et al. [57] who proposed an implementation for a plate-fin heat exchanger in laminar flow. This implementation did not involve conjugate heat transfer (CHT) between the solid plates and the fluid.

An assumption is made that fully developed flow in a finned-tube bundle can be represented by a cyclic cell corrected for pressure drop and temperature loss.

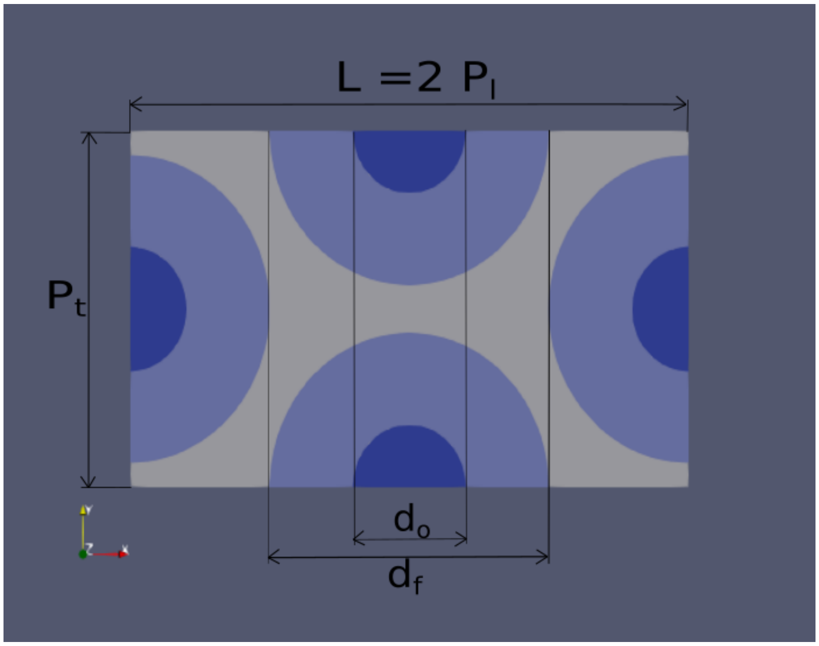

Figure 30: Reduced computational domain with cyclic boundary conditions in the streamwise direction. The flow direction is from left to right

Figure (30) shows the reduced domain. This is a cut-out with length L of the full domain shown in Figure (28). All other dimensions and parameters are the same as for the full domain shown in Figure (28) with dimensions given in Table (3).

In the work by Martinez et al. [43] the jumps in pressure and temperature are implemented as source terms in the RANS and energy equations, respectively. The source term β_L added to the RANS equations represents the pressure drop per domain length. During the simulation, the initial β_L is then multiplied with a correction factor based on the desired flow rate and the actual flow rate. This is then driving the flow through the domain, adjusting the velocity and pressure gradient to fit the desired flow rate.

The source term β_L was, however, not implemented in the reduced domain developed in this thesis. Instead, a simplification was made setting the density to a constant. This simplification made the desired average velocity at the inlet known. This velocity could then be imposed at the inlet of the cyclic domain through a pre-implemented source term in OpenFOAM. This source term then adjusted the velocity profile mapped from the outlet to the inlet of the cyclic domain to this average value. The constant density simplification was also used by Lindqvist et al. [34].

The source term added to the energy equation in the work by Martinez et al. [43], is a convection term of a scalar γ. γ represent the temperature gradient over the domain and was, in the work by Martinez et al. [43], defined as:

$$\gamma = \frac{\Delta T_L}{L} = \frac{\dot{Q}}{\dot{m} \cdot C_p \cdot L} \tag{27}$$

where ΔT_L is the temperature difference over the domain with length L, and $\dot{Q}$ is the heat duty. This gives γ the unit $[K/m]$.

This is the same as the term given by Patankar et al. [57] in an implementation valid for constant wall heat flux boundary conditions. Patankar et al. [57] then used γ in a source term in the energy equation for temperature.

In the work by Martinez et al [43], γ is, however, used in the energy equation for enthalpy $\widetilde{h}$, not temperature. This does not make consistent units. To get consistent units for implementation into the energy equation (see equation 25), γ was therefore redefined to γ_1:

$$\gamma_1 = \frac{\rho \cdot \dot{Q}}{\dot{m}} = \frac{\rho \cdot (h_{app} \cdot A_{tot}) \cdot \Delta T}{\dot{m}} \tag{28}$$

where h_{app} is the apparent or overall outside heat transfer coefficient, A_t the total outside heat transfer area and $\rho/\dot{m}$ is one over the volumetric flow rate ($\dot{V}$).

The scalar γ_1 can then be added to the energy equation (see equation (25)) as:

$$\frac{\partial U_i \gamma_1}{\partial x_i} \tag{29}$$

where U_i is the velocity in the i^{th} direction.

To calculate γ_1 the overall heat transfer coefficient has to be specified. This relies on empirical correlations for the Nusselt number and can be calculated into the apparent heat transfer coefficient using the procedure described in section 3.6 backwards. The last unknown is then the temperature difference ΔT. This was, in the work by Martinez et al. [43], calculated using ΔT_{LM}, also described in section 3.6. Exactly how the different temperatures were found in the work by Martinez et al. [43], is somewhat unclear, as a software with this term implemented was utilised.

In the original paper by Patankar et al. [57] the source term γ was multiplied with the velocity and inserted into the energy equation for temperature. It was then stated that this implementation is only valid for cases with constant wall heat flux boundary conditions. The other implementation given by Patankar et al. [57] was for a constant wall temperature and takes a very different form.

In the work by Lindqvist et al. [34], the temperature field was mapped from the outlet to the inlet of the cyclic domain and adjusted by a specific ΔT. Hence, this method does not need an implementation of a source term in the energy equation.

Implementation of the reduced domain model

For the implementation inspired by the work of Martinez et al. [43], a new OpenFOAM solver was programmed. The solver was based upon the existing solver "chtMultiRegionFoam" used for all the other simulations in this thesis. "chtMultiRegionFoam" is described in section 3.1. The new solver had the source term added to the energy equation for the fluid region (see equation (25)), with ΔT, T_w and a term $\gamma_1/\Delta T$ added as new input parameters possible to set at run-time.

The calculation of ΔT was done using the effectiveness-NTU method. The effectiveness-NTU method is collected from Incropera et al.[21]. For the case at hand, the temperature at the outside tube wall is set to a fixed value $T_w = 298$ K. This implies $\dot{m} \cdot C_p$ for the fluid inside the finned-tube (not modelled) is zero. In such cases the effectiveness ϵ_T, can be described as:

$$\epsilon_T = \frac{T_{in} - T_{out}}{T_{in} - T_w} = 1 - e^{-NTU} \tag{30}$$

where NTU is the number of heat transfer units, $NTU = \frac{(h_{app} \cdot A_{tot})}{\dot{m} \cdot C_p}$ [21].

A simulation was run at $Re_{do} \approx 5500$. The thermophysical properties for this simulation were the same as for the full bundle model described in section 3.4.

The resulting pressure drop over the middle row of the domain shown in Figure (30) was $Eu_{num} = 1.09$. This is an overprediction of around 30%, compared to the correlation by Holfeld [17] $Eu_{corr} = 0.84$ (see equation (23)). This is within the ±34% error band given by Holfeld [17] for this correlation. The pressure drop in the reduced domain model is governed by the imposed average velocity. This uses an already implemented source term in OpenFOAM. Hence, the solution is more likely to be correct since it eliminates the chance of implementation error.

The heat transfer from the simulation gave, on the other hand, a more varying result. Many different input ΔT were tested out. Simulations using both the ΔT from the effectiveness-NTU method directly as input, and simulation using ΔT_{LM} with various T_{in} values in combination with a sampled T_{out} were tried out.

One of these simulations used an input ΔT to the simulation calculated using the effectiveness-NTU method over the two last rows in the eight-row bundle shown in Figure (28). This gave a numerical result $Nu_{num} = 41.0$, which is fairly close to $Nu_{corr} = 37.0$ using the correlation for a full bundle by Holfeld [17] (see equation (20)).

This result was, however, calculated using a different ΔT_{res} than the input ΔT. The ΔT_{res} used in calculating the results is arithmetic mean of the sampled outlet temperature, and the inlet temperature calculated using the heat duty from the simulation result. Calculation of T_{in} uses equation (36) and the sampled outlet temperature. The reason ΔT_{res} was used in the results and not the input ΔT, is to have consistency between the resulting heat duty and the temperature difference.

It is worth pointing out that ΔT used as input in the simulation is way higher than the ΔT observed over the domain and ΔT_{res}. ΔT_{res} was small because the heat duty in all the simulations were small. This means the result is highly influenced by small changes.

During the simulation, the solution stabilised at a temperature higher than T_w, which it should, although a temperature gradient over the domain was not visible. The definition of γ_1 is a constant value over the domain. This means the source term is only a proportionality constant to the divergence of the velocity vector ($\frac{\partial U_i}{\partial x_i}$). From the solution for temperature (not shown), it looked like the cyclic domain had a small uniform heating keeping the temperature a little above T_w.

The simulations by Martinez et al. [43] used constant wall heat flux boundary conditions, but they did not discuss whether the method is extendable to CHT cases. It is therefore possible that the model they proposed only works for simulations with constant wall heat flux boundary conditions (as described by Patankar et al. [57]), and not for CHT simulations.

An implementation valid for CHT simulations was mentioned by Patankar et al. [57] and pointed out to be different. No instruction on how to do such an implementation was, however, given.

The method by Patankar et al. [57], although explicitly stated not to be valid for CHT cases, was also tried. This was done to check how it behaved for CHT cases and compare the result with result from the method by Martinez et al. [43]. The original method by Patankar et al. [57] uses a source term $U_i \cdot \gamma$, where U_i is the velocity in the i^{th} direction. For implementation into the energy equation (see equation (25)) this was redefined to $U_i \cdot \gamma_1 / L$.

The result of this simulation was similar to the result using the method by Martinez et al. [43], although with an even smaller value for the resulting heat duty for the same γ_1. This implies that the method by Martinez et al. [43] most likely is not valid for CHT simulations.

It is also worth mentioning that γ_1 is used instead of γ for the units to be consistent, whether γ_1 is correct, is not verified.

Some of the simulations used, as mentioned, a sampled T_{out}. For this, a sampling plane had to be implemented at the outlet. A code adapted from the postprocess function for a sampling plane was used. Even so, the two gave somewhat different answers. The reason for this fault in implementation is not clear, but most likely the C++ function names mean slightly different thing depending on which C++ header files and namespaces are included.

Implementation of the method described by Lindqvist et al. [34] is then more straightforward. No source term had to be added, and thus no new solver had to be programmed. Instead, some trick boundary conditions could be used, where a ΔT was added to the inlet of the cyclic domain.

For this implementation, cyclic boundary conditions in the streamwise direction were not initially used. Instead, the profiles for the different variables were manually mapped from the outlet to the inlet. From this, all but temperature, velocity and pressure acted as cyclic boundary conditions. The same pre-implemented velocity source term described above was used.

Initially, a fixed value for outlet temperature was used to test out the method. This was found to be unstable with regards to pressure, where the solver could not calculate the pressure for the first time-step.

A jump in temperature was also tried out. This required cyclic boundary conditions in the streamwise direction. A specific jump could then be set when the profile was mapped from the outlet to the inlet of the cyclic domain. This had similar stability issues as for a fixed value.

Since the methods were either unstable or the simulation results were very different to expected, implementation of a reduced domain was dropped. The reduced model using the method by Martinez et al.[43] was dropped because of all the inaccuracies described above. Further investigation into the implementation of the method described by Martinez et al. [43] should be done. If a different implementation is needed for CHT cases, this should also be investigated.

The method described by Lindqvist et al. [34] is then more straightforward. An implementation mapping and scaling the profiles from the outlet to the inlet is probably more physically correct. The stability issues led to the dropping of this model as well. Lindqvist et al. [34] used this model for CHT simulations, and further work into achieving an implementation of this model should be done.

3.6 Postprocessing

In this section, the data deduction or postprocessing of the simulation results is presented. Below are the procedures for calculation of the heat transfer and pressure drop valid for both the one-row and full bundle model. The postprocessing was done in MATLAB R2018b if nothing else is stated.

The outside tube diameter d_o is used as a length scale in the Reynolds number and the Nusselt number, this is the same length scale used by both Holfeld [17] and Lindqvist [33]. The Reynolds number Re_{do} is calculated in the minimum free-flow area A_{min}:

$$Re_{do} = \frac{U_{Amin} \cdot d_o}{\nu} = \frac{\dot{m} \cdot d_o}{A_{min} \cdot \mu} \tag{31}$$

where U_{Amin} is the average velocity in the minimum free-flow area, and $\dot{m}$ is the mass flow rate. The mass flow rate is calculated based on the inlet conditions, that is to say $\dot{m} = (\rho \cdot U \cdot A)_{in}$. These values are known at the simulation start.

Heat transfer

To evaluate the overall heat transfer result, the Nusselt number (Nu) is used. The Nusselt number is a non-dimensional heat transfer coefficient defined as:

$$Nu = \frac{h_o \cdot d_o}{\kappa} \tag{32}$$

where h_o is the outside heat transfer coefficient and κ is the thermal conductivity of air [17].

From the simulations the heat duty $\dot{Q}$ can be collected using the postprocessing tool "wallHeatFlux". The heat duty $\dot{Q}$ is defined as:

$$\dot{Q} = \int_{A_{tot}} q\text{"} dA \tag{33}$$

Where q" is the local heat flux and A_{tot} the total heat transfer area. The total heat transfer area consists of the fin area A_f and the tube area between the fins A_b.

All the simulations used a constant temperature at the outside of the tube wall $T_w = 298$ K. This means the apparent heat transfer coefficient h_{app} can be calculated using a heat balance for the total heat transfer area. h_{app} is here the same as the overall outside heat transfer coefficient.

Using formulas collected from Incropera et al. [21], the heat balance becomes:

$$h_{app} = \frac{\dot{Q}}{A_{tot} \cdot \Delta T_{LM}} \tag{34}$$

where ΔT_{LM} is the logarithmic mean temperature difference defined as:

$$\Delta T_{LM} = \frac{T_{in} - T_{out}}{\ln(T_{in} - T_w) - \ln(T_{out} - T_w)} \tag{35}$$

with T_{in} being the inlet temperature, and T_{out} being the outlet temperature.

To calculate the bulk temperatures the heat duty was used:

$$T_i = T_{in} - \frac{\sum_i \dot{Q}_i}{\dot{m} \cdot C_p} \tag{36}$$

where C_p is the specific heat at constant pressure. T_i is the temperature for row number i. For $i = N$, where N is the number of rows, $T_i = T_{out}$.

Using the apparent heat transfer coefficient, one can solve for the outside heat transfer coefficient h_o:

$$h_{app} \cdot A_{tot} = h_o \cdot [A_b + \eta_f \cdot A_f] \tag{37}$$

where η_f is the fin-efficiency.

Equation (37) has to be solved iteratively since η_f is a function of h_o. Values for η_f in the iterations can be calculated from equation (38). When the iterative procedure has converged, h_o can be inserted into equation (32) for the Nusselt number.

The fin efficiency is a parameter used to calculate the heat transfer from extended surfaces like fins. Heat has to be conducted through the fin. Since the fin has a finite thermal conductivity, a temperature gradient will form in the radial direction. The fin efficiency is then a parameter accounting for the lower heat transfer caused by the temperature gradient. η_f is defined as the ratio of the actual heat transfer to the ideal heat transfer from the fin. The ideal heat transfer from the fin is the heat transfer with an infinite thermal conductivity, that is say no temperature gradient. [17, 69]

A differential equation for the heat conduction can be set up to solve for the temperature gradient in the fin. Gardner (1945) solved this equation for annular finned-tubes, proposing a theoretical solution. This solution involves modified Bessel-functions[17]. The equation and the solution by Gardner (1945) can be found in Incropera et al. [21].

To avoid using Bessel-functions, simpler solutions using curve fitting of the Gardner (1945) solution has been proposed. The solution used to calculate the fin efficiency in this thesis was proposed by Schmidt (1945). The solution by Schmidt (1945) is taken from Klynderud [69]. This uses the simpler theoretical solution for the fin efficiency of rectangular fins:

$$\eta_f = \frac{\tanh(m \cdot \phi)}{m \cdot \phi} \tag{38}$$

along with a modified fin height ϕ, which is defined as:

$$\phi = h_f \cdot \left[1 + 0.35 \cdot \ln\left(\frac{d_f}{d_o}\right)\right] \tag{39}$$

The parameter m is defined as m= $\sqrt{\frac{2 \cdot h_o}{\kappa_{alu} \cdot t}}$, where κ_{alu} is the thermal conductivity of aluminium and t is the fin thickness [69].

The local heat transfer coefficient over the fin was calculated as

$$h_{loc} = \frac{q''}{\Delta T} = \frac{q''}{T_f - T_{ref}} \tag{40}$$

where T_f is the local fin temperature and T_{ref} is a reference temperature set to the arithmetic mean air temperature (T_m) over the fin. h_{loc} can then be used instead of h_o in equation (32) to obtain the local Nusselt number. This calculation was done in ParaView 5.6.0.

Pressure drop

To evaluate the overall pressure drop, the Euler number (Eu) is used. Eu is a non-dimensional pressure drop coefficient defined as:

$$Eu = \frac{2 \cdot \Delta P}{\rho U^2_{(Amin)} N} \tag{41}$$

where ΔP is the pressure drop over N rows. Since the density is not constant, U_{Amin} varies through the bundle. The U_{Amin} used in equation (41) is calculated from continuity using the density at the arithmetic mean of the temperature over the domain: $T_m = 0.5 \cdot (T_{in} + T_{out})$. This gives $\dot{m} = \bar{\rho} \cdot A_{min} \cdot U_{Amin}$.

Since the density is not constant, the method by Kays and London [24] was used to account for the pressure drop due to flow acceleration:

$$\Delta P_a = \frac{G^2}{2 \cdot \rho_{in}} \cdot \left(1 + \sigma^2\right) \cdot \left(\frac{\rho_{in}}{\rho_{out}} - 1\right) \tag{42}$$

where σ is an area ratio: $\sigma = \frac{A_{min}}{A_{in}}$ and G is the mass velocity in the smallest free flow area: $G = \dot{m}/A_{min}$. The subscript in and out corresponds to the inlet and outlet.

Unlike for the heat transfer, the pressure was collected from a mass averaged sampling plane inserted in front of the first tube row and behind the last. The method can, however, be used for the row-by-row Nu calculations, inserting the plane before and after the row in question. To keep the temperature difference consistent with the heat duty, this was not used.

4 Results and Discussion

In this section, the results for the full bundle simulations are presented and discussed. Firstly, the results from the simulations performed using the eight-row domain shown in Figure (28) with dimensions shown in Table (3) are presented. These are used, in part, to validate the full bundle model, but also to investigate the row-by-row heat transfer coefficient. These results were intended to be used as a starting point for the investigation into geometry changes of the finned-tubes and finned-tube bundles. However, some mistakes were made, making the results less useful and inapt for this.

The second part is a presentation of the simulation results with different changes in the geometry of the finned-tubes and finned-tube bundles. The results are then discussed and compared with the literature presented in section 2.4.

The results for the one-row model are used in section 3.2 to investigate y_p^+ and in section 3.3 to investigate turbulence models and are presented and discussed in these sections.

4.1 Row-by-row heat transfer

In this section, the row-by-row development of the heat transfer coefficient for the initial full eight-row finned-tube bundle is presented. The heat transfer coefficient is calculated as described in section 3.6. The results were intended to be used as validation of the full bundle model and in deciding how many rows constitutes a full bundle. However, these simulations had an error in the CAD drawings of the bundle, and hence in the mesh, where every other row were shifted 1 mm towards the outlet. For this reason, Re_{do} is not constant through the bundles but oscillates $\pm 2\%$. This difference is relatively small. However, results in section 4.2 indicate that the error in the overall heat transfer coefficient is significant. If this is only due to the shift in the geometry, is unclear.

How much the shift has influenced the row-by-row heat transfer coefficient is not clear. The trends are, however, believed to be the same as for the correct geometry, although some extra oscillations in the heat transfer coefficient between the rows might be present.

Three simulations using the full eight-row bundle shown in Figure (28) were run. Initially a simulation at $Re_{do} \approx 1100$ with $T_{in} = 398$ K was performed. This used the thermophysical properties described in section 3.4.

For this simulation, it was found that the difference in temperature between row five and row eight was only around 1 K, with an equally small resulting heat duty. This means the heat transfer result for these rows is highly sensitive to small numerical errors. To challenge this result, a simulation at a similar Reynolds number and a higher inlet temperature $T_{in} = 500$ K was also performed. This simulation did, however, have a Reynolds number $Re_{do} \approx 1600$ due to a mistake made, not updating the thermophysical properties to match the higher inlet temperature.

Lastly, a simulation at a moderate Reynolds number $Re_{do} \approx 5500$ was conducted, this used the same inlet temperature as the first simulation (i.e. $T_{in} = 398$ K). It is worth pointing out that this simulation was run at an inlet turbulent intensity $I \approx 0.2\%$ inadvertently, the two others were run at $I \approx 1\%$. The simplification of using an adiabatic fin-tip was used in all the simulations.

The row-by-row Nusselt number results from the three simulations along with some results from the literature are shown in Figure (31). The results are divided by an average Nu to have the same scale. The results from the literature used for comparison are experimental results by Klynderud [69] and Holfeld [17], and a numerical result by Lindqvist et al. [36]. The experimental result by Klynderud [69] corresponds to "Test 1" with low mass flow in the thesis by Klynderud [69]. The results by Holfeld [17] and Lindqvist et al. [36] corresponds to their respective lowest Reynolds number row-by-row result.

These results were, as described in section 2.3, chosen mostly due to the data from the studies being available, either through values given for the results or through clear graphs. These results are also for an eight-row bundle, as seen in Figure (31).

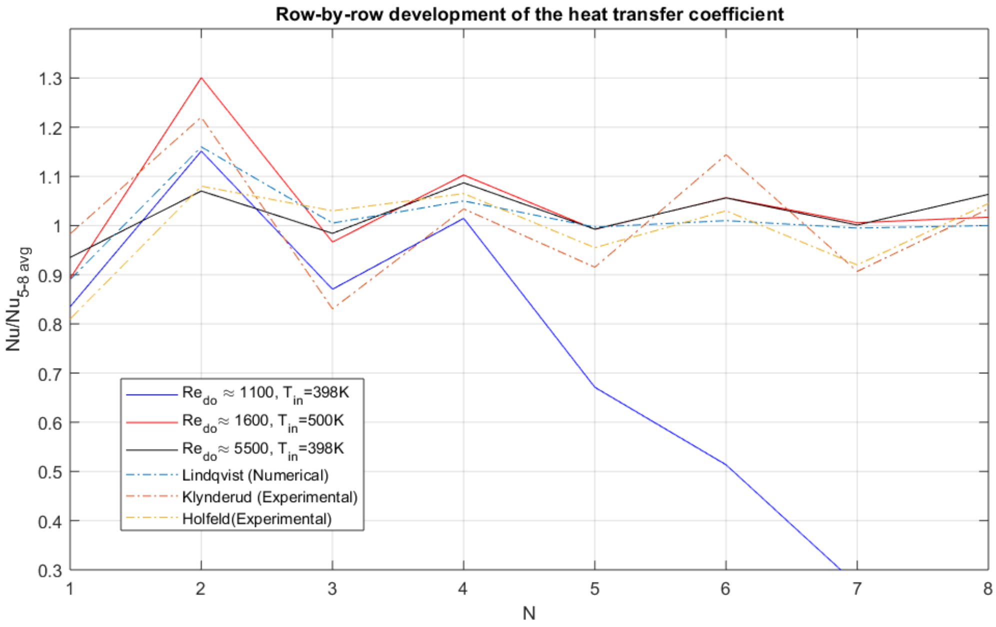

Figure 31: The row-by-row Nu development of the three simulations conducted using an eight-row finned-tube bundle

As can be seen from Figure (31), the simulation at $Re_{do} \approx 5500$ (black in Figure (31)) and the simulation with a higher T_{in} (red in Figure 31) behaved similarly to what is described in section 2.3. Large oscillations for the first rows, then smaller oscillations stabilising more towards a constant value for Nu. The lowest heat transfer coefficient is also found in the first row in these two simulations.

For the simulation with a higher T_{in} (red in Figure 31), the highest heat transfer coefficient is found in the second row, as one expects from the literature described in section 2.3. This simulation follows a similar trend to the numerical result by Lindqvist et al. [36], although the oscillations in Nu between the rows are larger than in the result by Lindqvist et al. [36], as can be seen in Figure (31). Whether this is caused by the shift in the geometry is not clear. However, as can be seen in Figure (31), the experimental result by Klynderud [69] has similar oscillations in Nu between the rows. This experimental result also has an unexpected peak in Nu at the sixth row. For the simulation result with a higher T_{in}, however, most of the change happens before the third row, and from row five onwards Nu is close to constant, as can be seen in Figure (31).

For the simulation at $Re_{do} \approx 5500$ (black in Figure (31)), there is an unexpected peak in Nu at the fourth row, and the maximum value for Nu is found here. Both this peak at the fourth row and the, lower than expected, value for the second row fits with the flow acceleration and deceleration due to the shift in the geometry. Whether this shift is responsible for the behaviour, is unclear. The oscillations in Nu for the simulation at $Re_{do} \approx 5500$ do, as seen in Figure (31), become somewhat smaller from the fifth row onwards, even though they do not vanish. Similar oscillations in Nu through the whole bundle are also found in the experimental result by Holfeld [17], as can be seen in Figure (31). However, as described in section 2.3, Holfeld [17] argued that error in measurements could be the reason for the behaviour of the experimental results being different than expected. Both Klynderud [69] and Holfeld [17] used the same experimental setup which means the same errors can be present.

For the simulation at $Re_{do} \approx 1100$ (blue in Figure (31)), a somewhat different behaviour than all the other results is visible from row four onwards. To keep the scaling of this result similar to the others shown in Figure (31), the result for the fourth row was used for scaling instead of the average of rows five to eight.

The reason for the drop off in Nu from row four is believed to be a numerical error. The most likely reason is, as mentioned, a small ΔT between the last rows. Due to the magnitude of the heat duty for these last rows being very small, the result becomes highly sensitive to small errors. The mass flow rate for this simulation was checked using a sampling plane inserted in front of the first row. This revealed that the sampled mass flow rate was 1.6% lower than the mass flow rate calculated from initial values. If this sampled mass flow rate was used to calculate the temperatures going into ΔT_{LM}, as described in section 3.6, the row-by-row decrease seen for the simulation at $Re_{do} \approx 1100$ in Figure (31), changes to an increase.

Calculating the row-by-row Nu for the two other simulations ($Re_{do} \approx 1600$ and $Re_{do} \approx 5500$) using the sampled mass flow rate at the inlet, gives a slight decrease at the end for the simulation result at $Re_{do} \approx 1600$ and no visible change to the result of the simulation at $Re_{do} \approx 5500$.

The fact that the simulation result at $Re_{do} \approx 1600$ with $T_{in} = 500$ K behaves as expected, also underlines that the drop off in Nu (seen in Figure (31)) for the result at $Re_{do} \approx 1100$ is a numerical error. In the simulation with a higher T_{in}, the heat duties for the last rows and the temperature differences between the last rows are higher. This means the result is less sensitive to small numerical errors.

The results of the overall Nu and Eu for these three simulations are shown in Figures (32b) and (32a). Nu and Eu are calculated as described in section 3.6.

The heat transfer correlations used for comparison with the simulation results are from VDI (see equation (19) in section 2.5) and from PFR (see equation (18) in section 2.5), both taken from Holfeld [17]. The error band used for the correlation from PFR is ±31% and is taken from Holfeld [17]. The correlation from VDI comes with a specified ±25% maximum deviation, according to Mon [48].

The pressure drop correlations used for comparison with the simulation results are by Holfeld [17] (see equation (23) in section 2.5) and by Ward et al. [72] (see equation (22) in section 2.5). The correlation by Holfeld [17] has a ±34% error band, according to Holfeld [17], and the correlation by Ward et al. [72] has a $+26\%/-31\%$ error band, according to Ward et al. [72].

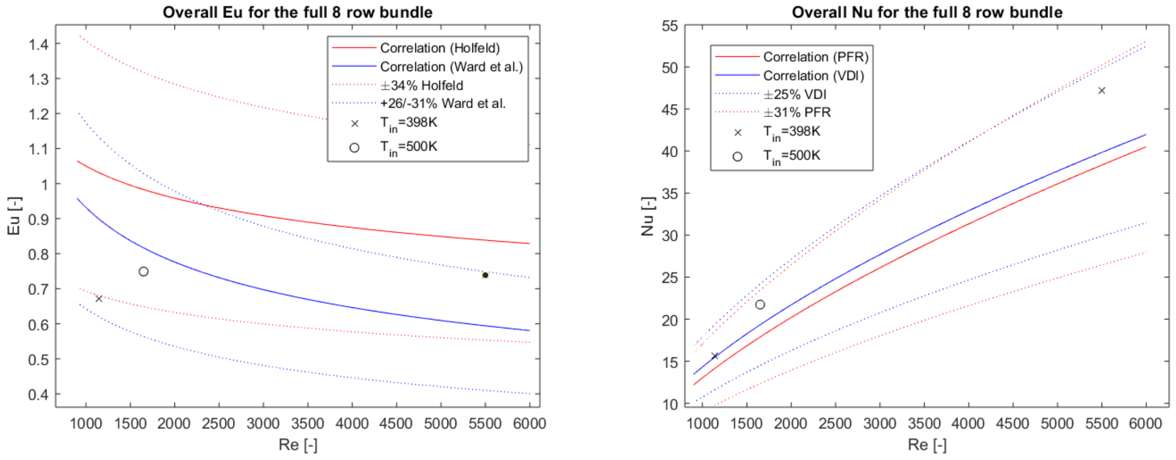

(a) (b)

Figure 32: Overall Eu (a) alongside the correlations by Ward and Young and by Holfeld, and overall Nu (b) alongside the correlations from VDI and PFR

As can be seen from Figure (32b), the simulation results for Nu overpredicts the correlation by VDI for the simulations at $Re_{do} \approx 1600$ and $Re_{do} \approx 5500$. This overprediction increases with increasing Reynolds numbers and the two results overpredict the VDI correlation by 12% and 18% respectively. All the results overpredict the correlation by PFR. All the results are, however, within the error band for both the correlations, as can be seen in Figure (32b).

It is worth pointing out that the Reynolds number is calculated in the non-shifted A_{min}, which is the average of the A_{min} in the rows where the flow is accelerated and decelerated. Using the A_{min} from the rows where the flow is accelerated, the Reynolds number would be somewhat higher, and the overprediction of the correlations less.

For the pressure drop seen in Figure (32a), the results are a little more varied. The two correlations also vary significantly from each other, as seen in Figure (32a). Only the result for the simulation at $Re_{do} \approx 1600$ are within the error band of both the correlations. For the simulation at $Re_{do} \approx 5500$, the result is between the two correlations and slightly outside the error band for the correlation by Ward et al. [72], as can be seen in Figure (32a).

In the simulation at $Re_{do} \approx 1100$, the pressure was found to be fluctuating quite significantly in front and behind the bundle. Sampling planes were inserted into the bundle to investigate the pressure drop development through the bundle and find a representative value for the overall pressure drop. The result for the overall Eu of the simulation at $Re_{do} \approx 1100$ shown in Figure (32a), should be representable, although a higher error can be expected.

Since the row-by-row heat transfer behaviour for this simulation (seen in Figure (31)) also is believed to be wrong, this simulation can be disregarded.

Due to the problems in generating a good grid for these simulations, as described in section 3.4, the value of y_p^+ became higher than wanted. For the simulation at $Re_{do} \approx 5500$, the maximum value was $y_p^+ = 4.3$. The two other simulations had lower maximum y_p^+ values.

In the y^+-investigation in section 3.2 it was found that y_p^+ should be kept below two, with higher values leading to an increase in Nu. An indication that this might be the case for the simulation at $Re_{do} \approx 5500$ was found in the next section. Here, a new simulation with five rows and the shift in geometry corrected was conducted. This had a result for Nu which was 26% lower than the result shown in Figure (32b). For Eu, the new result was 7% higher, matching the correlation by Holfeld [17] as shown in Figure (35a). The new five-row simulation and the differences compared to the eight-row simulation are further described in section 4.2.

Some difficulties in postprocessing also became evident in postprocessing the simulation results in this section. The (mass flow average) sampling plane postprocessing tool in OpenFOAM did not seem to give a consistent and accurate answer. A slight movement of the sampling plane changed the result in some cases significantly. For this reason, postprocessing using results from a sampling plane was kept to a minimum. The bulk temperatures were, for this reason, calculated from the heat duty using equation (36) in section 3.6. The exception where sampling planes are used, is the calculation of the pressure drop, as described in section 3.6.

Due to the shift in the geometry of every other row, a sampling plane could not be inserted between the rows without touching the fins. For this reason, the row-by-row pressure drop was not investigated, only the overall Eu.

4.2 Geometrical parameters

In this section the results for changes in the geometry of the finned-tubes and finned-tube bundles are presented.

In section 4.1, the simulation results using the eight-row simulation domain were presented. These were, as mentioned, intended to be used to decide the number of rows necessary to model in this section. The runtime of these simulations, did, however, supersede available time. For this reason, the decision of how many rows to model was made from preliminary, non-converged results and findings in the literature described in section 2.3.

From this, it was decided to continue with only five rows instead of eight. It is difficult to judge whether this decision can be justified, as the row-by-row results, described in section 4.1, behaved differently than expected. Part of this, as described in section 4.1, can be down to the shift in the geometry of every other row. The row-by-row result at $Re_{do} \approx 5500$ shown in Figure (31) does show less change in the row-by-row heat transfer coefficient from the fifth row onwards. This does not prove that the decision of going forward with five rows is correct but indicates that the error of doing so should be relatively small. However, further research into the row dependency of the heat transfer coefficient is needed.

The simulations in this section were run at $Re \approx 5500$, that is to say, the same as the highest Reynolds number simulation in section 4.1. For all but one of the simulations, the Reynolds number $Re_{do} \approx 5500$ is calculated in the minimum free-flow area, as defined in equation (31). The simulations used the same thermophysical properties as the other full bundle simulations, as described in section 3.4.

Prescribed inlet turbulence I was lower than 1% for the $Re_{do} \approx 5500$ row-by-row simulation in section 4.1. To keep the comparison as similar as possible, this was kept in all the simulations with different geometries. This means $I \approx 0.2\%$ was used instead of $I \approx 1\%$ at the inlet for all the simulations in this section. Numerical results by Lindqvist et al. [36] show that this should only influence the heat transfer coefficient for the first row.

A new simulation at $Re_{do} = 5500$ using a five-row version of the initial geometry shown in Figure (28) was run. This was to have a better comparison for the simulation results with geometry changes, both to correct the shift in the eight-row geometry and to have the same number of rows.

As described in section 4.1, the result for the overall Nu for this five-row simulation was around 26% lower than the overall Nu for the eight-row simulation. For Eu, the result for the five-row simulation was around 7% higher. The difference in the results for Nu was much higher than expected and much more than expected due to the shift in the geometry for the eight-row simulation. All the rows in the eight-row simulation had a higher heat duty, even though both simulations had the same inlet conditions and same thermophysical properties.

There do, however, seem to be a difference in the mesh quality. For the five-row simulation, the maximum y_p^+ for the heat transfer area was $y_p^+ = 2.6$. For the eight-row simulation, this value was $y_p^+ = 4.3$, as described in section 4.1. This means the five-row simulation is much closer to the recommended maximum y_p^+ value of around two found in the y^+ investigation in section 3.2. It is, however, possible either one of the two simulations has other undiscovered issues.

To test if the error came from a mistake in the postprocessing, the heat duties and temperatures for the first five rows in the eight-row bundle were copied into the postprocessing for the five-row bundle. This gave an answer within 1% of the answer for the eight-row bundle shown in Figure (32b) in section 4.1. This indicates that the error is not in the postprocessing. If the eight-row simulation can be trusted, this also indicates that reducing the domain down to five rows, do not influence the overall answer.

As for the overall heat transfer coefficient and pressure drop of the five-row simulation, they are compared with the correlations by Holfeld [17] in the comparison of different fin pitches below. Both the results are within the uncertainty range given by Holfeld [17] for the correlations, as seen in Figure (35). The result for Nu in the five-row simulation is also within the uncertainty range of the correlations in Figure (32b) showing the results for the eight-row simulations.

The five-row simulation is used as a starting point to investigate changes in the geometry, and the changes are compared relative to this simulation. The meshes for the five-row simulation and the simulations with changed geometries are made as similar as possible. The hope for this being that the qualitative trends and relative results between the changes would be representative. However, the grids for two of the simulations ended up with significantly higher values for y_p^+.

The geometry changes investigated are in the fin tip clearance, in the fin pitch and in the layout. The differences are compared in terms of the overall pressure drop and overall heat transfer. The distribution of the heat transfer coefficient over the fins in the second and fourth row are also compared. As described in section 3.6, a reference temperature is needed to calculate the local heat transfer coefficient. For this, the arithmetic mean of the bulk air temperature in front and behind the given fin is used. This makes the scale of Nu vary a lot between the different simulations, and between the second and fourth row. For this reason, the distribution of Nu can only be compared qualitatively between the simulations, not quantitatively.

The angle θ, defined in Figure (2) in section 2.2, is used to describe the local behaviour of the heat transfer coefficient. θ is defined as the angle from the inflow.

The row-by-row heat transfer coefficient for all the simulations in this section is shown in appendix C.

Fin tip clearance

Simulations with three different fin tip clearances were performed. The simulated finned-tube bundles all had a layout of $\beta = 30°$. The fin tip clearances investigated were $C_f = 0$, $C_f = 5.2$ mm and $C_f = 10.4$ mm, where $C_f = 5.2$ mm was the initial five-row simulation. The dimensions used in this initial simulation are described in section 3.4. Changing C_f also changes the transverse and longitudinal pitch, the fin tip clearances and the pitches for the three simulations are shown in Table (4).

Table 4: Dimensions relating to the bundles used for the different simulated fin tip clearances

Fin tip clearances (C_f) [mm]	Longitudinal pitch (P_t) [mm]	Transverse pitch (P_l) [mm]
0	33.5	29
5.2	38.7	33.5
10.4	43.9	38

The results are compared with experimental results by Holfeld [17]. These experimental results are from an investigation using an eight-row finned-tube bundle with serrated fins. The fin tip clearances tested by Holfeld [17] were $C_f = 0$, $C_f = 5$ mm and $C_f = 10$ mm. Holfeld [17] also did experiments with the initial full bundle with $C_f = 5.2$ mm modelled in this thesis. The results by Holfeld [17] at $Re_{do} = 5500$ for the serrated finned-tube bundle with $C_f = 5$ mm are around 15% higher for Nu and 250% higher for Eu compared with the results by Holfeld [17] for the geometry modelled in this thesis. This means the results by Holfeld [17] can only be used to compare trends. It is also worth mentioning that the results by Holfeld [17] are interpolated to $Re_{do} = 5500$ in order to match the Reynolds number used in the simulations.

The results for the simulations with different fin tip clearances are shown in Figure (33).

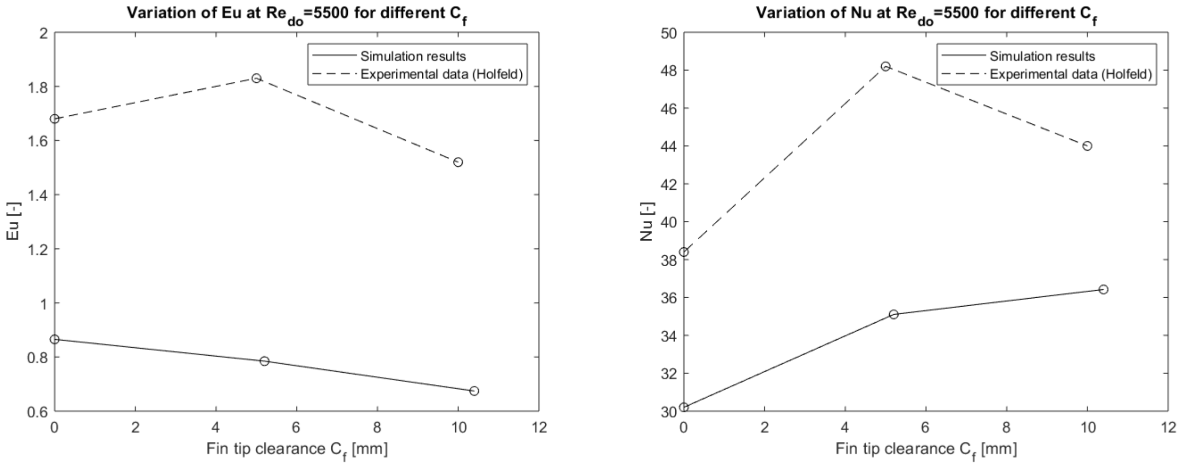

(a)

(b)

Figure 33: Overall Eu (a) and overall Nu (b) for different fin tip clearances compared with experimental results by Holfeld [17]

As can be seen in Figure (33b) for Nu, the simulation results follow the same trend as the results by Holfeld [17] going from $C_f = 5.2$ mm down to where the fins are touching ($C_f = 0$). In the simulation results, there is a decrease of around 14% for this change in C_f. In the experimental results by Holfeld [17], this decrease is around 20%. The only experimental study found investigating a fin tip clearance of $C_f = 0$ is by Holfeld [17], as described in section 2.4. So based on the study by Holfeld [17], the simulation results are as expected. If the fact that Holfeld [17] studied a different type of fins influences the trend as C_f goes to zero, is not investigated, and more research is needed.

In the simulation results going from $C_f = 5.2$ mm to $C_f = 10.4$ mm there is a small increase in Nu, as can be seen in Figure (33b). Here the simulation results do not follow the results by Holfeld [17]. However, as described in section 2.4, the results by Ma et al. [40] showed a small increase in Nu as C_f increases, while the results by e.g., Ward et al. [72] showed negligible effect on the heat transfer coefficient when changing C_f.

For the pressure drop, the simulation results show a steady decrease in Eu as C_f increases, as can be seen in Figure (33a). Going from $C_f = 5.2$ mm to $C_f = 10.4$ mm there is a decrease in Eu of around 14% in the simulation results. Here the simulation results follow the results by Holfeld [17], which has a decrease in Eu of around 17%. The decrease in Eu as C_f increases found in the simulation results is also in accordance with all the other studies described in section 2.4.

Going from $C_f = 5.2$ mm to $C_f = 0$, the simulation results do not follow the same trend as the results by Holfeld [17], as seen in Figure (33a). The simulation results show an increase in Eu of around 10%, while the results by Holfeld [17] show a decrease of around 8%. It is worth pointing out that Holfeld [17] calculated an uncertainty in measurements of Eu of up to 25% for $Re_{do} \approx 5500$. This makes it hard to evaluate if the simulation results show the correct trend, with further research being needed.

The distribution of Nu over the fins at different fin tip clearances is shown in Figure (34).

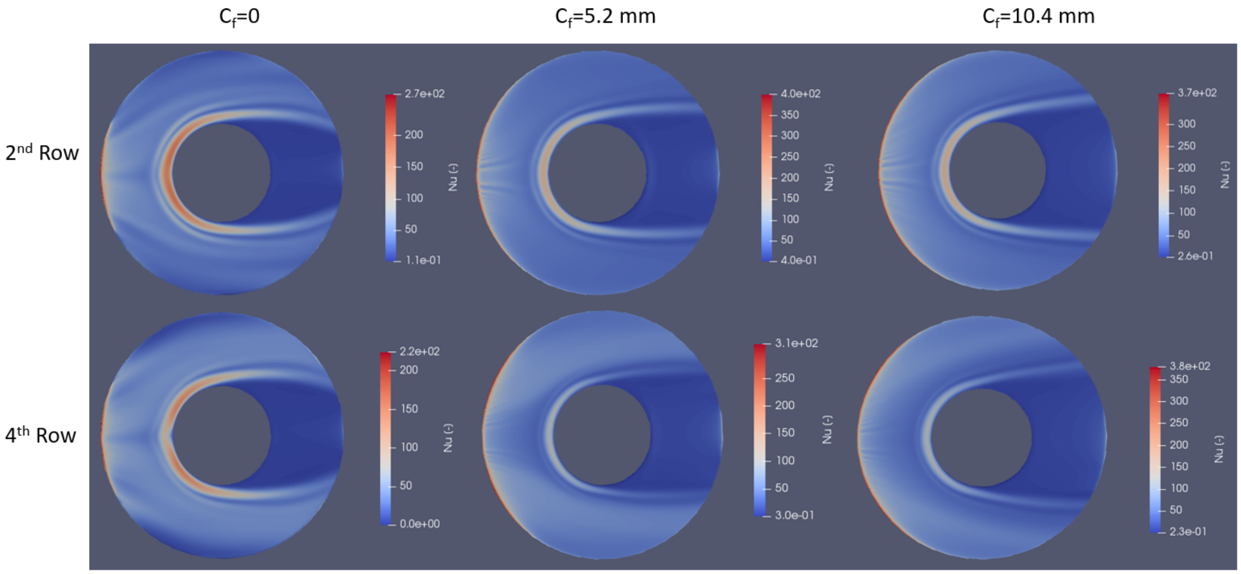

Figure 34: Distribution of Nu for the different fin tip clearances at the second and fourth row

As C_f increases, the increase in heat transfer at the leading edge of the fin due to flow impingement goes up to a larger θ, as seen in Figure (34). This is as expected, as less of the fin is in the wake of the preceding row. The effect the wake of the preceding row has on the heat transfer is also visible for the fin tips at $\pm 45° \lesssim \theta \lesssim \pm 110°$ for $C_f = 0$, where Nu is much lower. This is most visible for the fourth row, as seen in Figure (34). This influence of the wake of the preceding row is believed to be the reason the overall Nu is lower for $C_f = 0$ than $C_f = 5.2$ mm, as seen in Figure (33b).

As C_f increases the angle θ where the legs of the horseshoe vortices leave the fin decreases, as seen in Figure (34). This is a phenomenon not described in the literature but is probably the influence of the next row. For a small C_f the flow leaving the fin must change direction due to the tubes in the next row. However, as C_f increases, the bypass flow between the finned-tubes increases and the next tube row do not influence where the legs of the horseshoe vortices leave the fins.

This increase in the bypass flow is a phenomenon that should decrease Nu going from $C_f = 5.2$ mm to $C_f = 10.4$ mm. However, as seen in Figure (33b), the heat transfer coefficient increases going from $C_f = 5.2$ mm to $C_f = 10.4$ mm.

Comparing the distribution of Nu at the fourth row in front of the tube, the area of lower heat transfer seems to be smaller for $C_f = 10.4$ mm than for $C_f = 5.2$ mm.

This indicates that the jet-like flow hitting the fourth row is more pronounced for $C_f = 10.4$ mm. This is also reflected in the row-by-row heat transfer coefficient, seen in Figure (C.1) in appendix C. Here Nu for the three first rows are more or less the same for $C_f = 5.2$ mm and $C_f = 10.4$ mm, but for the fourth and fifth row, Nu is higher for $C_f = 10.4$ mm.

From this, it looks like there are two effects working against each other. Firstly, an increase in the bypass flow as C_f increases due to the flow taking the path of least resistance lowering Nu. This is also indicated by the decrease in Eu as C_f increases, as seen in Figure (33a). Secondly, the accelerated bypass flow results in a more jet-like flow impinging the edge of the fins increasing Nu. This is, however, only speculations based on two simulation results at a moderate Reynolds number, and further research is needed to understand this behaviour.

Comparing the second and the fourth row in Figure (34), the general trend seems to be a somewhat more evenly distributed heat transfer coefficient for the fourth row. This is as expected.

A mistake was made in the simulation with $Cf = 0$. The simulation used the wrong boundary condition for the temperature at the base of the fin for the second and fourth row. This was done because some of the boundaries were given different names when the mesh was split into the different regions. This splitting process is described in section 3.4. Why this happened, is unclear. The same error was found in the simulation with a $\beta = 45°$ layout described later in this section.

The mistake was, however, fixed halfway through the simulation. A new simulation investigating what influence, if any, this had on the solution was not conducted. It is, therefore, possible that the distribution for the heat transfer coefficient for $C_f = 0$ shown in Figure (34) is wrong. It might also have influenced the result for the overall heat transfer coefficient, shown in Figure (33b) and the result for the row-by-row heat transfer coefficient shown in appendix C. A new simulation with $C_f = 0$ should therefore be conducted.

Fin pitch

Simulations with three different fin pitches were conducted. All the simulated bundles had a $\beta = 30°$ layout. The fin pitches investigated were $S = 1.4$ mm, $S = 2.81$ mm and $S = 5.62$ mm, with $S = 2.81$ mm being the initial five-row simulation. The dimensions of this initial bundle are described in section 3.4. The simulations with $S = 1.4$ mm and $S = 5.62$ mm has the same dimensions as the simulation with $S = 2.81$ mm, apart from the changed fin pitch.

The correlations by Holfeld [17] (see equation (20) and (23) in section 2.5) are used as a comparison for the simulation results.

The results for the overall Eu and Nu at different fin pitches are shown in Figure (35).

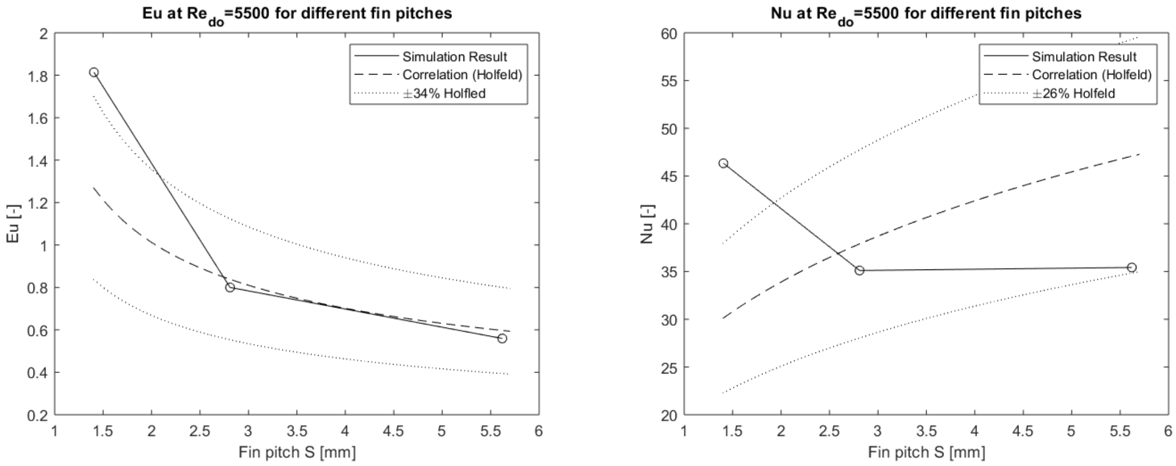

(a) (b)

Figure 35: Overall Eu (a) and overall Nu (b) for different fin pitches compared with correlations by Holfeld [17]

For Nu, the simulation results follow a different trend to the correlation by Holfeld [17], as seen in Figure (35b). The simulation results show the heat transfer to be independent of the fin pitch going from $S = 2.81$ mm to $S = 5.62$ mm, with the results being within 1% of each other. The correlation by Holfeld [17] shows the heat transfer to increase as the fin pitch increases, as seen in Figure (35b). It is, however, worth pointing out that the experimental results by Holfeld [17] show the heat transfer to be more or less independent of the fin pitch, as described in section 2.4. Both of these simulation results are also within the ±26% error band given by Holfeld [17] for the Nu correlation, as seen in Figure (35b). A negligible effect on Nu changing the fin pitch, as is found in the simulation results, also agrees with all of the other experimental studies described in section 2.4.

In the simulation results going from $S = 2.81$ mm to $S = 1.4$ mm, there is an increase in Nu of around 32%, as seen in Figure (35b). This is the opposite trend to the correlation by Holfeld [17]. It is, however, worth pointing out that this is a much smaller fin pitch than tested by Holfeld [17], and beyond where the correlation is valid. A study found investigating such a small fin pitch, is the numerical study by Lindqvist et al. [36]. These simulation results by Lindqvist et al. [35] are for the same geometry modelled in this thesis, and are shown in Figure (17) in section 2.4. The simulation results by Lindqvist et al. [36] show a similar trend to the simulation results shown in Figure (35b). The results by Lindqvist et al. [36] also show a drop off in Nu at fin pitches lower than tested here.

For the pressure drop, the simulation results follow the correlation by Holfeld [17] remarkably well, as seen in Figure (35a). For the two largest fin pitches ($S = 2.81$ mm and $S = 5.62$ mm) the simulation results are within 7% of the correlation. This is well within the ±34% error band given by Holfeld [17] for this correlation. For $S = 1.4$ mm, the simulation results overpredict the correlation by 43%. This is, again beyond where the correlation by Holfeld [17] is valid. The simulation results by Lindqvist et al. [36] (see Figure (17) in section 2.4) has the same trend as the simulation result shown in Figure (35a). This trend where Eu decreases as the fin pitch increases is also in accordance with all the studies presented in section 2.4.

The results are also intuitively as expected. As S decreases, the surface area increases, increasing the friction surface and thus increasing the pressure drop, as explained by Holfeld [17].

The distribution of Nu over the fins for the different fin pitches is shown in Figure (36)

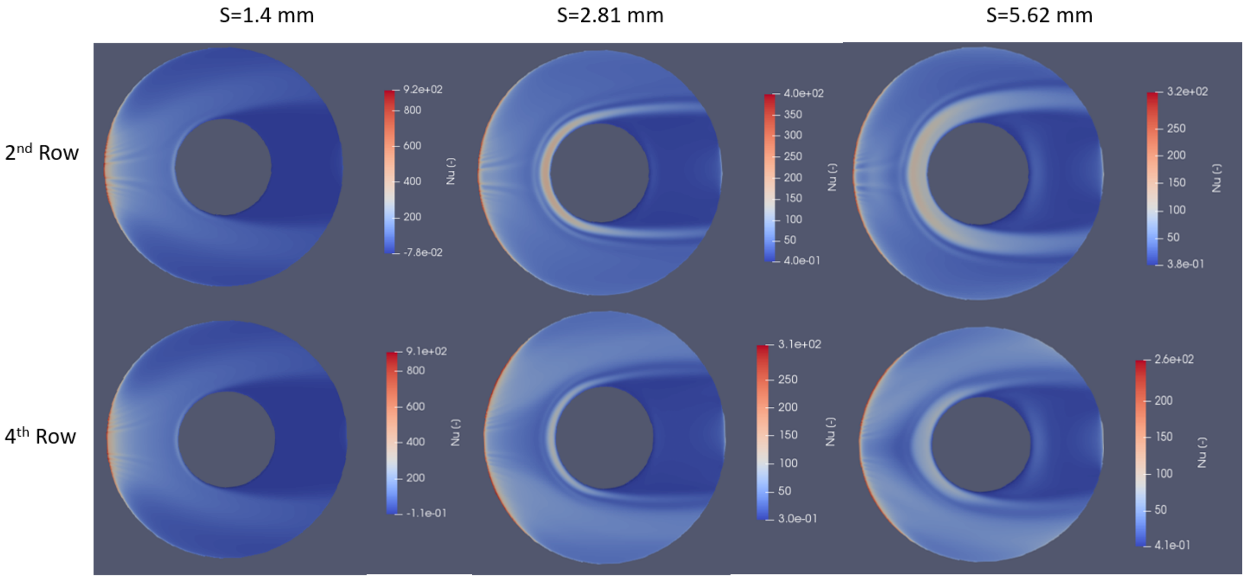

Figure 36: Distribution of Nu for the different fin pitches at the second and fourth row

As S increases the increase in heat transfer due to horseshoe vortices becomes more prominent, as seen in Figure (36). Figure (36) also show that there is a difference between $S = 1.4$ mm and the two other fin pitches. For $S = 1.4$ mm both heat transfer associated with horseshoe vortices and heat transfer due to backflow seems to be absent, this is not the case for the two others, as seen in Figure (36).

For $S = 1.4$ mm most of the heat transfer happens at the leading edge. This also seems to happen at a narrower angle θ than for the two others. For the two largest fin pitches ($S = 2.81$ mm and $S = 5.62$ mm), the increase in heat transfer is visible from the leading edge of the fin up to around $\theta = \pm 50°$. For $S = 1.4$ mm, the difference in the distribution between the second and fourth row is also smaller than for the two larger fin pitches.

Figure (36) can, however, be deceiving due to the large difference in the scale of Nu between $S = 1.4$ mm and the two others. The qualitative trends should, however, be independent of this.

The heat transfer over the fin is to an extent controlled by the boundary layer growth from where the flow impinges, as described in section 2.2.

The difference between $S = 1.4$ mm and the two other fin pitches can be because the boundary layers between the fins meet for $S = 1.4$ mm. If the boundary layers meet, the main flow does not penetrate all the way to the tube, this fits well with the absence of horseshoe vortices [48, 67]. When the boundary layers meet, the fin pitch restricts the maximum boundary layer thickness to half of the distance between the fins. A smaller boundary layer thickness is associated with a higher heat transfer coefficient, as described in section 2.2. This then indicates that Nu should increase as the fin pitch decreases.

On the other hand, as the fin pitch decreases less of the flow goes between the fins due to the increase in friction surface, increasing the bypass flow. This indicates that Nu should decrease as the fin pitch decreases. As seen in Figure (35b), the simulation results show Nu to increase going from $S = 2.81$ mm to $S = 1.4$ mm. The simulation results by Lindqvist et al. [36] shows this increase to continue up to around $S = 1.1$ mm for this geometry, then drop off (see Figure (17) in section 2.4).

Investigating this shift in the behaviour of Nu using streamlines, Lindqvist et al. [36] found the bypass effect described above to increase as S decreases. The drop off can therefore have been caused by the effect of bypass-flow overtaking the effect of a smaller boundary layer thickness. As described in section 2.4, the simulation results by Mon [48] showed an increase in the heat transfer coefficient going from $S = 1.2$ mm to $S = 2.6$ mm. This is the opposite to the simulation results in Figure (35b), and the simulation results by

Lindqvist et al. [36] shown in Figure (17). If this is down to differences in geometry, is unclear.

Again, this is only an attempt to explain the simulation results, and further research is needed to understand the details better. It is also worth pointing out that the same numerical error as was found in the project thesis [65], with a zone of the opposite sign of Nu behind the tube is also found for the simulation with $S = 1.4$ mm, as seen in Figure (36).

Comparing the distribution of Nu for the $S = 2.81$ mm and $S = 5.62$ mm simulations, there seem to be more pronounced horseshoe vortices and more backflow for the simulation with $S = 5.62$ mm as can be seen in Figure (36). Both these phenomena are expected to increase Nu.

Looking at the distribution of Nu at the fourth row for these two fin pitches, there is an area in front of the fin with lower heat transfer, as seen in Figure (36). This area is larger in the result for the simulation with $S = 2.81$ mm compared to the simulation with $S = 5.62$ mm. This indicates that the bypass flow decreases as S increases, which is as expected. This is also a phenomenon expected to increase Nu.

There are, however, no observable increase in the overall heat transfer coefficient between these two fin pitches, as seen in Figure (35b). Why this is, can only be speculated on.

A possibility is that the friction is more or less the same between the two fin pitches, and thus the velocity between the fins is more or less the same. With the higher pressure drop for $S = 2.81$ mm seen in Figure (35a) not being down to more friction surface, but the flow having to change direction more. This could equate to little difference in Nu.

Another possibility is that the increase in S indeed reduced the friction, resulting in less bypass flow. Therefore, more of the fin is engulfed in the flow, but the acceleration associated with bypass flow is smaller, so the jet-like flow impinging the fin is weaker. This could, again, equate to little difference in Nu.

None of these speculations into why the result for Nu is constant going from $S = 2.81$ mm to $S = 5.62$ mm have, however, been tested out or investigated further. There is also the possibility that the numerical results are wrong, and more simulations are needed to understand this behaviour.

Layout

The initial five-row simulation with dimensions described in section 3.4 had a tube layout angle $\beta = 30°$. Simulations were performed with three other layouts. The tube layout angle, the transverse pitch and the longitudinal pitch used in each of the simulations are shown in Table (5).

Table 5: Dimensions relating to the bundles used for the different simulated layouts

Tube layout angle (β)	Longitudinal pitch (P_t) [mm]	Transverse pitch (P_l) [mm]
30°	38.7	33.5
45°	54.7	27.73
60°	67	19.35
90°	38.7	38.7

To keep the bundles as similar as possible, the $\beta = 60°$ layout is the same as the $\beta = 30°$ layout but turned by 90°. The $\beta = 90°$ layout has the same transverse pitch as the $\beta = 30°$ layout, and the $\beta = 45°$ layout is the same as the $\beta = 90°$ layout, but turned by 45°.

To get the best comparison, the Reynolds number calculated in the transverse plane was kept constant at $Re_{P_t} = 5500$, instead of a constant Re_{do} as used in the simulations with different fin tip clearances and fin pitches. It is, however, only for the $\beta = 60°$ layout that this is different. For this layout, the minimum free-flow area is in the diagonal plane, not the transverse plane. In hindsight, keeping Re_{do} constant might have been better.

The simulation results are compared with the tube layout angle corrections by Næss [52] shown in equations (12) and (13) in section 2.4 for Nu and Eu respectively. Both of these are compared relative to the

$\beta = 30°$ layout. In Figure (37) the corrections are therefore multiplied with the simulation results for $\beta = 30°$. The corrections are also only given in the points corresponding to the different layouts simulated. This is because the corrections do not use β as the parameter to describe the layout, but an area ratio and a pitch ratio, as described in section 2.4.

The results for the simulations with different layouts are shown in Figure (37).

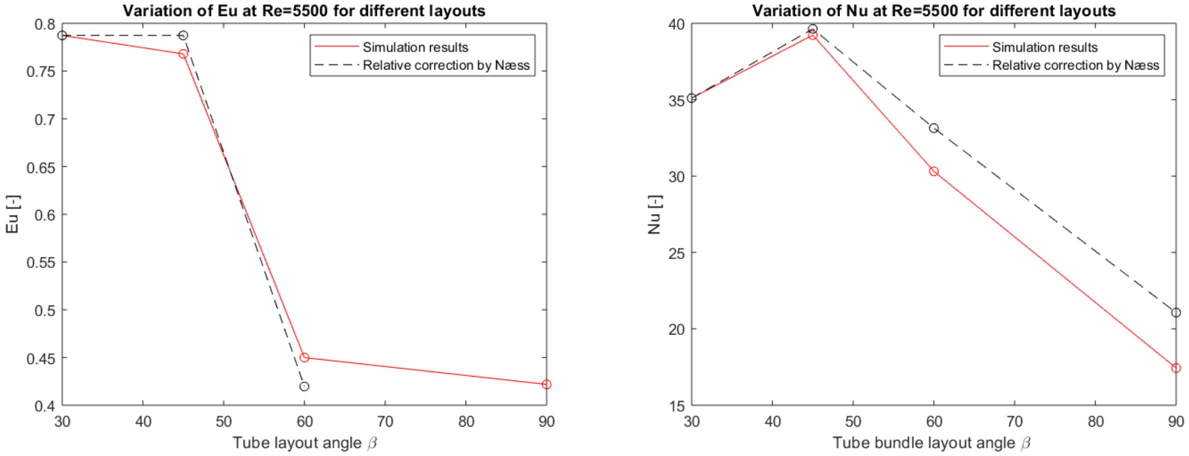

(a) (b)

Figure 37: Overall Eu (a) and overall Nu (b) for different layouts compared with a relative correlation by Næss [52]

As can be seen in Figure (37), the results for both Nu and Eu follow the corrections by Næss [52] quite well. For Eu, the simulation results are around 2.5% below and 7% above the correction by Næss [52] for the $\beta = 45°$ layout and the $\beta = 60°$ layout respectively, as seen in Figure (37a). For Nu, the result for the $\beta = 60°$ layout is around 9% below the corrections by Næss [52], while the results for the in-line, $\beta = 90°$, layout is around 17% below. The $\beta = 45°$ layout result is within 1% of the correction by Næss [52], as seen in Figure (37b).

For the heat transfer behaviour, Næss [52] compared his own experimental results with the experimental results by Ackerman and Brunsvold [1], both of which are shown in Figure (18) in section 2.4. From $\beta \approx 30°$ up to $\beta \approx 45°$ these follow a similar trend, which follows the prediction of the correlation by Weierman [73], also shown in Figure (18). The simulation result for the $\beta = 45°$ layout also follows this trend, as seen in Figure (37b). Næss [52] also compared his experimental results with some other correlations, as seen in Figure (18), these do not follow the same trend as the experimental results.

For $\beta = 60°$, the only study found is by Næss [52]. The Reynolds number for this layout is, as described in section 2.4, calculated in the diagonal plane in the study by Næss [52], while for the simulation result, the Reynolds number is calculated in the transverse plane. This makes a direct quantitative comparison difficult. The qualitative trends are, however, similar for both Eu and Nu, as seen in Figure (37). The Reynolds number for this simulation calculated in the diagonal plane is around 15% higher than in the transverse plane. This means the real underprediction of Nu compared to the correction by Næss [52] probably is a little larger than shown in Figure (37b), while for Eu it is a little less than shown in Figure (37a).

For the $\beta = 90°$ layout, there is more variation in the literature, as described in section 2.4. For comparison, the ratio of the $\beta = 90°$ layout result to the $\beta = 30°$ layout result is used. Using this ratio for Nu, there is a variation from 0.57 and 0.6 found by Weierman et al. [75] and Næss [52] respectively up to around 0.82 found by Ackerman and Brunsvold [1]. The simulation results for Nu, shown in Figure (37b), has a ratio of around 0.5. This is a little less than the experimental values found in the literature.

Weierman et al. [75] found the same ratio of around 0.57 for the pressure drop as well. Mon [48] found numerically this ratio to be around 0.6 for Eu. In the simulation results for Eu shown in Figure (37a), this ratio is around 0.54. This is again a little lower than the results from the literature, but with the ratio by Weierman et al. [75] being the closest.

The distribution of Nu for the different layouts are shown in Figure (38).

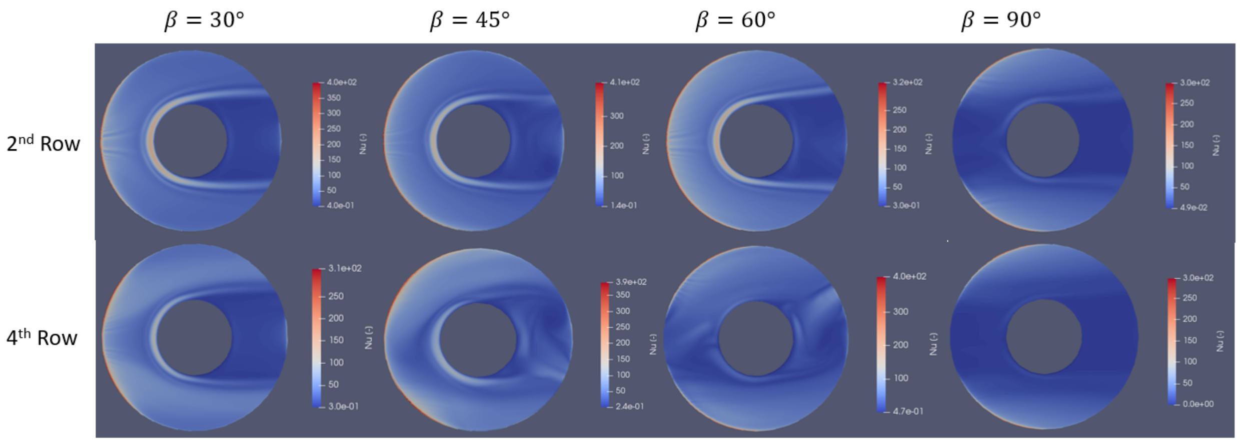

Figure 38: Distribution of Nu for the different layouts at the second and fourth row

Figure (38) shows that as β increases, the maximum angle θ, where the flow impinges the edge of the fin, increases. For the in-line, $\beta = 90°$, layout the flow does not impinge the leading edge of the fin. Instead, the flow impinges a little to each side, due to the preceding row. An implication of this is that the increase in heat transfer due to horseshoe vortices is less than for the staggered layouts, as can be seen in Figure (38). This is as expected based on the literature described in section 2.2, and has the effect of lowering Nu compared to a staggered layout, as seen in Figure (37b).

For $\beta = 45°$, there is a mixing effect at the trailing edge of the fin for the second row, where the legs of the horseshoe vortices are not symmetric, as seen in Figure (38).

For the fourth row, this mixing effect is even more pronounced, and now visible in front and behind the tube in both the results for the $\beta = 45°$ and $\beta = 60°$ layouts. The effect is more pronounced for the $\beta = 60°$ layout, as seen in Figure (38).

The leading-edge heat transfer at the fourth row for these two layouts are also lower compared with a little to each side, in the same way as for the in-line layout. This is, again, most visible for the $\beta = 60°$ layout, as seen in Figure (38). This might indicate a shift in the behaviour from what is associated with a staggered layout towards what is associated with an in-line layout as β increases. The behaviour of a staggered and of an in-line layout are both described in section 2.2, but also well represented in the results for the $\beta = 30°$ and $\beta = 90°$ layouts respectively.

To further investigate this shift in the behaviour, the velocity vectors were plotted for the $\beta = 30°$, $\beta = 45°$ and $\beta = 60°$ layouts. The velocity vectors are shown in Figure (39), and the colour corresponds to the temperature.

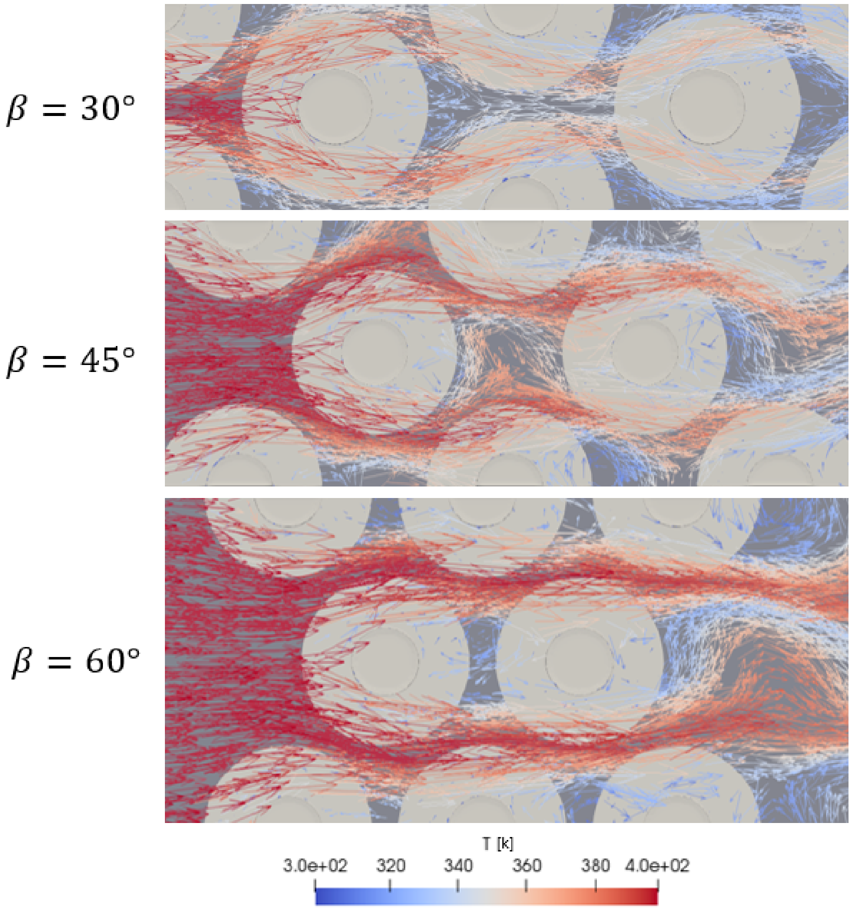

Figure 39: Velocity vectors/Streamlines for the $\beta = 30°$, the $\beta = 45°$ and the $\beta = 60°$ layouts. The colours correspond to temperature

As can be seen in Figure (39), these streamlines show the gradual shift from a staggered to an in-line behaviour. The mixing effect for the $\beta = 45°$ layout at the second row seems like a consequence of the layout and the choice of P_l and P_t (see Table (5)). For this layout, there is more space for flow to recirculate between the finned-tube rows. This because P_l is larger compared with the $\beta = 60°$ layout and because P_t is larger and less restrictive compared with the $\beta = 30°$ layout.

Compared to the $\beta = 30°$ layout, the velocity in the diagonal plane is, also, higher for the $\beta = 45°$ layout. This means more of the fin is exposed to higher velocity in the $\beta = 45°$ layout. The velocity in the diagonal plane is higher for the $\beta = 45°$ layout because the area in the transverse and diagonal plane is roughly the same for this layout. For the $\beta = 30°$ layout, the area in the diagonal plane is twice that of the transverse plane.

This higher velocity is believed to be the reason the overall heat transfer is higher for the $\beta = 45°$ layout compared to the $\beta = 30°$ layout, as seen in Figure (37b). The higher velocity in the diagonal plane seems to make the most difference a little into the bundle, as seen in the row-by-row heat transfer coefficient shown in Figure (C.3) in appendix C. The heat transfer coefficients are more or less the same for the two layouts at the first and second row, then the $\beta = 45°$ layout has a significantly higher heat transfer coefficient for the third and fourth row. For the fifth row, the $\beta = 30°$ layout has a higher heat transfer coefficient. This might be because it is the last row, and simulations with more rows are needed in order to investigate this.

For the $\beta = 60°$ layout, the main flow changes direction much less than for the two smaller β simulations, behaving more like an in-line layout, as seen in Figure (39). This is believed to explain the drop in both the overall Nu and Eu seen in Figure (37). The row-by-row heat transfer coefficient for the $\beta = 60°$ layout is shown in Figure (C.3) in appendix C. This shows a drop in the heat transfer coefficient as the number of rows increases, which is associated with the row-by-row behaviour of an in-line layout, as described in section 2.3. At the same time, oscillations in the heat transfer coefficient between the rows, associated with the row-by-row behaviour of a staggered bundle, is still present.

This might explain the higher heat transfer coefficient of the $\beta = 60°$ layout compared with the in-line, $\beta = 90°$, layout. It is, however, again worth pointing out that the Reynolds number for this simulation is calculated in the transverse plane, while the minimum free-flow area is in the diagonal plane. Calculating the Reynolds number in the diagonal plane for this simulation gives $Re_{do} \approx 6300$. Comparing this to a simulation with a $\beta = 60°$ layout at $Re_{do} = 5500$, one expects the latter to have a lower Nu and a higher Eu.

As mentioned in the section investigating different fin tip clearances above, the $\beta = 45°$ layout did have some problems in the mesh. Both the grids for the simulation with $C_f = 0$ and $\beta = 45°$ had different names for some of the boundaries. The different names came from the splitting of the grids into the different regions. However, why OpenFOAM assigned different names to some of the boundaries is unclear. This splitting process is described in section 3.4.

The simulation with a $\beta = 45°$ layout also behaved unexpectedly with regards to sampling the in- and out-let pressure. The pressure drop remained fairly constant over many successive iterations, and this is the value used in the result for Eu in Figure (37a). However, for a few iterations after the pressure drop had stabilised, the pressure drop was significantly different. Using this value in calculating Eu gives a straight line from the result for the $\beta = 30°$ layout down to the result for the $\beta = 60°$ layout instead of the drop shown in Figure (37a). This result is therefore expected to have higher uncertainty for Eu, and new simulations with a $\beta = 45°$ layout are needed to investigate the pressure drop behaviour.

It is worth pointing out that both the simulations with a $\beta = 45°$ layout and a fin tip clearance $C_f = 0$ had a higher y_p^+ value compared to the rest of the simulations in this section. These two simulations did, as mentioned, have grids that behaved differently when split into regions. The maximum y_p^+ value found in the simulation with a $\beta = 45°$ layout was $y_p^+ \approx 8$ and the maximum value found in the simulation with $C_f = 0$ was around $y_p^+ \approx 5$. This is significantly higher than the recommended maximum value of $y_p^+ \sim 2$ found in the y_p^+-investigation in section 3.2. Using a too high y_p^+ value gave in section 3.2 an increase in Nu.

Whether the y_p^+ influence explains some of the increase in the simulation with $\beta = 45°$ compared with the $\beta = 30°$ layout seen in Figure (37b), is unclear, and further research is needed.

All the other simulations with changes in different geometry parameters had maximum values for y_p^+ around $y_p^+ \approx 2.5$.

5 Conclusions

In this thesis, the one-row model developed in the project thesis was extended to a full bundle of finned-tubes. The CFD simulations were performed in the open-source software OpenFOAM.

A study of literature was performed, and the literature was used for comparison and validation of the simulation results.

The mesh investigation performed in the project thesis was deemed unsatisfactory, and a more thorough investigation was performed. This included a new grid convergence test, and a background grid with size $h = 0.35$ mm was deemed good enough.

The effects of y_p^+ and usage of wall functions were also investigated. The findings showed that y_p^+ should be kept under two. These findings are close to recommendations for y_p^+ values found in the literature [58]. No apparent difference was found between simulations with wall functions and without wall functions. Using an adiabatic boundary condition for the fin tips were, however, found to give a difference in the result for the heat transfer. This boundary condition was assumed to be more accurate and was used for all the full bundle simulations.

Suitable turbulence models for the problem were investigated in the literature. These models were then tested out on the one-row simulation domain. Some differences were found between the models, but it was difficult to judge which of them performed best. The Spalart-Allmaras turbulence model was, therefore, chosen due to its simplicity and stability. This is also the model used in the project thesis.

Both the investigations of the mesh and of the different turbulence models used the one-row model and were performed at a relatively low Reynolds number. An assumption was made that these results are valid for the full bundle domain. This assumption does not necessarily hold true, and further research redoing these investigations using a full bundle model at a higher Reynolds number is necessary. The findings using the one-row model do, however, match well with the literature. These findings in the literature were used to aid in the choice of a suitable turbulence model and a suitable background mesh.

A lot of problems were experienced in the grid generation for the eight-row full bundle simulations. Due to these problems caused by the apparent limitations in the meshing tool "snappyHexMesh", the Reynolds number had to be restricted to $Re_{do} \approx 5500$. Even at this Reynolds number the findings for a maximum advisable y_p^+ found in the y_p^+ investigation were violated in some of the full bundle simulations.

The three initial full bundle simulations with eight rows were compared to the literature in terms of Nu and Eu. The results were found to be within the error band of the experimental correlations used for comparison. The row-by-row results for Nu were also investigated for these simulations, and compared to the literature. Both the highest and lowest Reynolds number simulation were found to behave differently than expected. For the lowest Reynolds number simulation, this was put down to a small temperature difference for the last rows due to the low Reynolds number. The last simulation did, however, behave as expected.

The row-by-row behaviour of these simulations was investigated to find the minimum number of rows that are needed to model a full bundle. This was done to shrink the computational domain and save computational time. However, due to a shift in the geometry no conclusions could be made for how many rows need to be modelled. This shift came from a mistake made in the drawings of the geometry and thus in the stl-files used in the grid generation.

A reduced domain full bundle model with cyclic boundary conditions in the streamwise direction was also investigated. This too was investigated to try and save computational time. The model was inspired by the work of Lindqvist et al. [34] and Martinez et al. [43].

However, no successful implementation of such a model was achieved. Some inconsistencies were found in the work by Martinez et al. [43], and these have been pointed out. Lindqvist et al. [34] implemented a reduced domain model for, among others, the geometry used in this thesis. The work by Lindqvist et al. [34] does, however, lack clear instructions for how the implementation was achieved.

A decision was made to use five rows for the investigation of different geometry parameters instead of eight. To get a better comparison for the results of these simulations, a new simulation with the initial geometry was performed. This also used five rows instead of eight and had the correct, non-shifted geometry.

The new simulation with five rows was found to have a significantly lower result for Nu compared to the eight-row simulation. The difference was a 26% lower value for Nu in the five-row simulation. Apart from the shift in the mesh for the eight-row simulation, and lower maximum y_p^+ for the five-row simulation, no good explanation has been found for the difference, and further investigations are needed. This difference gives some doubt to the validity of all the full bundle simulations, and the investigation of geometry differences starts out with a less validated model than ideal.

To get the best relative results in the investigation of different geometry parameters, the mesh was, therefore, made as similar as possible. The hope was that the relative results should be representative of the geometry changes, even if the absolute results are off.

The results of changes in the geometry parameters were compared to the literature in terms of the overall Eu and Nu. The local heat transfer coefficient was also compared and used to try and understand the changes in the overall heat transfer. How the distribution of Nu changes with both changes in the geometry and through the bundle is a topic that is lacking in the literature. This is something new the results in this thesis provides.

The results of the simulations with changes in the fin tip clearance were compared with experimental results by Holfeld [17]. For Nu, a decreasing trend going from the original C_f down to where the fins touch is visible in both the simulation result and experimental result. This is believed to be caused by the wake of the preceding rows. Increasing C_f to double that of the original geometry shows an increase in Nu in the simulation results, while the experimental results show a decrease. Some speculations into why this is have been given, but further investigations into the behaviour are needed. For Eu, the simulation results show a steady decrease as C_f increases. This is believed to be caused by an increase in the bypass flow.

For the fin pitch, the simulation results were compared with the correlations by Holfeld [17]. For Eu, the simulation results were in good agreement with the correlation. For Nu, the results showed the opposite trend. The trend in the simulation results is, however, the same as was found by Lindqvist et al. [36]. The simulation results show a significant difference between the smallest fin pitch of $S = 1.4$ mm and the two others. This difference is believed to be caused by the boundary layers growing over the fins meeting for the smallest fin pitch. An increase in Nu was also seen for the result with the smallest fin pitch compared to the two others. Some possible explanations for this are discussed, but further research is needed.

Increasing the fin pitch from the original geometry up to $S = 5.62$ mm gave no observable difference in Nu. This is, again, not fully understood, but some possible reasons are discussed. Further research is needed.

For the simulations with different tube layouts, the results were compared with relative layout corrections by Næss [52]. The results were in good agreement with these corrections, reproducing the same trends for both Nu and Eu. The simulation results show a shift in the behaviour from a staggered towards an in-line layout as the tube layout angle β increases. This shift was clear to see in a comparison of the streamlines for the three staggered layouts.

The Nu result of simulation with a $\beta = 45°$ layout was higher than the Nu result for the simulation with a $\beta = 30°$ layout. Some possible explanations for this have been discussed, however, further research into this is needed. This simulation also had a higher y_p^+ value compared with the other simulations in the investigation of layouts, and some fluctuations in the pressure drop. A new simulation with a $\beta = 45°$ layout is therefore needed to confirm the behaviour in the result. The row-by-row result for Nu in this simulation also indicates that only modelling five rows is not sufficient to understand the behaviour fully.

6 Further work

Some of the behaviours difficult to explain in the results are believed to be caused by a poor-quality mesh in the simulations. This is difficult to prove without redoing the simulations with a better mesh. However, given all the problems in the grid generation for the full bundle model described in section 3.4, it seems likely.

The meshing tool "snappyHexMesh" in OpenFOAM does not seem able to generate a sufficiently good grid for simulations of finned-tube bundles. For further studies, a different meshing tool should be considered.

Likewise for the sampling plane tool in OpenFOAM. This does not seem very consistent and accurate, as found in the postprocessing of the eight-row full bundle results. Using an external tool to postprocess the simulation data should be considered.

The investigation of turbulence models was done using the one-row model. The one-row model was utilised instead of the full bundle model due to the limited time available in this thesis. The results are, however, not ideal. Further research into suitable turbulence models for finned-tube bundles is therefore needed. Especially since a thorough investigation at a wide range of Reynolds numbers and with a consistent mesh, seem to be lacking in the literature. The y_p^+ value was found to differ significantly between the models using the same mesh at the same Reynolds number. This then indicates that the shear stress is different between the models. This difference in y_p^+ should be visible if the forces on the finned-tubes are monitored. The distribution of the heat transfer coefficient is also a parameter that should reveal differences between the models.

The investigation of the grid was also performed on the one-row domain due to the time limit. The assumption that the findings are true for the full bundle, especially given the investigation was done at a low Reynolds number, is not great. Further investigation is therefore needed into the grid dependency of the full bundle. This should also be done at a higher Reynolds number and with $y_p^+ < 1$. Having a converged grid, further investigations can be performed varying y_p^+ and studying the effects on the results.

Apart from some differences in the grid, no good explanation has been found for the large difference in Nu between the eight-row and five-row simulation at $Re_{do} = 5500$. New simulations investigating this is therefore needed. The shift in the geometry in the eight-row simulations also means these results are of less utility. Due to this, no final conclusion could be drawn with regards to the number of rows needed to be modelled, with further investigations being necessary. The investigation performed in this thesis only investigated row-by-row heat transfer and not pressure drop. Further studies are therefore needed into how the pressure drop developes row by row and how it depends on changes in the geometry.

Only one simulation for each change of the geometry parameters was performed. This constitutes a major limitation in the results. Some trends have been pointed out with regards to the changes. However, further research investigating the parameters at a wider range of Reynolds numbers are needed. This both to verify the trends found in the simulations, but also to see how the trends change with the Reynolds number. A comparison using the same mass flow rate instead of the Reynolds number should also be performed.

For the investigation of fin pitch, no good explanation of the behaviour of Nu increasing the fin pitch from $S = 2.81$ mm up to $S = 5.62$ mm was found. Some speculations into the behaviour are discussed, but further investigations are needed. It is believed that using streamlines in multiple planes and investigating the forces on the finned surface should give more insight into the behaviour.

The same is true for the investigation of the fin tip clearances, increasing C_f from the original bundle geometry up to $C_f = 10.4$ mm. Further investigations into what causes this behaviour is also needed.

Some of the simulations performed in the investigation of geometry parameters did not go as planned. These are therefore believed to be less trustworthy compared to the rest. Both the simulation with a fin tip clearance of $C_f = 0$ and the simulation with a $\beta = 45°$ layout had similar problems in the generation of the grid. These two simulations also had a significantly higher y_p^+ compared to the other simulations in the investigation. For a better comparison, these two simulations should therefore be redone.

The behaviour of the heat transfer coefficient and pressure drop for the simulation with a $\beta = 45°$ layout is not fully understood either. A more thorough investigation like the one suggested for the fin pitch should be performed. For the simulation with a $\beta = 60°$ layout, a different area was used in the Reynolds number. This makes a comparison with the literature difficult. For this reason, a new simulation using the same area as in the literature should be performed.

A reduced computational domain was also investigated in this thesis; however, no good implementation was achieved. Some inconsistencies found in the literature describing the implementation has been pointed out. Further investigations of these are needed.

References

[1] J. W. Ackerman and A. R. Brunsvold. "Heat Transfer and Draft Loss Performance of Extended Surface Tube Banks". In: *Journal of Heat Transfer* 92 (May 1970), pp. 215–220. ISSN: 0022-1481. DOI: 10.1115/1.3449652. eprint: https://asmedigitalcollection.asme.org/heattransfer/article-pdf/92/2/215/5743991/215_1.pdf. URL: https://doi.org/10.1115/1.3449652.

[2] Helge I. Andersson. "Introduction to turbulence modelling". Lecture notes in subject 76572 Turbulent flow, NTNU. Oct. 1988.

[3] Samy M. El-Behery and Mofreh H. Hamed. "A comparative study of turbulence models performance for separating flow in a planar asymmetric diffuser". In: *Computers & Fluids* 44 (2011), pp. 248–257. ISSN: 0045-7930. DOI: https://doi.org/10.1016/j.compfluid.2011.01.009. URL: https://www.sciencedirect.com/science/article/pii/S0045793011000168.

[4] Samy M. El-Behery and Mofreh H. Hamed. "Advanced Turbulence Modelling of Separated Flow in a Diffuser". In: *Turbulence and Combustion* 63 (2000). ISSN: 1573-1987. DOI: https://doi.org/10.1023/A:1009930107544. URL: https://link.springer.com/article/10.1023/A:1009930107544.

[5] J. Bredeberg. *On the Wall Boundary Condition for Turbulence Models*. Internal Report 00/4. Department of Thermo and Fluid Dynamics CHALMERS UNIVERSITY OF TECHNOLOGY, Götebord Sweden, 2000.

[6] E.Gianolio and F.Cuti. "Heat Transfer Coefficients and Pressure Drops for Air Coolers with Different Numbers of Rows Under Induced and Forced Draft". In: *Heat Transfer Engineering* 3 (1981), pp. 38–48. DOI: 10.1080/01457638108939573. eprint: https://doi.org/10.1080/01457638108939573. URL: https://doi.org/10.1080/01457638108939573.

[7] P. W. Eckels and T. J. Rabas. "Heat Transfer and Pressure Drop of Typical Air Cooler Finned Tubes". In: *Journal of Heat Transfer* 107 (Feb. 1985), pp. 198–204.

[8] He FaJiang, Cao WeiWu, and Yan Ping. "Experimental Investigation of Heat Transfer and Flowing Resistance for Air Flow Cross over Spiral Finned Tube Heat Exchanger". In: *Energy Procedia* 17 (2012). 2012 International Conference on Future Electrical Power and Energy System, pp. 741–749. ISSN: 1876-6102. DOI: https://doi.org/10.1016/j.egypro.2012.02.166. URL: https://www.sciencedirect.com/science/article/pii/S1876610212005024.

[9] "Fangqing Liu.: A Thorough Description Of How Wall Functions Are Implemented In OpenFOAM." In: *In Proceedings of CFD with OpenSource Software* (2016). Edited by Nilsson. H., URL: http://www.tfd.chalmers.se/~hani/kurser/OS_CFD_2016/FangqingLiu/openfoamFinal.pdf.

[10] J.H. Ferziger and M. Peric. *Computational Methods for Fluid Dynamics*. Springer Berlin Heidelberg, 2012, pp. 167, 178. ISBN: 9783642560262. DOI: https://doi.org/10.1007/978-3-642-56026-2. URL: https://books.google.no/books?id=BZnvCAAAQBAJ.

[11] The OpenFOAM Foundation. *OpenFOAM*. https://openfoam.org/. Accessed: May. 2021.

[12] The OpenFOAM Foundation. *OpenFOAM v8 User Guide - 4.6.3 PISO, SIMPLE and PIMPLE algorithms*. https://cfd.direct/openfoam/user-guide/v8-fvSolution/. Accessed: May. 2021.

[13] The OpenFOAM Foundation. *OpenFOAM v8 User Guide - 5.2 Boundaries*. https://cfd.direct/openfoam/user-guide/v8-boundaries/. Accessed: May. 2021.

[14] The OpenFOAM Foundation. *OpenFOAM v8 User Guide - 5.4 Mesh generation with the snappyHexMesh utility*. https://cfd.direct/openfoam/user-guide/v8-snappyHexMesh/. Accessed: May. 2021.

[15] Rene Hofmann and Heimo Walter. "Experimental and Numerical Investigation of the Gas Side Heat Transfer and Pressure Drop of Finned TubesPart I: Experimental Analysis". In: *Journal of Thermal Science and Engineering Applications* 4 (Oct. 2012). 041007. ISSN: 1948-5085. DOI: 10.1115/1.4007124. URL: https://doi.org/10.1115/1.4007124.

[16] Rene Hofmann and Heimo Walter. "Experimental and Numerical Investigation of the Gas Side Heat Transfer and Pressure Drop of Finned TubesPart II: Numerical Analysis". In: *Journal of Thermal Science and Engineering Applications* 4 (Oct. 2012). 041008. ISSN: 1948-5085. DOI: 10.1115/1.4007125. URL: https://doi.org/10.1115/1.4007125.

[17] Anna Holfeld. "Experimental investigation of heat transfer and pressure drop in compact waste heat recovery units". PhD thesis. NTNU, 2016. URL: http://hdl.handle.net/11250/2432512.

[18] X. Hu and A. M. Jacobi. "Local Heat Transfer Behavior and Its Impact on a Single-Row, Annularly Finned Tube Heat Exchanger". In: *Journal of Heat Transfer* 115 (Feb. 1993), pp. 66–74. ISSN: 0022-1481. DOI: 10.1115/1.2910671. eprint: https://asmedigitalcollection.asme.org/heattransfer/article-pdf/115/1/66/5746241/66_1.pdf. URL: https://doi.org/10.1115/1.2910671.

[19] H. Huisseune et al. "Thermal Hydraulic Study of a Single Row Heat Exchanger With Helically Finned Tubes". In: *Journal of Heat Transfer* 132 (Mar. 2010). 061801. ISSN: 0022-1481. DOI: 10.1115/1.4000706. URL: https://doi.org/10.1115/1.4000706.

[20] *High-fin staggered tube banks: heat transfer and pressure drop for turbulent single phase gas flow*. Standard. ESDU, Mar. 2000.

[21] F.P. Incropera et al. *Incropera's principles of Heat and Mass Transfer*. Wiley, 2017, pp. 143–44, 153–159, 337–338, 374–375, 657, 659–660, 670–673. ISBN: 9781119382911.

[22] Hrvoje Jasak. "Error analysis and estimation for the finite volume method with applications to fluid flows." PhD thesis. Imperial College London (University of London), Jan. 1996. URL: http://hdl.handle.net/10044/1/8335.

[23] Georgi Kalitzin et al. "Near-wall behavior of RANS turbulence models and implications for wall functions". In: *Journal of Computational Physics* 204 (2005), pp. 265–291. ISSN: 0021-9991. DOI: https://doi.org/10.1016/j.jcp.2004.10.018. URL: http://www.sciencedirect.com/science/article/pii/S0021999104004164.

[24] W M Kays and A L London. *Compact heat exchangers*. McGraw-Hill, 1984, pp. 36. ISBN: 9789387938038.

[25] W.M. Kays and M.E. Crawford. *Convective Heat and Mass Transfer, Second Edition*. McGraw-Hill Series in Management. McGraw-Hill, 1980, pp. 169–171, 173. ISBN: 9780070334571. URL: https://books.google.no/books?id=PpkeAQAAIAAJ.

[26] S. P. Kearney and A. M. Jacobi. "Local Convective Behavior and Fin Efficiency in Shallow Banks of In-Line and Staggered, Annularly Finned Tubes". In: *Journal of Heat Transfer* 118 (May 1996), pp. 317–326. ISSN: 0022-1481. DOI: 10.1115/1.2825847. eprint: https://asmedigitalcollection.asme.org/heattransfer/article-pdf/118/2/317/5669283/317_1.pdf. URL: https://doi.org/10.1115/1.2825847.

[27] Sean Kearney and A.M. Jacobi. *Local and Average Heat Transfer and Pressure Drop Characteristics of Annularly Finned Tube Heat Exchangers*. ACRC Technical Report. Air Conditioning and Refrigeration Center. College of Engineering. University of Illinois at Urbana-Champaign., Jan. 1995. URL: http://hdl.handle.net/2142/10990.

[28] Johan C. Kok. “Resolving the Dependence on Freestream Values for the $k - \omega$ Turbulence Model”. In: *AIAA Journal* 38 (2000), pp. 1292–1295. DOI: 10.2514/2.1101. URL: https://doi.org/10.2514/2.1101.

[29] Robin B. Langtry and Florian R. Menter. “Correlation-Based Transition Modeling for Unstructured Parallelized Computational Fluid Dynamics Codes”. In: *AIAA Journal* 47 (2009), pp. 2894–2906. DOI: 10.2514/1.42362. URL: https://doi.org/10.2514/1.42362.

[30] Robin Blair Langtry. “A correlation-based transition model using local variables for unstructured parallelized CFD codes”. PhD thesis. University of Stuttgart, May 2006. URL: http://dx.doi.org/10.18419/opus-1705.

[31] B. E. Launder, G. J. Reece, and W. Rodi. “Progress in the development of a Reynolds-stress turbulence closure”. In: *Journal of Fluid Mechanics* 68 (1975), pp. 537–566. DOI: 10.1017/S0022112075001814.

[32] Mooyeon Lee, Taehyung Kang, and Yongchan Kim. “Air-side heat transfer characteristics of spiral-type circular fin-tube heat exchangers”. In: *International Journal of Refrigeration* 33 (2010), pp. 313–320. ISSN: 0140-7007. DOI: https://doi.org/10.1016/j.ijrefrig.2009.09.019. URL: http://www.sciencedirect.com/science/article/pii/S0140700709002308.

[33] Karl Lindqvist. “Computational Fluid Dynamics Modeling of Flow and Heat Transfer in Fin-Tube Bundles”. PhD thesis. NTNU, 2019. URL: http://hdl.handle.net/11250/2583704.

[34] Karl Lindqvist and Erling Næss. “A validated CFD model of plain and serrated fin-tube bundles”. In: *Applied Thermal Engineering* 143 (2018), pp. 72–79. ISSN: 1359-4311. DOI: https://doi.org/10.1016/j.applthermaleng.2018.07.060. URL: http://www.sciencedirect.com/science/article/pii/S1359431117359598.

[35] Karl Lindqvist and Erling Næss. “Numerical modeling of vortex shedding in helically wound finned tube bundles in cross flow”. In: *International Heat Transfer Conference (IHTC)* 16 (2018), pp. 1843–1850. ISSN: 2377-424X. DOI: https://doi.org/10.1615/IHTC16.cms.024036. eprint: http://ihtcdigitallibrary.com/conferences/ihtc16,1b62c5720219fa67,4ffa35c077d9305a.html.

[36] Karl Lindqvist and Erling Næss. “On correction factors in thermal-hydraulic correlations for compact fin-tube bundles”. In: *Heat and Mass Transfer* 56 (June 2020). DOI: 10.1007/s00231-019-02772-1.

[37] Eirik Løland Eide. “Numerical investigation of thermal-hydraulics performance of fin-tube waste heat recovery units”. MA thesis. NTNU, 2015. URL: http://hdl.handle.net/11250/2350185.

[38] OpenCFD Ltd. *OpenFOAM*. https://www.openfoam.com/. Accessed: May. 2021.

[39] OpenCFD Ltd. *OpenFOAM: User Guide v2012 - Linear eddy viscosity models*. https://www.openfoam.com/documentation/guides/latest/doc/guide-turbulence-ras-linear-eddy-viscosity-models.html. Accessed: May. 2021.

[40] Youfu Ma et al. “Experimental investigation of heat transfer and pressure drop in serrated finned tube banks with staggered layouts”. In: *Applied Thermal Engineering* 37 (2012), pp. 314–323. ISSN: 1359-4311. DOI: https://doi.org/10.1016/j.applthermaleng.2011.11.037. URL: https://www.sciencedirect.com/science/article/pii/S135943111100665X.

[41] W.A. Mair, P.D.F. Jones, and R.K.W. Palmer. “Vortex shedding from finned tubes”. In: *Journal of Sound and Vibration* 39 (1975), pp. 293–296. ISSN: 0022-460X. DOI: https://doi.org/10.1016/S0022-460X(75)80082-4. URL: http://www.sciencedirect.com/science/article/pii/S0022460X75800824.

[42] Paul Malan, Keerati Suluksna, and Ekachai Juntasaro. “Calibrating the $\gamma - Re_\theta$ Transition Model for Commercial CFD”. In: *47th AIAA Aerospace Sciences Meeting including The New Horizons Forum and Aerospace Exposition*. DOI: 10.2514/6.2009-1142. URL: https://arc.aiaa.org/doi/abs/10.2514/6.2009-1142.

[43] E. Martinez et al. “Numerical simulation of turbulent air flow on a single isolated finned tube module with periodic boundary conditions”. In: *International Journal of Thermal Sciences* 92 (2015), pp. 58–71. ISSN: 1290-0729. DOI: https://doi.org/10.1016/j.ijthermalsci.2015.01.024. URL: https://www.sciencedirect.com/science/article/pii/S1290072915000277.

[44] F. R. Menter. “A Comparison of Some Recent Eddy-Viscosity Turbulence Models”. In: *Journal of Fluids Engineering* 118 (Sept. 1996), pp. 514–519. ISSN: 0098-2202. DOI: 10.1115/1.2817788. URL: https://doi.org/10.1115/1.2817788.

[45] F. R. Menter. “Influence of freestream values on k-omega turbulence model predictions”. In: *AIAA Journal* 30 (1992), pp. 1657–1659. DOI: 10.2514/3.11115. URL: https://doi.org/10.2514/3.11115.

[46] F. R. Menter et al. “A Correlation-Based Transition Model Using Local VariablesPart I: Model Formulation”. In: *Journal of Turbomachinery* 128 (Mar. 2004), pp. 413–422. ISSN: 0889-504X. DOI: 10.1115/1.2184352. URL: https://doi.org/10.1115/1.2184352.

[47] Fredrik Mentzoni et al. “Numerical modeling of turbulence above offshore helideck Comparison of different turbulence models”. In: *Journal of Wind Engineering and Industrial Aerodynamics* 141 (2015), pp. 49–68. ISSN: 0167-6105. DOI: https://doi.org/10.1016/j.jweia.2015.02.005. URL: https://www.sciencedirect.com/science/article/pii/S0167610515000483.

[48] Mi Sandar Mon. “Numerical Investigation of Air-Side Heat Transfer and Pressure Drop in Circular Finned-Tube Heat Exchangers ”. PhD thesis. TU Bergakademie Freiberg, Freiberg, 2003. URL: https://nbn-resolving.org/urn:nbn:de:swb:105-26331.

[49] Max Monheit. “Comparative experimental performance of high-finned tubes in staggered equilateral and equivelocity layouts”. In: *Experimental Thermal and Fluid Science* 1 (1988), pp. 75–81. ISSN: 0894-1777. DOI: https://doi.org/10.1016/0894-1777(88)90050-7. URL: https://www.sciencedirect.com/science/article/pii/0894177788900507.

[50] J.A. Moore, J.P.J. Stevenson, and R. Grimes. “Thermal and flow characteristics of a single-row circular-finned tube heat exchanger under elevated free-stream turbulence”. In: *International Journal of Heat and Fluid Flow* 57 (2016), pp. 48–57. ISSN: 0142-727X. DOI: https://doi.org/10.1016/j.ijheatfluidflow.2015.11.001. URL: http://www.sciencedirect.com/science/article/pii/S0142727X15001319.

[51] Bernhard Müller. “Introduction to Computational Fluid Dynamics”. Lecture notes for the course Computaional Heat and Fluid Flow, EPT, NTNU. Nov. 2018.

[52] Erling Næss. “Experimental investigation of heat transfer and pressure drop in serrated-fin tube bundles with staggered tube layouts”. In: *Applied Thermal Engineering* 30 (2010), pp. 1531–1537. ISSN: 1359-4311. DOI: https://doi.org/10.1016/j.applthermaleng.2010.02.019. URL: http://www.sciencedirect.com/science/article/pii/S1359431110000785.

[53] Hossain Nemati and M. A. Moghimi. “Numerical study of flow over annular-finned tube heat exchangers by different turbulent Models”. In: *CFD Letters* 6 (Jan. 2014), pp. 101–112.

[54] A. NIR. “Heat Transfer and Friction Factor Correlations for Crossflow over Staggered Finned Tube Banks”. In: *Heat Transfer Engineering* 12 (1991), pp. 43–58. DOI: 10.1080/01457639108939746. URL: https://doi.org/10.1080/01457639108939746.

[55] *OpenFOAM: User Guid - Spalart-Allmaras*. https://www.openfoam.com/documentation/guides/latest/doc/guide-turbulence-ras-spalart-allmaras.html. Accessed: Nov. 2020.

[56] CFD Direct - The Architects of OpenFOAM. *Energy Equation in OpenFOAM*. https://cfd.direct/openfoam/energy-equation/. Accessed: June. 2021.

[57] S. V. Patankar, C. H. Liu, and E. M. Sparrow. “Fully Developed Flow and Heat Transfer in Ducts Having Streamwise-Periodic Variations of Cross-Sectional Area”. In: *Journal of Heat Transfer* 99 (May 1977), pp. 180–186. ISSN: 0022-1481. DOI: 10.1115/1.3450666. URL: https://doi.org/10.1115/1.3450666.

[58] R.H. Pletcher, J.C. Tannehill, and D. Anderson. *Computational Fluid Mechanics and Heat Transfer, Second Edition*. Series in Computational and Physical Processes in Mechanics and Thermal Sciences. Taylor & Francis, 1997, pp. 276–280, 470–471. ISBN: 9781560320463. URL: https://books.google.no/books?id=ZJPbtHeilCgC.

[59] Parinya Pongsoi et al. "Effect of fin pitches on the air-side performance of L-footed spiral fin-and-tube heat exchangers". In: *International Journal of Heat and Mass Transfer* 59 (2013), pp. 75–82. ISSN: 0017-9310. DOI: https://doi.org/10.1016/j.ijheatmasstransfer.2012.11.071. URL: https://www.sciencedirect.com/science/article/pii/S0017931012009349.

[60] T. J. RABAS and F. V. HUBER. "Row Number Effects on the Heat Transfer Performance of In-Line Finned Tube Banks". In: *Heat Transfer Engineering* 10 (1989), pp. 19–29. DOI: 10.1080/01457638908939713. URL: https://doi.org/10.1080/01457638908939713.

[61] Christopher Rumsey. *Langley Research Center - Turbulence Modeling Resource*. Accessed: Feb. 2021. URL: https://turbmodels.larc.nasa.gov/.

[62] Tsan-Hsing Shih et al. "A new k-ϵ eddy viscosity model for high reynolds number turbulent flows". In: *Computers & Fluids* 24 (1995), pp. 227–238. ISSN: 0045-7930. DOI: https://doi.org/10.1016/0045-7930(94)00032-T. URL: https://www.sciencedirect.com/science/article/pii/004579309400032T.

[63] Magnus Själander et al. *EPIC: An Energy-Efficient, High-Performance GPGPU Computing Research Infrastructure*. 2019. arXiv: 1912.05848 [cs.DC].

[64] *Design and Optimization of Waste Heat Recovery Unit Using Carbon Dioxide as Cooling Fluid*. Vol. Volume 1: Fuels and Combustion, Material Handling, Emissions; Steam Generators; Heat Exchangers and Cooling Systems; Turbines, Generators and Auxiliaries; Plant Operations and Maintenance; Reliability, Availability and Maintainability (RAM); Plant Systems, Structures, Components and Materials Issues. ASME Power Conference. V001T03A006. July 2014. DOI: 10.1115/POWER2014-32165. URL: https://doi.org/10.1115/POWER2014-32165.

[65] Andreas H. Søgnen. "Numerical analysis of finned-tubed heat exchangers". Project work, EPT, NTNU. Dec. 2020.

[66] Philippe Spalart and Steven Allmaras. "A One-Equation Turbulence Model for Aerodynamic Flows". In: *AIAA* 439 (Jan. 1992). DOI: 10.2514/6.1992-439. URL: https://arc.aiaa.org/doi/abs/10.2514/6.1992-439.

[67] Hyung Jin Sung, Jung Seung Yang, and Tae Seon Park. "Local convective mass transfer on circular cylinder with transverse annular fins in crossflow". In: *International Journal of Heat and Mass Transfer* 39 (1996), pp. 1093–1101. ISSN: 0017-9310. DOI: https://doi.org/10.1016/0017-9310(95)00190-5. URL: https://www.sciencedirect.com/science/article/pii/0017931095001905.

[68] H. Tennekes and J.L. Lumley. *A First Course in Turbulence*. Butterworth, 1989, pp. 28–34, 43, 51–52. ISBN: 9780262200196.

[69] Thea Valsø Klynderud. "The influence of free-stream turbulence on heat transfer in finned tube bundles". MA thesis. NTNU, 2014. URL: http://hdl.handle.net/11250/235746.

[70] H.K. Versteeg and W. Malalasekera. *An Introduction to Computational Fluid Dynamics: The Finite Volume Method*. Pearson Education Limited, 2007, pp. 55, 57–59, 65–66, 76–82, 191–196, 275, 277–278. ISBN: 9780131274983.

[71] Sebastien Vintrou et al. "Quantitative infrared investigation of local heat transfer in a circular finned tube heat exchanger assembly". In: *International Journal of Heat and Fluid Flow* 44 (2013), pp. 197–207. ISSN: 0142-727X. DOI: https://doi.org/10.1016/j.ijheatfluidflow.2013.05.019. URL: https://www.sciencedirect.com/science/article/pii/S0142727X13001276.

[72] D J Ward and E H Young. "Heat Transfer and Pressure Drop of Air in Forced Convection Across Triangular Pitch Banks of Finned Tubes". In: *Chem. Eng. Progr.* Vol: 55, Symposium Ser. No. 29 (Jan. 1959). URL: https://www.osti.gov/biblio/4170140.

[73] C. Weierman. “Correlations - Ease the Selection of Finned Tubes”. In: *The Oil and Gas Journal* 74 (1976), pp. 94–100.

[74] C. Weierman. “Pressure Drop Data for Heavy-Duty Dinned Dubes”. In: *Chem. Eng. Prog.* 73 (Feb. 1977), pp. 69–73.

[75] C. Weierman, J. Taborek, and W.J. Marner. “Comparison of the Performance of Inline and Staggered Banks of Tubes with Segmented Fins”. In: *AIChE Symp. Ser.* 74 (1978), pp. 39–46.

[76] F.M. White. *Viscous Fluid Flow*. McGraw-Hill international edition. McGraw-Hill, 2006, p 409. ISBN: 9780071244930.

[77] Dr. Aidan Wimshurst. *The k-omega SST turbulence model*. Accessed: Feb. 2021. Mar. 2019. URL: https://www.youtube.com/watch?v=myv-ityFnS4.

[78] Dr. Aidan Wimshurst. *The Spalart-Allmaras Turbulence Model*. URL: https://www.youtube.com/watch?v=Xivc0EIGFQw. Accessed: Nov. 2020. Feb. 2020.

[79] Dr. Aidan Wimshurst. *The Transition SST (gamma - Re_theta) model*. Accessed: Feb. 2021. July 2019. URL: https://www.youtube.com/watch?v=5htknS9uVEk.

Appendices

Appendix A

Streamlines of turbulence models

The streamlines of all the turbulence models tested in section 3.3 are shown in Figure (A.1) on the next page.

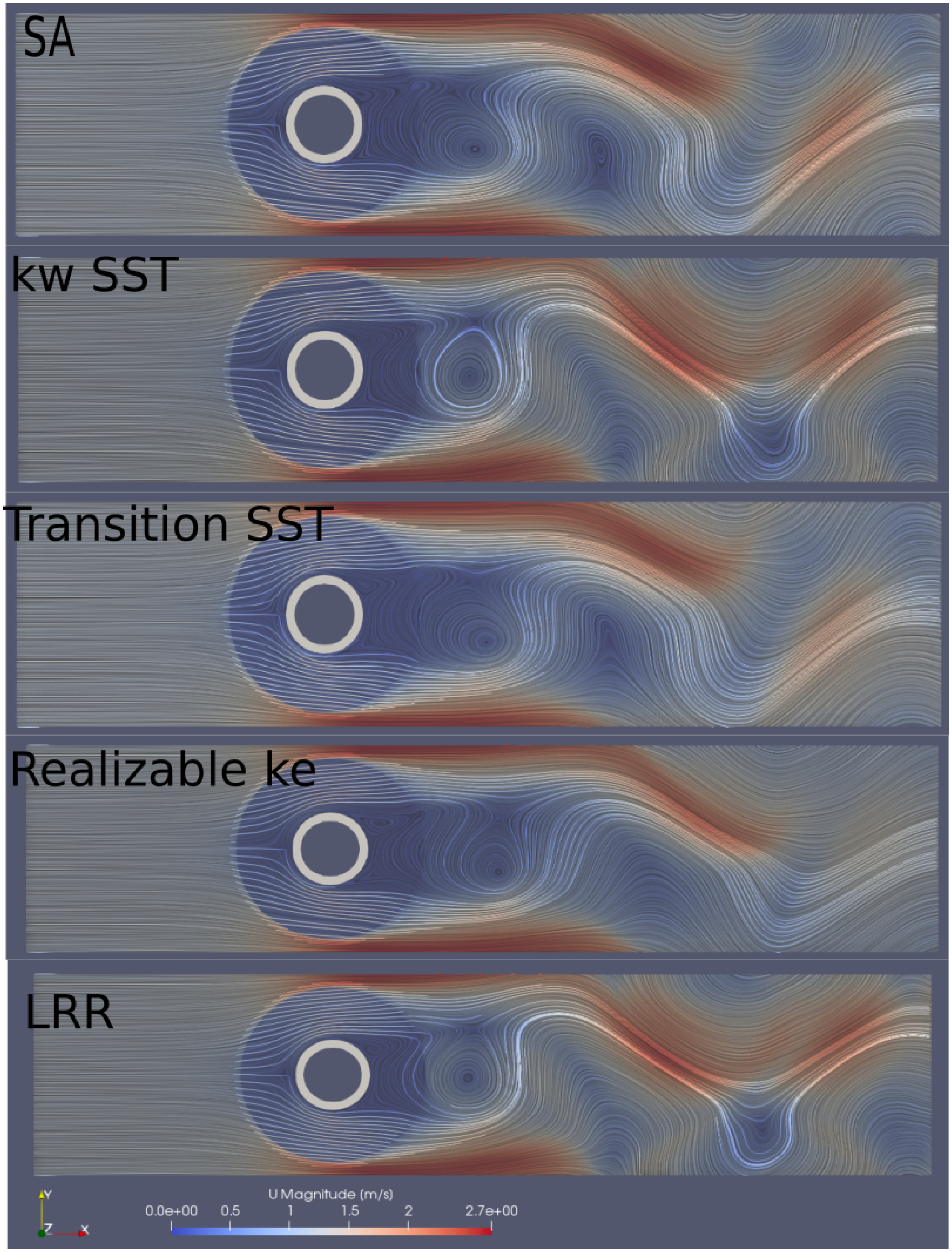

Figure A.1: Streamlines of turbulence models at $Re_{do} = 1000$

Appendix B

Nu distribution of turbulence models

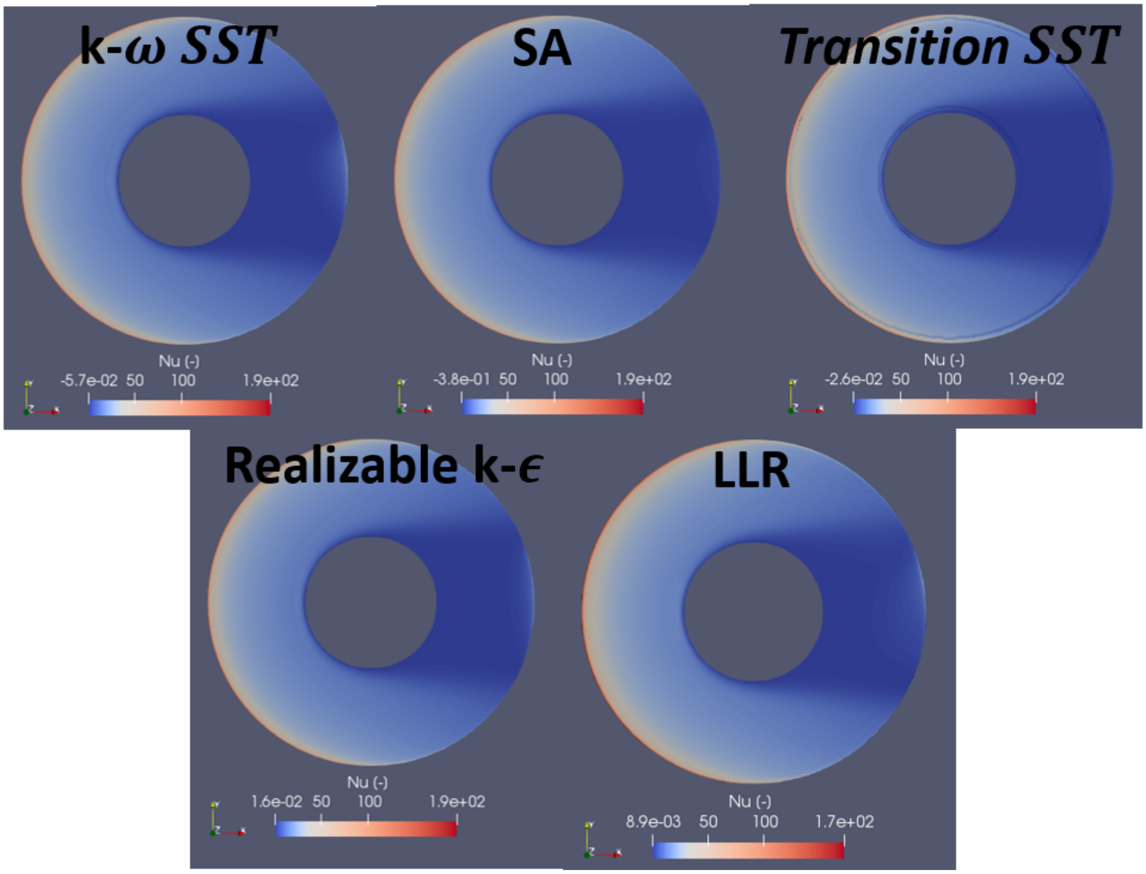

Figure B.1: The distribution of Nu over the fin for the simulations using the Spalart-Allmaras (SA), $k-\omega SST$ and Transition SST turbulence model at $Re_{d_o} = 1000$

Appendix C

Row-by-row development of Nu

Row-by-row development of Nu for different fin tip clearances

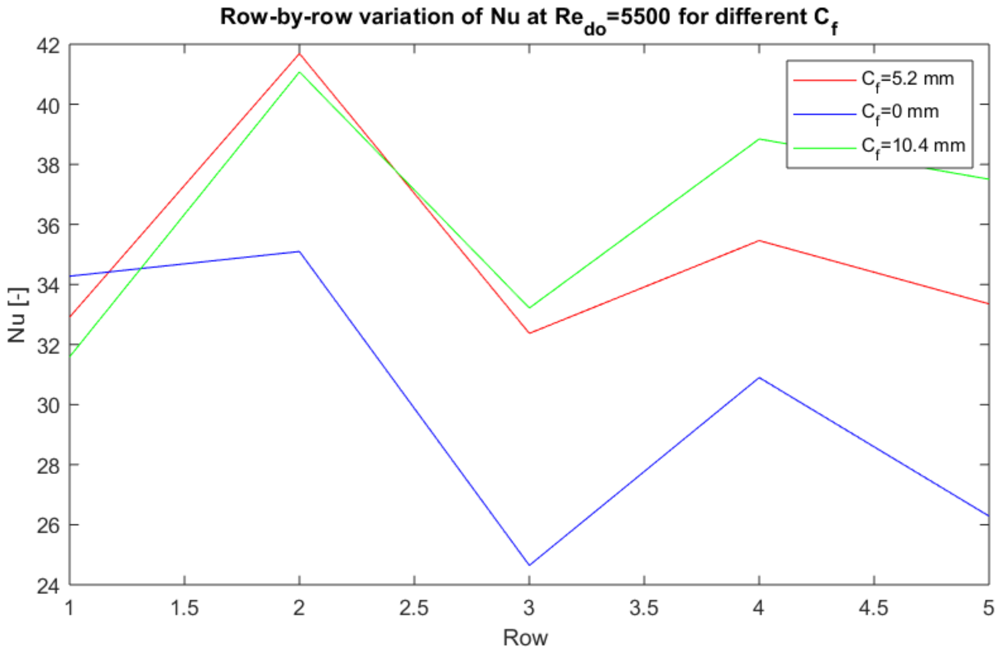

Figure C.1: Row-by-row Nu for different C_f

Row-by-row development of Nu for different fin pitches

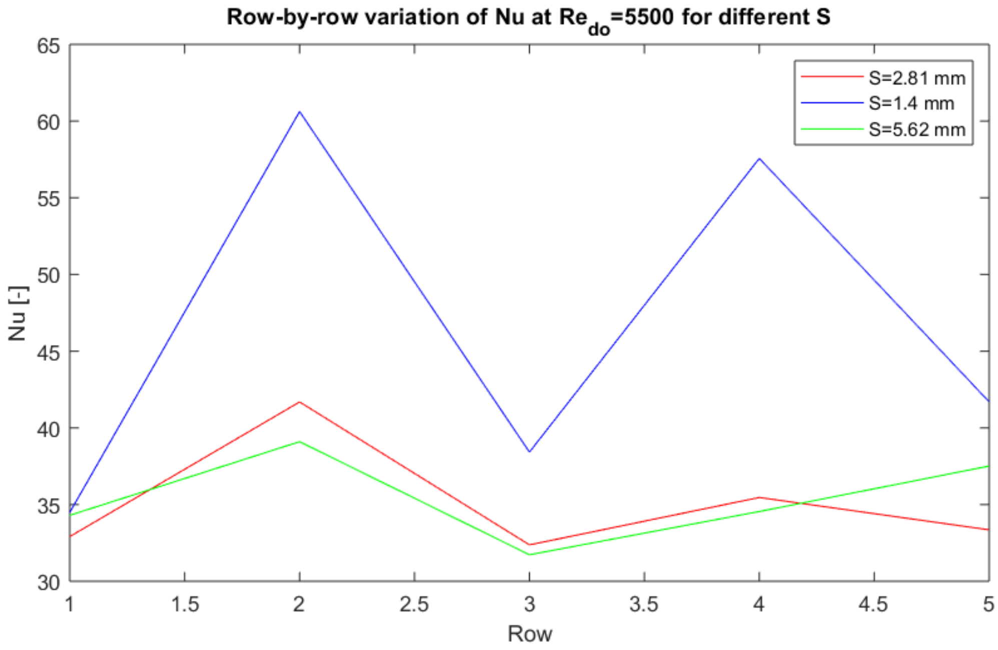

Figure C.2: Row-by-row Nu for different S

Row-by-row development of Nu for different layouts

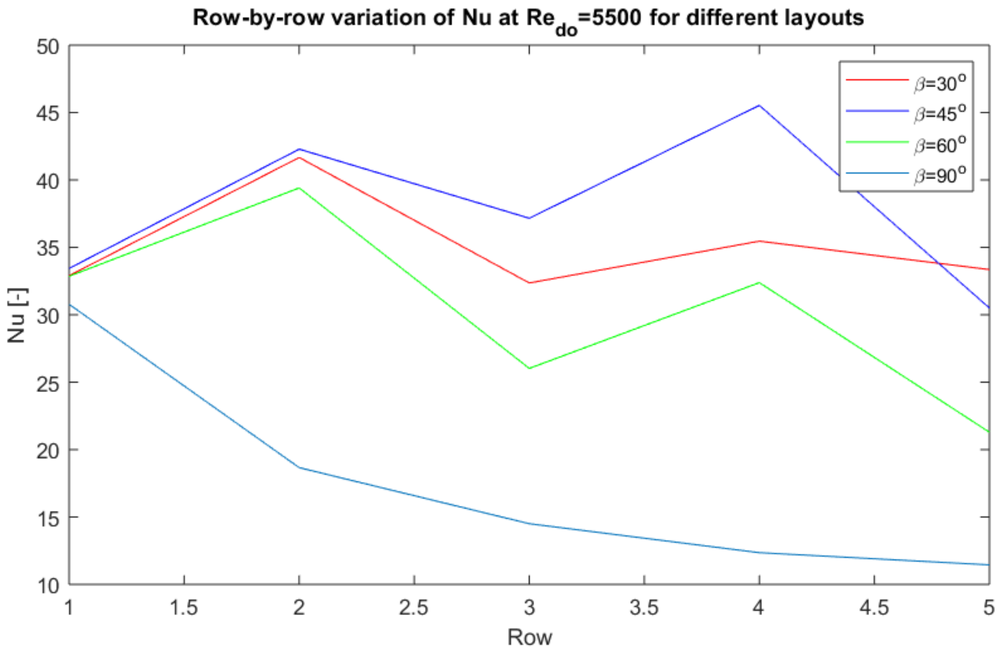

Figure C.3: Row-by-row Nu for different Layouts

Appendix D

Risk assessment

No full risk assessment was conducted in this master's thesis due to the task being theoretical. The first page of the assessment is shown on the next page.

NTNU		Prepared by	Number	Date
HSE	Hazardous activity identification process	HSE section	HMSRV2601E	09.01.2013
		Approved by		Replaces
		The Rector		01.12.2006

Unit: Department of Energy and Process Engineering (EPT) **Date:** **26.05.2021**

Line manager: ???

Participants in the identification process (including their function)**: Erling Næss (responsible supervisor), Andreas Herløsund Søgnen (student)**

Short description of the main activity/main process: Master project for student Andreas Herløsund Søgnen. Project title: Numerical analysis of finned-tubes and finned-tube bundles.

Is the project work purely theoretical? (YES/NO): YES *Answer "YES" implies that supervisor is assured that no activities requiring risk assessment are involved in the work. If YES, briefly describe the activities below. The risk assessment form need not be filled out.*

Signatures: *Responsible supervisor:* Erling Næss *Student:* Andreas Herløsund Søgnen

ID nr.	Activity/process	Responsible person	Existing documentation	Existing safety measures	Laws, regulations etc.	Comment
001	Numerical simulations in OpenFOAM of finned-tubes and finned-tube bundles for usage in offshore waste heat recovery units. The simulations are done on a computer provided by EPT and on the IDUN/EPIC comuter cluster at NTNU.					

Andreas Herløsund Søgnen

Numerical analysis of finned-tubes and finned-tube bundles

NTNU
Norwegian University of
Science and Technology